6-15-2023

SIMULATIONS OF INTRUDER-FREE X-RAY TRANSIENT ABSORPTION AND TIME-RESOLVED X-RAY SCATTERING FOR PROBING ATTOSECOND ELECTRON DYNAMICS

Mengqi Yang
Louisiana State University and Agricultural and Mechanical College

SIMULATIONS OF INTRUDER-FREE X-RAY TRANSIENT ABSORPTION AND TIME-RESOLVED X-RAY SCATTERING FOR PROBING ATTOSECOND ELECTRON DYNAMICS

A Dissertation

Submitted to the Graduate Faculty of the
Louisiana State University and
Agricultural and Mechanical College
in partial fulfillment of the
requirements for the degree of
Doctor of Philosophy

in

The Department of Chemistry

by
Mengqi Yang
B.S., Shanxi University, 2017
August 2023

I dedicate this dissertation to the Almighty God for giving me a glimpse of the ultrafast world of electrons.

Acknowledgments

I am deeply grateful to Prof. Kenneth Lopata, my supervisor, for his invaluable mentorship and support on the projects I have worked on during my PhD years in graduate school at Louisiana State University. He encouraged me to think independently and provided patient guidance through many unsure times. Without his inspiring insights and support, the completion of my research projects would have been impossible.

I am grateful to my advisory committee: Prof. Kenneth Schafer, Prof. Bin Chen, Prof. Daniel Kuroda, and Prof. Bhuvnesh Bharti for their time and insight into my research. I am also grateful for the expertise of the groups of Dr. Peter M. Weber and Dr. Adam Kirrander in our collaborative project on time-resolved X-ray scattering. I would like to thank Dr. Andrés Moreno Carrascosa for the help and critical discussions on incorporating RT-TDDFT into scattering framework. I am also in deep gratitude for Dr. Haiwang Yong for his invaluable expertise and patient help whenever I had scattering-related questions. Moreover, I would like to express my sincere appreciation to Department of Energy (DOE), for their financial support to my PhD researches.

I would also like to express my gratitude to Dr. Adonay Sissay for his willingness to help whenever I needed it. I would like to send my thank to Dr. Alex Meyer, who always cheered me up with pictures of his dog. I am thankful to all other members in my group for their kind help and useful suggestions.

Most importantly, I would like to thank to my family and friends. Their love, encouragement, and unwavering support have sustained me throughout the ups and downs of my PhD journey. Their understanding and patience have been a constant source of motivation, and I am forever grateful for their presence in my life.

Thank you all for being part of this journey and for making it an unforgettable one.

Table of Contents

Abstract

The motion of electrons plays a fundamental role in both physics and chemistry, and capturing such dynamics requires the ability to resolve changes at the attosecond timescale, which is enabled by the advent of ultrashort laser pulses. This dissertation aims to facilitate the interpretation of ultrafast electron dynamics and attosecond spectroscopy by real-time time-dependent density functional theory (RT-TDDFT) simulations. The first part of this dissertation focuses on improving the simulation of X-ray transient absorption spectra (XTAS) with Gaussian basis sets in RT-TDDFT by applying a filter to the transition dipole matrix. Due to the spatial limitation of atom-centered Gaussian functions, the transitions from higher-energy orbitals to the poorly described continuum can show as "intruder" peaks in the simulated core-level spectra. This can further result in unphysical modulations in the calculated XTAS, leading to incorrect interpretations of the corresponding electron dynamics. By manually zeroing all elements arising from unwanted transitions, the calculated XTAS are free of these unphysical peaks. This methodology can be adapted to other Gaussian-based real-time methods. In the second part of this dissertation, a combination of RT-TDDFT and scattering theory is employed to calculate time-resolved X-ray scattering and explore the potential mapping between the scattering signals and electron dynamics. The investigations of the electron motions induced by core-hole ionization or a UV pump in both ring-shape and linear molecules reveal measurable modulations between the electron currents and the scattering patterns.

Chapter 1. Introduction

1.1. Resolving Electron Dynamics with Ultra-fast X-ray Pulses

Electronic structure is a critical component that determines the physical and chemical properties of materials. Its rearrangement, which takes place on an attosecond (1 as= 10^{-18} s) timescale, drives the femtosecond-nuclei motions (1 fs = 10^{-15} s) and initiates chemical reactions and transformations of matter. Therefore, the investigation of the electronic landscape and its time evolution are of fundamental interest in chemistry, biology and physics, such as the photo-damage to DNA strands [1, 2], the clock time in processors [3], the solar energy conversion [4], etc. However, the ultrafast nature of electron motion presents challenges for both experimental and theoretical studies. The growing demand for measuring these dynamics has spurred the development of ultrafast optics and motivated its technical leaps with the advent of sub-femtosecond X-ray laser pulses produced by high harmonics generation (HHG) [5] and X-ray free electron laser (XFEL) [6–9]. Both of these laser sources result from the energy released by accelerated electrons, but they rely on different mechanisms. HHG generates ultrashort pulses by the recombination of the tunneling ionized and accelerated free electrons with few-cycle IR pulses, while the XFELs deploy the interaction between realistically accelerated free electrons near the speed of light and the emitted radiation, offering unprecedented peak intensity and angstrom-scale spatial resolution [10]. With these sub-femtosecond lasers, a plethora of methods have been developed to peek into the electron world. As the HHG process is driven by the time evolution of the electron wavepackets in the strong laser field, the electronic structural and dynamical information can be reconstructed by the analysis of the

emitted ultrashort pulses, which has grown into a mature technique called high harmonic spectroscopy (HHS) [11, 12]. The attosecond electron motions can also be captured by the attoclock technique, where the temporal information is encoded in the final momentum angle of a free electron liberated by an intense circularly polarized laser pulse, without the involvement of the ultrafast pulses [13–15]. Alternatively, the electron dynamics can be tracked by pump-probe setup, where the pump pulse ignites the electronic transitions, and the probe pulse takes snapshots of the system at different time delays. The nonstationary electron transitions can be recovered by a photo-ionization probe that renders the kinetic energy distribution of the photo-electron over time, such as attosecond streaking [16–18] and RABBIT (reconstruction of attosecond beating by interference of two-photon transitions) [19, 20] techniques. Transient absorption spectroscopy (TAS) is another powerful tool for studying time-resolved electron dynamics. By monitoring the changes in the absorptance at specific photon energies as a function of time, TAS can reveal the time evolution of the population of transient states via the modulations of optical density and energy shifts. With different choices of pump and probe pulses, different dynamical attributes can be portrayed [21]. The combination of isolated attosecond X-ray pump pulse, which currently can be as short as 53 as [22], and a few-cycle IR probe have been implemented to detect the dynamics of lass-dressed states and light-induced species [23–25] as well as electron relaxations [26, 27]. However, this approach typically requires a long-enough dephasing time so that the time-evolving electron superpositions can be probed by the femtosecond IR pulse, and thus its current application is constrained in atomic systems [28]. On the other hand, X-ray transient absorption spectroscopy (XTAS), a time-resolved version of X-ray absorption near edge absorption spectroscopy (XANES)

using attosecond X-ray as the probe, provides a more versatile option that can access the dynamics from atoms to solids. Given that XANES arises from the excitation of the low-lying inner-shell electrons by the high photon energy provided by X-ray pulses and the core electrons of different elements separate each other at distinguishable energies and are localized around their atomic core, the transitions from core-edges to unoccupied orbitals can manifest the element-specific electronic structure and its surrounding chemical environment [29–32]. With the development of isolated attosecond soft X-ray pulses [5], it has become possible to recover the electronic density around a particular absorbing atom via modulations in the XANES spectrum and exploited in revealing the evolution of valence electrons [33–36], band distortion and dynamics in solids [3, 37, 38], electron relaxation in chromophores [39, 40], and charge migration in silane gas [41]. With the realization of bright water-window laser pulses [42, 43], XTAS will be able to explore the dynamics in more complex molecules and clusters. Despite its advantages and increasing attention, XTAS has limited utility for systems consisting of the same element or heteroatoms with close core-edge energies, where the absorption positions of inner-shell electrons will be difficult to distinguish.

By virtue of its short wavelength, X-ray can also elucidate electronic and atomic structure of various samples via their scattering patterns. When an incident X-ray pulse hits the sample, it will be scattered by the electron density. Two scenarios can occur during the scattering process. If the photon reflects from the sample without changes in energy but only polarization, this event is defined as elastic scattering. While if the scattered photon shifts in wavelength, which triggers electron transitions in the sample, this circumstance is called inelastic scattering. Together with the elastic and inelastic scattering, the

electronic arrangement can be revealed by the complex scattering signals. Traditionally, this technique has been widely used to recover the repeating structure of crystals from the diffraction pattern [44, 45]. In recent years, profiting from the unprecedented peak brightness and angstrom spatial resolution of the XFELs, gas-phase time-resolved X-ray scattering has been achieved, illuminating time-dependent electronic structure during photoexcitation [46] and the evolution of nuclear wave packets in chemical reactions [47–51]. Currently, due to limited temporal resolution, direct imaging of the attosecond electron dynamics with time-resolved X-ray scattering is not accessible. However, with the development of attosecond hard X-rays [52, 53], X-ray scattering can be a promising and versatile tool to probe all-element electron dynamics. Together, with the XTAS detecting the localized electron density motion around the absorbing center and the time-resolved X-ray scattering filming the spatial electronic flow, these two approaches are able to be complementary tools for illustrating complex electron dynamics from different perspectives.

1.2. Simulations of Electron Dynamics and Their X-ray Signals

Although efforts to develop ultrashort pulses for uncovering the atto- to femtosecond dynamics have made significant progress, it remains a challenging task to perform direct measurements and interpret the rich and complex information from the generated spectra. Therefore, the simulations of the time-evolution of the electron density and the resulting spectra, are of importance, for shedding light into the dynamics, predicting the experimental spectroscopic features, and establishing a mapping between these two. To acquire the electron dynamics of a polyelectron system, one needs to first solve the Schrödinger equation to obtain its state functions, from which all measurable properties

are calculated. Due to the intricate interactions between each electron, the exact solution to Schrödinger equation is numerically untractable for systems with more than two electrons. To this end, approximations are necessary to access electronic wave functions in many-body systems, giving rise to various theories that facilitate the advance of quantum chemistry. In general, *ab initio* methods, which solve the Schrödinger equation without any empirical parameters, have two flavors: one is correlated methods that address electron correlations explicitly via many-electron wavefunctions, such as configuration interaction (CI) [54], multiconfigurational self-consistent-field (MCSCF) [55], and coupled cluster (CC) [56] etc; and the other is mean-field based approaches which assume the electrons move in a fictitious field averaged from the Coulomb interaction of the electrons, including Hartree-Fock (HF) method [57–59] and density functional theory (DFT) [60, 61]. While the consideration of excited state wavefunctions makes correlated methods more favorable in accuracy, they require heavy computational burdens for large systems. On the other hand, as a result of the utilization of a single Slater determinant, the mean-field methods provides more computationally economic solutions. Compared with HF, DFT can provide a better description of electronic states by incorporating electron correlation, albeit in a mean field way.

Regarding adopting DFT in time-dependent domains, there are linear response and real-time approaches. By applying the appropriate approximations in linear response theory, one can obtain observable changes towards small perturbations and determine the excitation energies from atoms to clusters [62–65]. Despite of the efficiency for precluding the full solution to the time-dependent Schrödinger equation and directly connecting to single-photon absorption, linear-response-based approaches are valid only when the ex-

ternal field is weak enough that the electron density is not driven far from the ground state, which prevents them from fully describing the interaction between external fields and electrons. On the other hand, by explicitly propagating electron wavepacket or density in real-time and real-space, real-time methods track the electron response towards external fields with any arbitrary profile. Although real-time methods are more time consuming since they require simulations to be long enough to capture all desired transition modes, they are more natural to portray the electron dynamics in response to time-dependent external fields, especially in non-linear regimes such as strong laser fields and pump-probe experiments, by taking the pulses at the same footing. When solving the time-dependent Schrödinger equation, despite that the advances in computation resources make the wavefunction-based approaches feasible to be incorporated into real-time framework [66–69], real-time time-dependent density functional thoery (RT-TDDFT) [70–72] stands out as a workhorse in computational chemistry community for the balance between computational efficiency and accuracy provided by DFT. RT-TDDFT has been utilized to reveal the coherent electron motions in charge migration [73–77], electron tunneling dynamics in strong field [78–80], conducting behaviors of electron [81, 82], UV-vis [71, 83–87] and core-level [71, 88–91] spectroscopy, as well as pump-probe spectra [92–94].

With the time-dependent electronic properties obtained from *ab initio* simulations, one can calculate the resulting signals with respect to different probing techniques. As a maturing technique with impressive achievements in measuring electron motions, XTAS has garnered a great deal of attention for simulations, which can be generally assigned to two types. The earliest attempt to model the XTAS for the intriguing dynamics treats the probe as an ultrashort pulse perturbatively, which is only applicable for non-overlapping

pump-probe setups and has been employed to identify the spectral features with respect to the hole dynamics in the transient absorption experiment of Kr [35] analytically [21], capture the charge migration in the chromophore group [95] with a one-electron reduced density operator [96], and track hole dynamics by including the degree of freedom of nuclei within the algebraic diagrammatic construction (ADC) framework [97]. Although these approaches can accurately reproduce the XTAS for targeted transitions, they are not versatile in terms of systems and pump-probe profiles. On the other hand, extensive work has been devoted to addressing the pump and probe at the same level so that it can cover both overlapping and nonoverlapping pump-probe setups. Chew *et al.*[98], by solving TDSE with spectral basis sets, demonstrated how the dressing IR pulse modified the electronic structure and dynamics of Ar. Through a combination of TDDFT and Maxwell equation, band dynamics and the corresponding XTAS in crystalline solids have been thoroughly investigated [37, 99]. Pabst *et al.*[33] employed time-dependent configuration interaction singles (TDCIS) to investigate the dynamical information revealed by the absorption line features in the previous transient absorption experiment of Kr [36]. RT-TDDFT has been deployed in calculating XTAS [92, 94], decoding the modulations between the spectra and valence electron motions. To manifest the relationship between the charge migration and transition dipole phase, Kobayashi *et al.*[100] calculated the electron dynamics and XTAS using a multi-state methodology. While RT-TDDFT has accurately attributed the spectral changes to the correct dynamical features with low computational costs, when the field induces significant excitation or density change, unphysical electron dynamics can arise due to the localization of the exchange functional in time, as discussed in Provorse et al[101]. To overcome this issue, constrained DFT (cdft) [102] can be em-

ployed to mimic the electronic structure immediately after the pump via constructing a well-defined excited initial state [73, 92]. Also, additional care and attention are required when utilizing Gaussian basis sets in real-time methods to simulate core-level spectra, especially the time-resolved ones. This is because the atom-centered Gaussian functions usually describe the asymptotic density poorly and can lead to unphysical transitions from occupied to continuum states, resulting in polluted spectra. A methodology to address this issue will be discussed in Chapter 3.

Regarding the study of time-resolved X-ray scattering, many endeavors have been undertaken to understand and predict the time-dependent scattering pattern. Even before the realization of ultrafast laser pulses, time-resolved X-ray scattering has been envisioned to track electric and nuclear motions and explored theoretically [103–105] with the independent atom model (IAM), which addresses each atom as an isolated scatter. Despite its convenience in calculating the scattering patterns for complex molecules[51, 106–108], IAM can not capture the electron density redistribution and is insufficient for tracking coherent electron motions in the simulated time-resolved scattering signal. To further investigate how the ultrafast dynamics in molecules can be encoded in the scattering signals, many *ab initio* approaches have been developed to model the gas-phase time-resolved X-ray scattering. By fully accounting for the quantum nature of the involving laser pulses, it has been demonstrated that unlike the elastic scattering, the inelastic scattering contribution of non-equilibrium electronic states cannot be accounted for by the Fourier transform of electron density but is related to electronic coherence [109, 110], which is further justified in later theoretic studies [109, 111, 112]. Herman et al. have shown that the time-resolved scattering signal is mainly effected by the time-derivative of the instantaneous density,

which is linked to the electron current via continuity equation [113] and suggests that X-ray scattering is a viable probe for measuring electronic processes and can probe more dynamical details than XTAS. Taking this as an ansatz, we simulated the time-resolved scattering patterns for valence motions with the combination of RT-TDDFT and scattering theory and explored how the electronic flows can be reflected in the scattering patterns.

1.3. Scope of Dissertation

The primary objective of this dissertation is to resolve electron dynamics at attosecond timescale in real-space using first-principle simulations, improve the accuracy of the calculation of X-ray transient absorption spectra (XTAS) as well as predict the time-resolved X-ray scattering of corresponding electron motions. Throughout this dissertation, RT-TDDFT is used to calculate various time-dependent quantities. Chapter 2 provides a general guide to the many-body system and its solutions in Hartree-Fock (HF) theory, density functional theory (DFT), and its time-evolving version, real-time time-dependent functional theory (RT-TDDFT).

In Chapter 3, an overview of XTAS is provided and the unphysical peaks that can occur in the simulated XTAS using Gaussian basis sets are discussed. Since atom-centered Gaussian functions provide a poor description of continuum states, which is a significant drawback when calculating core-edge absorption spectra, transitions from higher energy orbitals to the poorly portrayed continuum may sneak into the calculated spectra, leading to wrong predictions and interpretations of the dynamics. To overcome this issue, a "dipole filter" methodology is proposed and discussed. The dipole filter selectively removes transitions between unwanted orbitals, thus retaining only the transitions from the desired

core edges. The dipole filter methodology can also be employed to compute "pollution-free" XANES, particularly for systems with a high density of states (DOS) where LR-TDDFT is not feasible. Additionally, since the Gaussian basis sets are widely utilized in the quantum chemistry community, this method can be applied to other real-time-based methods. Further details of the dipole filter methodology and its validation in various systems will be presented in this chapter.

Chapter 4 explores the potential link between time-resolved scattering patterns and real-time electron dynamics. Recent studies suggest that the time-resolved scattering signal is related to the time-derivative of the electron density rather than the density itself [113, 114]. To investigate this relationship, scattering signals are simulated using a combination of RT-TDDFT and scattering theory, with the ansatz that the time-resolved scattering signal can be approximated by the time-derivative of the electron density. The methodology of the simulations and discussion of the mapping between the currents and scattering patterns are elaborated in this chapter.

Chapter 2. Methods

2.1. Hamiltonian for Many Electrons

The state of an atomic/ molecular system hinges on the distribution of electrons and nuclei. As electrons are much lighter than nuclei, they travel at much faster speed than the latter. Therefore, when examining the electronic structure, nuclei are often considered "fixed" and disentangled from the degree of freedom of electrons, which is well-known as Born–Oppenheimer approximation. This simplification reduces the nucleus kinetic energy and nuclei-nuclei interaction to constant values within a certain atomic configuration. Thus, in atomic units, the N-electron Hamiltonian can be expressed as follow [115, 116],

$$\hat{H} = -\sum_{i=1}^{N} \frac{1}{2}\nabla_i^2 - \sum_{i=1}^{N}\sum_{A=1}^{M} \frac{Z_A}{r_{iA}} + \sum_{i=1}^{N}\sum_{j>i}^{N} \frac{1}{r_{ij}}, \tag{2.1}$$

where M represents the number of nuclei and Z_A corresponds to the charge for nucleus A. The three terms on the right of this equation in order account for electron kinetic energy, electron-nucleus attraction and electron-electron interaction. Since the first two terms are sum of single electron states, they can be calculated analytically with relative ease. However, the third term requires considering all possible couplings between each electron, making the exact solution impossible with finite computation resources and has to be approximated.

2.2. The Hartree-Fock Method

Hartree-Fock (HF) approximation is one the most successful *ab initio* approaches for solving the many-body Schrödinger equation in the early stage of quantum chemistry [57, 59, 117]. Many modern theories including density-functional theory (DFT) are de-

veloped on the foundation it builds. To simplify the complex many-electron model, HF assumes that each electron moves within the mean-field imposed by other electrons and reduces the many-electron wavefunction into a single Slater determinant. The Fock operator is used to denote the Hamiltonian of the system and for the orbital $\psi_i(\mathbf{r})$ it is constructed as,

$$\hat{f}_i = -\frac{1}{2}\nabla_i^2 - \sum_{A=1}^{M}\frac{Z_A}{r_{iA}} + \sum_{j=1}^{\frac{N}{2}}\left[2\hat{J}_j(i) - \hat{K}_j(i)\right]. \tag{2.2}$$

Here because the kinetic energy and electron-nuclear attraction terms are one-electron operators, they together can be represented as a single electron notation $\hat{h}_{core}$,

$$\hat{h}_{core} = -\frac{1}{2}\nabla_i^2 - \sum_{A=1}^{M}\frac{Z_A}{r_{iA}}. \tag{2.3}$$

The mean-field in HF theory is constructed as the sum of the two-electron operators: the Hartree term $\hat{J}_j(i)$ and the exchange term $\hat{K}_j(i)$. While the Hartree term approximates the Coulomb repulsion between electrons, it does not prevent the possibility that the i^{th} and j^{th} electron overlap in space, which makes the electron correlation incomplete and can only render exact solution for one electron system. The exchange operator, arising from the antisymmetry of the Slater determinant, does not have a classic picture but is fully addressed in HF. With the ground state HF equation,

$$\hat{f}_i\psi_i = \epsilon_i\psi_i, \tag{2.4}$$

the ground state wave function $\psi_i(\mathbf{r})$ and energy ϵ_i for the i^{th} molecular orbital (MO) can be obtained as the the eigenfunction and eigenvalue, respectively. However, the numerical solution to this integro-differential equation is impractical. To address this issue, Roothaan constructed the MOs as the linear combination of a set of known functions,

which are called atomic orbitals (AOs) $\{\phi_\mu\}$,

$$\psi_i = \sum_\mu C_{\mu i}\phi_\mu \tag{2.5}$$

with the $C_{\mu i}$ as the coefficient of the μ^{th} atomic orbiatl ϕ_μ. The atomic basis set should be expressed as Slater orbitals in principle. However, for the consideration of computational efficiency, Gaussian functions are widely-used in computational chemistry community as basis sets. Despite their low computational cost, Gaussian basis sets generally cannot accurately describe continuum states. This can lead to unphysical ionization when using complex absorption potentials (CAPs) [79, 118], incorrect core absorption spectra and other related issues. Chapter 3 will address the problematic core-edge spectra in detail. By multiplying both sides of the HF equation (2.4) with ψ_i^* and integrating over the spatial coordinates, the matrix representation can be written as,

$$\mathbf{FC} = \mathbf{SC}\epsilon. \tag{2.6}$$

The element of the Fock matrix is evaluated by,

$$\begin{aligned}\mathbf{F}_{\mu\nu} &= \langle\phi_\mu|\hat{f}_i|\phi_\nu\rangle \\ &= H_{\mu\nu}^{core} + \sum_{\lambda\sigma} P_{\lambda\sigma}[(\mu\nu|\sigma\lambda) - \frac{1}{2}(\mu\lambda|\sigma\nu)].\end{aligned} \tag{2.7}$$

where density matrix $\mathbf{P}$ can be calculated from the coefficients,

$$P_{\mu\nu} = 2\sum_{a=1}^{N/2} C_{\lambda a}C_{\sigma a}^*. \tag{2.8}$$

The $(\mu\nu|\sigma\lambda)$ is the notation for two-electron integral, which is evaluated as,

$$(\mu\nu|\sigma\lambda) = \int \phi_\mu^*(1)\phi_\nu(1)\frac{1}{r_{12}}\phi_\sigma^*(2)\phi_\lambda(2)d\mathbf{r}_1 d\mathbf{r}_2, \tag{2.9}$$

and $\mathbf{S}$ is defined as the overlap matrix with elements:

$$\mathbf{S}_{\mu\nu} = \langle \phi_\mu | \phi_\nu \rangle. \tag{2.10}$$

Since the atomic orbitals are pre-known, the electronic wave functions and energies can be calculated with the coefficient matrix $\mathbf{C}$ and eigenvector ϵ. However, as the atomic orbitals are not necessarily orthogonal, this equation is challenging to solve with non-unitary overlap matrix. Therefore, the canonical orbitals (COs) $\{\phi'_i\}$ are introduced by orthogonalizing the AO basis,

$$\phi'_i = X_{\mu i}\phi_\mu, \tag{2.11}$$

with the transformation matrix $\mathbf{X}$ given by,

$$\mathbf{X} = \mathbf{U}\mathbf{s}^{-\frac{1}{2}}. \tag{2.12}$$

Here $\mathbf{U}$ is the eigenvector of the overlap matrix $\mathbf{S}$ and $\mathbf{s}$ is the corresponding eigenvalue matrix. By constructing the MOs with COs with,

$$\psi_i = \sum_\mu C'_{\mu i}\phi'_\mu \tag{2.13}$$

the Roothaan equation can be represented as,

$$\mathbf{F}'\mathbf{C}' = \mathbf{C}'\epsilon, \tag{2.14}$$

which can smoothly yield the CO coefficient matrix $\mathbf{C}'$ and the ground state energies through diagonalization procedure. Here $\mathbf{F}'$ denotes the Fock matrix in COs and can be projected from AOs with,

$$\mathbf{F}' = \mathbf{X}^\dagger \mathbf{F} \mathbf{X}. \tag{2.15}$$

As shown in equation (2.7), the Fock matrix is a function of the density matrix, which is determined via the coefficients obtained from equation (2.14). Therefore, the HF equation must be solved iteratively. Firstly, an initial guess of the coefficient matrix is provided based on the given AOs. The Fock matrix, $\mathbf{F}'$, is then calculated using this initial guess. Secondly, a new coefficient matrix is obtained by diagonalizing $\mathbf{F}'$ from the previous step. The calculated $\mathbf{C}'$ is then used as a new input to the first step. These operations are repeated until the coefficient matrix $\mathbf{C}'$ is converged. This procedure is also well-known as the self-consistent field (SCF) method, which has facilitated the implementation of various electronic structure theories. For more details about the HF method, the readers are referred to Ref [117].

2.3. Kohn-Sham Density Functional Theory

Density functional theory is underpinned by the Hohenberg-Kohn (HK) [60] theorem, which establishes that there is a one-to-one correspondence between the ground-state energy of a many-electron system and its electron density $\rho(\mathbf{r})$. This means that, in principle, any electronic property of the system can be obtained from the ground-state density. In practice, however, calculating the exact ground-state density for a many-electron system is computationally intractable. To facilitate the practical implementation of DFT, Kohn and Sham (KS) [61, 119] introduced the effective potential which arises from non-interacting electrons that have the exact ground-state density as the interacting system [120–122]. In this way, the Hamiltonian can be represented by a one-body KS Hamiltonian,

$$\hat{h}_{KS} = -\frac{1}{2}\nabla^2 + \hat{V}_{\text{eff}}(\mathbf{r}). \tag{2.16}$$

The Kohn-Sham (KS) effective potential is composed of three distinct contributions, namely the external potential $\hat{V}(\mathbf{r})$, the Hartree potential $\hat{J}(\mathbf{r})$, and the exchange-correlation potential $\hat{V}_{xc}(\mathbf{r})$.

$$\hat{V}_{\text{eff}}(\mathbf{r}) = \hat{V}_{\text{ext}}(\mathbf{r}) + \hat{J}[\rho](\mathbf{r}) + \hat{V}_{\text{xc}}[\rho](\mathbf{r}). \tag{2.17}$$

Here $\rho(\mathbf{r})$ is the electron density of the auxiliary non-interacting system,

$$\rho(\mathbf{r}) = \sum_{i=1}^{N} |\psi_i(\mathbf{r})|^2, \tag{2.18}$$

and the i^{th} KS orbital ψ_i is the eigenfunction of the KS equation with orbital energy ϵ_i that satisfies,

$$\hat{h}_{\text{KS}}\psi_i = \epsilon_i\psi_i. \tag{2.19}$$

In the effective potential, the external potential accounts for the Coulomb interaction between electrons and the nuclei,

$$\hat{V}_{\text{ext}} = \sum_{A=1}^{M} \frac{Z_A}{|\mathbf{r} - R_A|}. \tag{2.20}$$

The Hartree potential arises from the electrostatic repulsion between electrons and is given by the Coulomb operator $\hat{J}(\mathbf{r})$, which is a functional of the electron density $\rho(\mathbf{r})$,

$$\hat{J}[\rho](\mathbf{r}) = \int \frac{\rho(\mathbf{r}')}{|\mathbf{r} - \mathbf{r}'|} d\mathbf{r}'. \tag{2.21}$$

Finally, the exchange-correlation potential $\hat{V}_{xc}(\mathbf{r})$ accounts for the effects of electron correlation and exchange, which cannot be fully expressed in terms of the electron density alone,

$$\hat{V}_{\text{xc}}[\rho](\mathbf{r}) = \int v_{\text{xc}}\rho(\mathbf{r}) d\mathbf{r}, \tag{2.22}$$

with the exchange correlation potential represented in terms of exchange correlation energy E_{xc},

$$v_{\mathrm{xc}} = \frac{\delta E_{\mathrm{xc}}}{\delta \rho}. \tag{2.23}$$

In theory, the electronic distribution obtained from DFT is exact with the exchange-correlation term correcting all the effects from the quantum nature of the electrons, including the electron correlation and exchange effects. However, the exchange correlation is a non-classical term that is not readily available from first principles, and its calculation remains one of the most challenging tasks in DFT. To address this challenge, various approximations have been developed: from local density approximation (LDA) [119], generalized gradient approximation (GGA)[123, 124], to hybrid functionals [125, 126], with increasing complexity and accuracy. When the correlation energy is neglected, using the exact exchange contribution, the KS Hamiltonian is reduced to HF representation. Due to the dependence of the KS Hamiltonian on the electron density, which in turn is determined by the KS orbitals, a self-consistent field (SCF) approach needs to be employed to solve the KS equation. In this iterative procedure, an initial guess of the KS orbitals is used to compute the electron density and the corresponding KS potential, which is then used to obtain a new set of KS orbitals. The procedure continues until convergence is achieved, ensuring that the electron density and the KS orbitals are mutually consistent.

2.4. Real-Time Time-Dependent Functional Theory

To gain insight into the electronic response to an external field, DFT has been applied to solve the time-dependent Schrödinger equation [70–72], which formulates the real-

time time-dependent functional theory (RT-TDDFT),

$$i\frac{\partial}{\partial t}\psi_i(\mathbf{r},t) = [-\frac{1}{2}\nabla^2 + \hat{V}_{\text{ne}}(\mathbf{r}) + \hat{V}_{\text{ext}}(\mathbf{r},t) + \hat{J}[\rho(t)](\mathbf{r}) + \hat{V}_{\text{xc}}[\rho(t)](\mathbf{r})]\psi_i(\mathbf{r},t). \tag{2.24}$$

Here $\hat{V}_{\text{ne}}$ stands for the nucleus-electron interaction and $\hat{V}_{\text{ext}}$ represents the interaction between the electrons and the external field. When subject to electromagnetic field which is homogeneous across the investigated system, the $\hat{V}_{\text{ext}}$ takes the form,

$$\hat{V}_{\text{ext}}(\mathbf{r},t) = -\hat{d}(\mathbf{r})E(t) \tag{2.25}$$

with $\hat{d}$ as the dipole operator and $E(t)$ as the amplitude of the field.

In the modeling of the time-evolving electronic system, the exchange correlation $\hat{V}_{\text{xc}}$ is formally determined by the entire history of the electron density, the KS orbital Ψ_0 and the initial wave function of the non-interacting system Φ_0 at t=0 [116]. However, since the formal influence of these variables to the general-purpose time-dependent $\hat{V}_{\text{xc}}$ is out of our current knowledge, adiabatic approximation is often employed in TDDFT. This approximation assumes that the exchange-correlation potential is only a functional of the instantaneous density $\rho(t)$ at time t and does not explicitly depend on the previous history of the system [71, 127],

$$\hat{V}_{\text{xc}}[\rho(t_0,..,t);\Psi_0,\Phi_0](\mathbf{r}) = \hat{V}_{\text{xc}}[\rho(t)](\mathbf{r}). \tag{2.26}$$

This ignorance of electron density history poses challenges in describing the electron dynamics as the system evolves away from the ground state and undergoes significant changes in density, which is particularly problematic in the simulation of resonance processes, such as resonant pulse excitation [101, 128, 129] and Rabi cycling [130]. This adiabatic effect can be mitigated by propagating from an excited states, which can be obtained by linear-response TDDFT calculations[131], manual orbital occupation assignment

without energy optimization [132], or energy optimization with redistributed charge using constrained density functional theory (cDFT)[73, 92, 133].

In matrix representation, the time-dependent KS equation can be generalized as the Von Neumann equation,

$$i\frac{\partial \mathbf{P}'}{\partial t} = [\mathbf{H}'(t), \mathbf{P}'(t)], \tag{2.27}$$

where $\mathbf{H}'(t)$ and $\mathbf{P}'(t)$ are the time-dependent KS Hamiltonian and density matrix in orthogonal basis set. Note that this relationship will break with non-Hermitian Hamiltonian such as the inclusion of complex absorbing potential (CAP)[79, 84, 90], which instead should be expressed as,

$$i\frac{\partial \mathbf{P}'}{\partial t} = \mathbf{H}'(t)\mathbf{P}'(\mathbf{t}) - \mathbf{P}'(t)\mathbf{H}'(t)^{\dagger}. \tag{2.28}$$

With the converged ground states, the time-dependent density matrix can be calculated with the second order Magnus propagator which provides satisfying stability with large time steps [134],

$$\mathbf{P}'(t + \Delta t) = \exp^{\Omega} \mathbf{P}'(t) \exp^{-\Omega}, \tag{2.29}$$

with

$$\Omega = -i\mathbf{H}'(t + \frac{\Delta t}{2})\Delta t. \tag{2.30}$$

In the propagation of the density matrix over time, the future Hamiltonian $\mathbf{H}'(t + \frac{\Delta t}{2})$ is unknown and can be extrapolated from the Hamiltonian at times $t - \frac{\Delta t}{2}$ and t, with the density obtained through a SCF scheme. Firstly, the density matrix $\mathbf{P}'(t + \Delta t)$ for the next time step is calculated using equation 2.29, and the Hamiltonian $\mathbf{H}'(t + \Delta t)$ is built from the this new density. Secondly, the Hamiltonian $\mathbf{H}'(t + \frac{\Delta t}{2})$ is reconstructed from the interpolation of the one at time t and $t + \Delta t$. These two steps are repeated iteratively until

the density matrix converges.

Chapter 3. Intruder Peak-Free Transient Inner-Shell Spectra using Real-Time Simulations

3.1. Introduction

Electron dynamics are of fundamental interest for understanding complex phenomena like photosynthesis [135], light-harvesting [4], charge migration [73, 74], and conductivity in solids [136, 137], to name only a few. However, due to its attosecond timescale [9], electronic motion has only recently been directly measurable. The most versatile methods that have been deployed so far are photo-electron based techniques, such as high harmonic spectroscopy (HHS) [11], attosecond streaking [16, 17], RABBIT (reconstruction of attosecond beating by interference of two-photon transitions) [19, 20] and time-resolved photo-electron spectroscopy [138]. Alternatively, electron dynamics can be probed with attosecond X-ray laser pulses, generated either through high harmonic generation process [5] or at X-ray free electron laser (XFEL) facilities [6–9]. Attosecond transient absorption (ATAS) has been simulated for the study of ionization dynamics in polyatomic molecules [97, 139], and measured experimentally for ion population dynamics [35], evolution of autoionization states [27], electronic interference [140], and hole motion in solid states [18, 38, 141]. In an ATAS setup, a pump pulse is used to initiate the dynamics and an attosecond probe pulse takes snapshots at different pump-probe time delays. Owing to the spatial localization of the core electrons, the X-ray absorption near edge structure (XANES) encodes element-specific electronic structure information[142, 143]. By using isolated attosecond soft X-ray pulses [5], electronic density around a particular absorbing atom can

Reprinted with permission from Yang, M., Sissay, A., Chen, M. and Lopata, K., 2022. Intruder Peak-Free Transient Inner-Shell Spectra Using Real-Time Simulations. Journal of Chemical Theory and Computation, 18(2), pp.992-1002.

be probed via modulations in the XANES spectrum. These modulations are complicated, and reversing from time-delay to actual time typically requires first-principles simulations of both the dynamics and the observed spectra [92, 94].

There are numerous first-principles methods for simulating X-ray near edge spectra for the linear response (unpumped) case. Correlated methods for XANES include: algebraic diagrammatic construction (ADC) [144–146], equation-of-motion coupled-cluster (EOM-CC)[147–150], and Bethe-Salpeter equation with GW approximation[151, 152] etc. While these treat many-body effects accurately, their computational cost can grow rapidly for complex systems. Density functional theory (DFT), which can offer a good balance between cost and accuracy, can also be applied to XANES spectra using DFT with transition potential theory [153], orbital optimized DFT [154], orthogonality constrained DFT [155], and core-hole pseudopotentials [156, 157], to name a few. Time-dependent DFT, which has two general formulations, can also be used. Linear response TDDFT (LR-TDDFT) solves for the eigenvectors/values of a response function to obtain the excitation energies and oscillator strengths, and is a well-established method for computing single photon cross sections [158] and higher-order properties [159–165]. By windowing in energy or orbital space, LR-TDDFT can be used to compute XANES spectra [62, 65, 166–170]. For XANES, traditional functionals (i.e. local density approximation and generalized gradient approximation) are typically insufficient due to the large self-interaction energy errors. Hybrid functionals are generally more accurate for core-hole interactions due to admixture of exact Hartree-Fock exchange [62, 171–174]. Range-separated hybrids can also give an improved description when highly diffuse states are involved[90, 173].

Real-time TDDFT (RT-TDDFT), which propagates the electronic dynamics in

time domain, computes a spectrum from the Fourier transform of time-dependent dipole moment and has been widely applied to the simulation of XANES spectra [62, 84, 90, 91, 175–179]. In contrast to linear response spectra, attosecond X-ray transient absorption spectroscopy (XTAS) experiments often utilize strong pumps that create complex electronic superpositions involving either multi-orbital effects and/or non-reversible dynamics such as electron/nuclear coupling. In this case, real-time TDDFT is a natural choice since it can compute spectra for arbitrary dynamics and pump/probe configurations, for which perturbation-based methods are generally insufficient [21, 33, 92, 94, 180], although resonant pumping can be challenging for TDDFT with adiabatic functionals [101, 129].

Regarding basis sets, plane waves or grids have been applied for core-level spectroscopy [181, 182], however, they typically require core-hole pseudopotentials or similar techniques[183, 184]. Gaussian basis sets, on the other hand, are efficient for molecules, natural for describing core electrons and core-holes, and make all-electron calculations with hybrids tractable. Despite being widely exploited in the computational chemistry community, Gaussian basis sets give a poor description of high energy virtual states due to their limited spatial extent. This has been long understood for valence spectroscopy, where a large number of diffuse Gaussians are required for Rydberg states[185, 186]. Similarly, spectral features far above an X-ray ionization edge are problematic for Gaussians [84]. These failures are a result of the finite basis which makes the continuum states discrete. This in turn gives bound→continuum transitions artificially large amplitudes. In core spectra, this effect is especially deleterious as the transition from a higher edge to unphysical virtual states can occur at an excitation energy close to a near-edge transition from a deeper edge. In this unlucky case, an X-ray absorption will contain unphysical peaks or in-

creased absorption amplitude[85, 88, 90]. For a simple absorption spectrum, these spurious peaks can often be identified and removed by inspection. Linear response methods with an energy or orbital window do not suffer from this problem since they selectively compute transitions from a sub-set of core orbitals [65, 166, 168–170]. In real-time simulations of attosecond X-ray transient absorption, however, intruders can have a catastrophic effect on computed spectra, since they can exhibit nonphysical time-dependent modulations in their energies and oscillator strengths. These intruders are not generally observed in valence spectra, since they occur at energies much higher than the regions of interest.

Intruder peaks in RT-TDDFT were first addressed by Repisky and coworkers[88] who solved it using a selective perturbation method. In this method, they selectively include excitations from target core orbitals by zeroing all matrix elements of the dipole perturbation operator that do not involve particular core orbitals. This method modifies the electron-field interaction to only include contributions from particular core orbitals, and is not generally valid for pump-probe configurations, except possibly for the case of resonant X-ray pumping. Other options include using a complex absorbing potential (CAP), [33, 187–190] heuristic lifetimes added to the unbounded virtual states for real-time TDDFT [84, 90] and damped response theory[191, 192]. CAPs, however, are not norm-preserving and will only broaden out, not remove, intruder peaks. Moreover, CAPs with Gaussian basis sets are challenging to use due to unphysical leakage[79, 193] and may result in spuriously large ionization if used incorrectly. Another method for removing intruder peaks is to compute the contributions of the molecular orbitals (MOs) to a particular absorption peak via dipole pairs [85, 89, 91], transition densities[194], or the wavepacket autocorrelation function [195], but this can involve cumbersome post-processing of the spectrum. Ad-

ditionally, time-varying populations and strong field Stark shifts may make the projection onto ground state MOs invalid. In principle, summing over all virtual orbitals negates this problem, but in practice this becomes prohibitively slow for systems with a high DOS[91]. Propagating in a subset of MOs that excludes these "continuum" states would remove these unphysical transitions, but it can be difficult to distinguish a priori between physical and unphysical virtual orbitals based solely on an SCF calculation. Additionally, since the time-consuming part of calculations are formed in the atomic orbital (AO) basis, propagating in a limited subspace would yield minimal savings in terms of computational effort. Chopping away some atomic orbitals (e.g., diffuse and/or high angular momentum) is an alternative, but can have a deleterious effect on spectra. Inclusion of unphysical high energy virtual states does not affect the electron dynamics resulting from a pump laser, unless the fields are strong enough to ionize, in which case a complex absorbing potential (CAP), or similar, is required.

To address these issues, we propose a dipole filter approach. Similar to the selective perturbation, we use a filtered dipole operator (matrix) to weed out the transition amplitudes between all unwanted orbitals. This method generates a dipole moment that only contains dynamics associated with a particular core-level edge of interest (e.g., K-edge). Since this is only applied when computing the expectation value of the dipole moment, it keeps the interaction with the laser field unchanged and does not require more computational effort. As will be shown, without such correction transient spectra are qualitatively wrong when using atom-centered basis sets. Following methodology details, we demonstrate the intruder peak problem in the L-edge XANES of unpumped argon, where the physical origins of intruder peaks for the case of weak-field excitation are highlighted.

Next, we present the nitrogen and oxygen K-edge XTAS of UV-pumped aminophenol (C_6H_7NO), which serves as a demonstration of the intruder peak problem in molecular systems. Finally, we also show how this method can be used to compute linear and attosecond transient L-edge absorption in a bulk-mimicking α-quartz (SiO_2) cluster.

3.2. Methods

Generally speaking, real-time electronic structure can be used to compute absorption spectra by integrating some form of the time-dependent Schrödinger equation in time[115, 116]:

$$i\frac{\partial \left|\Psi(t)\right\rangle}{\partial t} = \hat{H}(t)\left|\Psi(t)\right\rangle \tag{3.1}$$

For the case of TDDFT with N electrons in a restricted Kohn-Sham framework, for example, this consists of $N/2$ single-particle equations:

$$i\frac{\partial \psi_j(r,t)}{\partial t} = \hat{H}_j(t)\psi_j(r,t)\ ,\ j = 1,\ldots,N/2 \tag{3.2}$$

with the DFT Hamiltonian for the j^{th} orbital is given by

$$\hat{H}_j(\rho,t) = -\frac{1}{2}\bigtriangledown_j^2 + \hat{V}_{\text{eN}}(R) + \int dr' \frac{\rho(r',t)}{|r-r'|} + \hat{V}_{\text{field}}(t) + \hat{V}_{xc}[\rho(t)]$$

where $\hat{V}_{\text{eN}}$ contains the nuclear-electron interaction within Born-Oppenheimer approximation. The exchange-correlation potential $\hat{V}_{xc}[\rho]$ corrects the fictitious non-interacting particles to the realistic system. Formally this depends on the complete history of the density, but here we use the adiabatic (local-in-time) approximation. Finally, $\hat{V}_{\text{field}}(t)$ is the coupling between the electrons and applied electric field $E(t)$, which for this work we use the dipole approximation:

$$\hat{V}_{\text{field}}(t) = -D \cdot E(t) \tag{3.3}$$

In this paper, for the time-propagation we use the RT-TDDFT module in NWChem [196]. This involves solving the equation of motion Eq. 3.2 using the density matrix formalism, which in the canonical orbital (CO) basis corresponds to the von Neumann equation with $m \times m$ matrices:

$$\frac{\partial \mathbf{P}'}{\partial t} = -i[\mathbf{F}'(\mathbf{t}), \mathbf{P}'(\mathbf{t})] \tag{3.4}$$

where m is the number of COs, and $\mathbf{P}'$ and $\mathbf{F}'$ are the density and Fock matrix in CO basis, respectively. This is propagated using a second order Magnus (exponential midpoint) method. For details, see Ref. [134]. Computing an absorption spectrum from a RT simulation typically involves broadband excitation using a laser pulse that is narrow in time. If interested in linear response, this magnitude of this applied electric field has to be much smaller than the intramolecular electric field experienced by the electrons. RT-TDDFT may be valid for strong fields (e.g., nonlinear properties, strong-field ionization) but this may stress the validity of the exchange-correlation functional [79, 84].

The resulting time-dependent dipole moment $\mu(t)$ for different directions ($\lambda = x, y, z$) is calculated as,

$$\mu_\lambda(t) = \mathrm{Tr}[\mathbf{P}(t)\mathbf{D}_\lambda] \tag{3.5}$$

where $\mathbf{P}$ and $\mathbf{D}$ are the density and dipole matrix in atomic basis sets. The dipole moment $\mu(\omega)$ and electric field $E(\omega)$ in frequency domain can be constructed using Pade approximants to the Fourier transform, which reduces the required simulation time needed to get converged spectra [85]. After transforming the electric field and dipole moment the same way, the polarizability tensor is computed as

$$\alpha_{\lambda\lambda'} = \frac{\mu_\lambda(\omega)}{E_{\lambda'}(\omega)} = \frac{\mu_\lambda(\omega) E_{\lambda'}(\omega)^*}{|E_{\lambda'}(\omega)|^2} \tag{3.6}$$

Finally, the optical density, $S_\lambda(\omega)$, is calculated from an isotropic average of the on-diagonal elements of α,

$$S_{\lambda\lambda'}(\omega) = \frac{4\pi\omega}{3c}\mathrm{ImTr}\left[\alpha_{\lambda\lambda'}\right] \tag{3.7}$$

where c is the speed of light ($c = 137$ a.u.).

As discussed previously (and shown in Sec. 3.3), using this atom-centered basis set approach for inner-shell spectra may give unphysical intruder peaks when applied to anything but the simplest system. To remove these unphysical transitions we propagate the equation of motion Eq. 3.4 using the regular operators and expressions, but when computing the expectation value of the dipole moment $\mu(t)$, we use a filtered version of the dipole operator $\mathbf{D}$. This filter is chosen to only include contributions from a particular subset of occupied core orbital(s). The filtered dipole operator is constructed in the ground state KS molecular orbital (MO) basis by converting from the AO to MO basis. In this basis, the element D_{ij}^{MO} corresponds to the transition dipole between the i^{th} and j^{th} molecular orbitals. The filtered dipole matrix $\widetilde{\mathbf{D}}^{\mathrm{MO}}$ is obtained by manually zeroing all rows and columns other than those involving particular occupied core-levels of interest in $\mathbf{D}^{\mathrm{MO}}$. For example, the filtered dipole matrix in the MO basis for just the i^{th} core-level orbital is,

$$\widetilde{\mathbf{D}}_i^{\mathrm{MO}} = \begin{pmatrix} 0 & \cdots & D_{1i}^{\mathrm{MO}} & \cdots & 0 \\ \vdots & & \vdots & & \vdots \\ D_{i1}^{\mathrm{MO}} & \cdots & D_{ii}^{\mathrm{MO}} & \cdots & D_{im}^{\mathrm{MO}} \\ \vdots & & \vdots & & \vdots \\ 0 & \cdots & D_{mi}^{\mathrm{MO}} & \cdots & 0 \end{pmatrix} \tag{3.8}$$

We use the over-tilde to denote filtered quantities. Note that $\widetilde{D}_{ii}^{\mathrm{MO}} = 0$ due to parity,

but we show this element for clarity. Each sparse filtered MO dipole matrix is then transformed back into a dense AO representation (see Appendix B for this transformation procedure). Since this filter is built from only the ground state MOs it only needs to be computed once, after which it can be used to compute the time-dependent filtered dipole moment,

$$\widetilde{\mu}_{i,\lambda}(t) = \mathrm{Tr}[\mathbf{P}(t)\widetilde{\mathbf{D}}_{i,\lambda}] \tag{3.9}$$

where i is the occupied (inner-shell) orbital of interest, and λ denotes the polarization.

3.3. Results

We now show representative examples of cases where transient XAS spectra computed using RT-TDDFT have significant intruder peak errors, and how the dipole filter remedies this issue. These results both serve as words of caution, and as a way to validate our method for using a filtered dipole during the time propagation.

3.3.1. L-edge X-ray Absorption of Argon

We first start with a simple example of L-edge absorption of a single Ar atom without pumping, which serves as a demonstration of the intruder peak problem in linear spectra. Since the 2s and 2p orbitals are close in energy, their absorption spectra are interleaved. Thus, we report the entire L-edge, rather than L_1 and $L_{2,3}$ separately. These simulations do not include spin-orbit effects. The def2-TZVPPD basis set and PBE0 [197] exchange correlation functional are used for these calculations. For the LR calculations, 200 roots were computed using the Ar 2s and 2p occupied orbital (energy window between -13 Ha to -8 Ha). In the real time calculations, a weak kick field with the form of delta function $E(t) = A\delta(t-t_0)$ was applied to excite the system, where t_0 is the center and A is

the amplitude of the kick. For generality, we used a time-shifted kick, although the spectrum is independent of t_0 if the signal processing is done correctly. Here we chose a field centered at $t_0 = 10$ au (0.24 fs) with an amplitude of $A = 0.0001$ au, which is weak enough to directly compare to the LR results. Due to symmetry, we calculated the excitation with only an x-polarized electric field. A time step of $\Delta t = 0.01$ au (2.4×10^{-4} fs) was used with a total simulation time of $t_{max} = 300$ au (7.25 fs). The time-dependent dipole moment was exponentially damped with $e^{-(t-t_0)/t_d}$, t_d =10 au (full width at half maximum/FWHM $\simeq$ 5.44 eV) before Pade processing [85] to give the peaks Lorentzian line shapes. The LR spectrum was broadened with same width (5.44 eV = 0.2 Ha).

The resulting spectra are shown in Fig. 3.1(a) for LR-TDDFT (green), unfiltered RT (gray), and filtered RT (dashed). In the LR spectrum, the first two peaks at 241 eV and 253 eV correspond to transitions from 2p to 3d and 4d orbitals. The bright peak at 296 eV arises from 2p $\rightarrow$ 5d with a small contribution from 2s $\rightarrow$ 4p. Also the absorption peaks at 316 eV and 352 eV in high energy region capture the excitation from 2s to 5p and 6p, respectively. The corresponding RT spectrum without a filter is shown as a solid gray line. The unfiltered RT spectrum is similar to the LR, except for two intruder peaks that appear between 256-284 eV (discussed below). The dashed black line in Fig. 3.1(a) shows the resulting RT spectrum using a filtered dipole operator built from only contributions from the second and third molecular orbitals (2s, $2p_x$). Note that for a x polarized kick, the fourth and fifth ($2p_y$ and $2p_z$) MOs are not involved in the dynamics. The spectrum computed using this filtered dipole operator is essentially indistinguishable from the LR one.

Next we discuss the physical origins of these intruder peaks. Since these transition

energies are much less than the K-edge (∼3.2 keV), they must arise from transitions from (3s, 3p) occupied orbitals to high-lying virtual states. To confirm this, we decomposed the

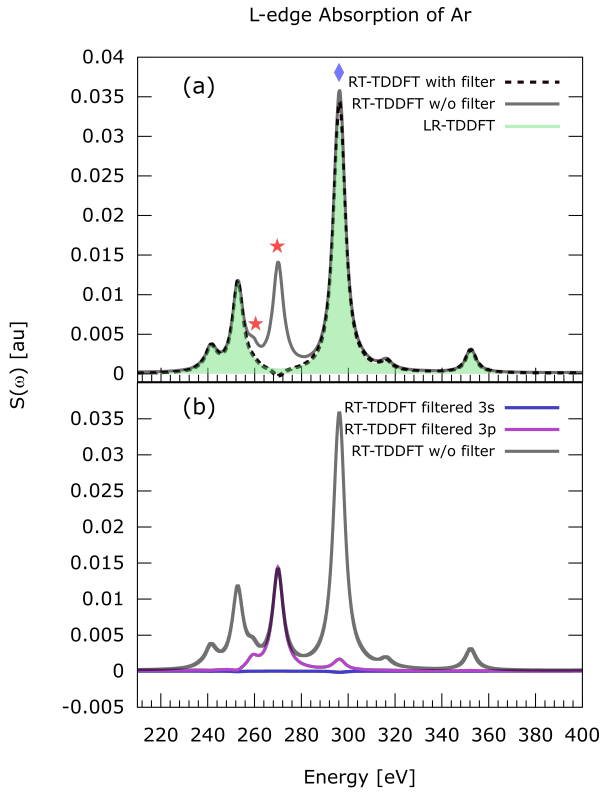

Figure 3.1. (a) The L-edge absorption spectra in Ar calculated from filtered RT-TDDFT (dashed black line), conventional RT-TDDFT (solid gray line) and windowed LR-TDDFT (filled green curve). The LR and RT+filter agree well, while the unfiltered RT has two intruder peaks between 256–284 eV (red stars). (b) The comparison between the unfiltered L-edge spectrum calculated from conventional RT-TDDFT (gray line) and the absorption spectra from 3s orbital (blue line) and $3p_x$ orbital (purple line). The unphysical intruders at 260 eV and 270 eV arise primarily from transitions from the 3p orbitals to high energy virtuals.

spectrum into orbital contributions by performing two simulations, one with a dipole filter only applied to the 3s occupied orbital, and the other applied only to the $3p_x$, and determined the exact contribution via LR-TDDFT calculation. As shown in Fig. 3.1(b), the intruder peak at 260 eV is a result of a 3p→8s transition, and the 270 eV intruder is primarily a 3p→6d excitation. Additionally, there is a small (3s,3p) contribution to the

L-edge peak at 296 eV (blue diamond) which slightly increases the absorption amplitude. Summarizing the argon atom results, it is interesting to note that even in this simple case of a single atom, simply computing the spectrum via a kick excitation gives qualitatively incorrect spectra, albeit with easily identified intruders. As we show next, however, as the number of basis functions increases, the intruders become more numerous and result in significant errors in the simulated spectra.

One thing to note is that the dipole filter can give negative absorption peaks, which are exhibited at around 270 eV for the L-edge absorption in Fig.3.1(a) and 296 eV for 3s orbital in Fig.3.1(b). Unlike the emission peaks in conventional spectra, these negative peaks are only a component of the total absorption peaks and do not possess clear physical meanings. This is because that the dipole moments computed between Kohn-Sham orbitals are not an actual physical observable. Whereas a total spectrum is positive, each individual contribution may be positive or negative in principle. However, these negative peaks are very small for inner-shell spectra, because core spectra generally involve only a small number of occupied orbitals. On the other hand, applying a dipole filter for an outer-shell or valence excitation would likely give unphysical results, as valence transitions typically have significant contributions from multiple occupied orbitals.

3.3.2. K-edge X-ray Absorption Spectroscopy of Aminophenol

Next, we show results for the oxygen and nitrogen K-edge transient XANES in aminophenol, which is a promising target for transient absorption studies due to the presence of an oxygen and a nitrogen atom at opposite ends of the molecule. We have previously reported simulated attosecond XTAS in this molecule [92], where the intruder

problem was circumvented by only considering a probe pulse polarized perpendicular to the plane of the molecule, and also by only considering a narrow energy range that fortuitously did not have intruder peaks. Here, we generalize the results to x, y, and z-polarization over a wider energy range.

The def2-TZVP basis and PBE0 functional were used for all calculations, both for geometry optimization and for LR and RT-TDDFT simulations. Before presenting the XTAS of the excited molecule, we first computed the ground state XANES spectra to evaluate the intruder problem in the unpumped molecule. The RT-TDDFT time step was $\Delta t = 0.04$ au (9.6×10^{-4} fs) and each x, y, z polarized simulation was run up to $t_{\max} = 700$ au (16.9 fs). The probe was taken to be a δ-function in time centered at $t_0 = 10$ au with field amplitude of 0.0001 au. The time signals were processed by exponential damping with $t_d = 100$ au (FWHM 0.544 eV), followed by Pade approximants to the Fourier transforms [85]. The resulting oxygen and nitrogen K-edge RT-TDDFT spectra, computed using Eqs. 3.6-3.7, are shown in Fig. 3.2 as gray lines in (a) and (b). The corresponding linear response TDDFT spectra were computing for 80 roots using energy windowing with cutoffs of -18 Ha and -13 Ha, respectively, and artificially broadened by 0.544 eV. The LR-TDDFT spectra were also shifted by 0.12 eV to match the RT-TDDFT spectra, to correct for finite time step effects in the RT spectra. Smaller Δt values would make this unnecessary. Our results are not shifted to match experiment as is commonly done in TDDFT[116], since we do not make direct comparison to experiments.

In the oxygen K-edge absorption in Fig. 3.2(a), besides the significant intruder peaks in the pre-edge region (500 – 520 eV in this plot), the peaks from conventional RT-TDDFT also have higher absorption strength in the rising-edge region compared

with the spectrum calculated with LR-TDDFT and RT-TDDFT with a filter. This is due to intruder peaks that overlap physical peaks. The nonphysical peaks come from transitions from the nitrogen K-edge to high energy virtual states (see Appendix B for details). Fig. 3.2(b) shows the nitrogen K-edge absorption spectra for aminophenol. The unfiltered RT suffers from intruders that involve transitions from the carbon K-edge to the poorly-described continuum states (see Appendix B for details). The corresponding RT spectra computed using a filtered dipole operator (O 1s only, N 1s only) are shown as purple curves in Fig.3.2. There is essentially quantitative agreement with the LR results, save for a slight difference in absorption magnitudes, likely arising from errors due to integrator time step.

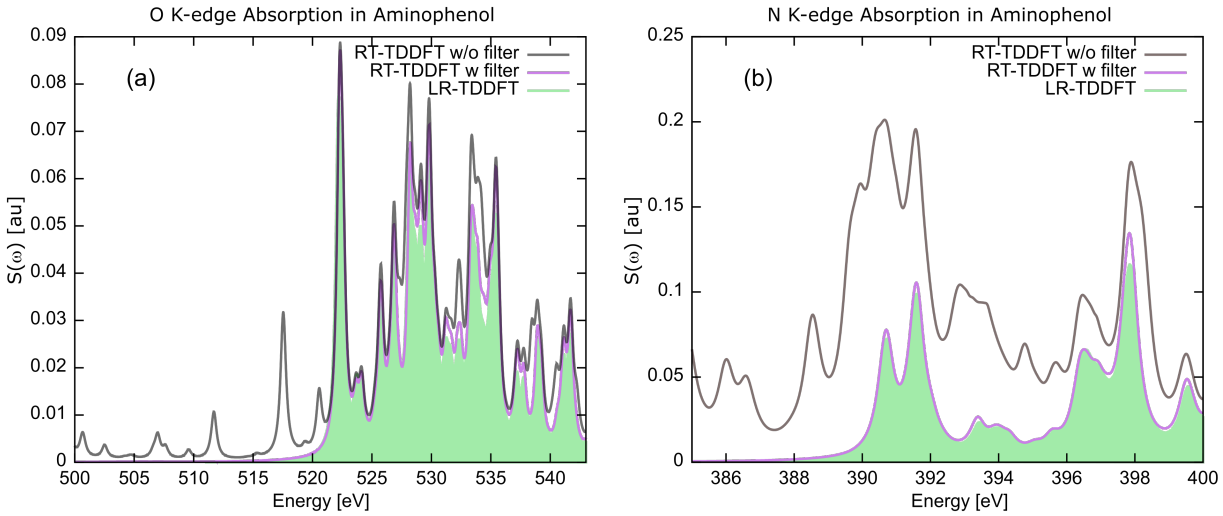

Figure 3.2. The oxygen (a) and nitrogen (b) K-edge absorption for aminophenol computed using un-filtered (gray solid line) RT, filtered RT (purple solid line), and LR-TDDFT (filled green). The unfiltered simulations have intruder peaks in the pre-edge region as well as unphysically large absorption amplitude in rising-edge region, whereas the filtered RT spectra agree well with LR ones.

These spectra exemplify the issues that Gaussian basis-set real-time methods face for K-edge spectra in molecules. First, K-edge spectra are likely contaminated with con-

tributions from lower energy edges, e.g., for a molecule containing C, N, O, the oxygen K-edge will be contaminated with N features, the nitrogen K-edge with C features. Second, although some intruder peaks occur at energies lower than the physical pre-edge features and can be easily identified by their position, in general the peaks can be interleaved within the spectrum, resulting in both obvious intruders as well as incorrect oscillator strengths. These cannot be easily remedied in an ad hoc way without some form of filtered signal. The effect of basis set on intruders in this system was also studied (see Appendix B). In this molecule, and in general, we observe that intruders are highly basis set dependent, but using a filtered dipole consistently removes them. In some, but not all cases, intruders can be fortuitously absent in small basis set calculations. In principle, one can use the basis dependence to determine the intruders, but since the physical peaks are also basis dependent, this can be difficult to do in practice.

Next, we present how this technique can be generalized to attosecond X-ray transient absorption in this molecule. As in Ref. [92], we prepared an initial state by putting 0.3 electron on the $-NH_2$ group and 0.3 charge on $-OH$ group using constrained density functional theory [133] in order to approximately mimic a $\pi \to \pi^*$ pump pulse. The resulting dynamics involve an oscillation of charge from one end of the molecule to another with two main frequencies 0.2 au (0.76 fs period) and 0.43 au (0.35 fs period). Fig. 3.3(a) shows the change in the number of electrons around the oxygen with respect to the ground state: $\Delta N_{\mathrm{O}}(t) = N_{\mathrm{O}}(t) - N_{\mathrm{O}}(t = 0)$, where the number of electrons is computed by integrating the density around the atom:

$$N_{\mathrm{O}}(t) = \int_{x_1}^{x_2} dx \int_{-\infty}^{\infty} dy \int_{-\infty}^{\infty} dz \, \rho(x, y, z) \tag{3.10}$$

with x_1 and x_2 chosen to correspond to the positions -0.15 Å to $+0.06$ Å from the location of the oxygen atom. $N_O(t)$ shows oscillations primarily at the electron dynamics frequency, with a max depletion and excess charge on the order of 15% of an electron. The XTAS spectra for this process were then computed using a time step of $\Delta t = 0.06$ au (1.4×10^{-3} fs) and a $t_{\max}$ of 650 au (15.7 fs), with a δ-function probe $E_0\delta(t-\tau)$ in the x, y, z for a range of time delays τ. The dipole signal without the probe was subtracted

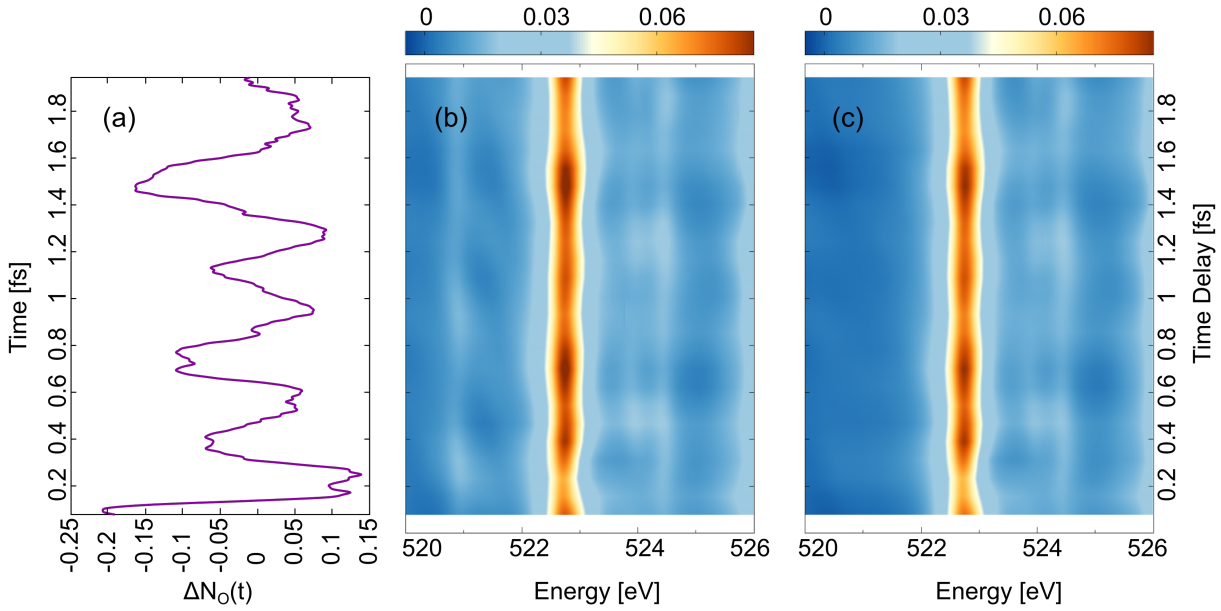

Figure 3.3. Simulated attosecond transient oxygen K-edge X-ray absorption in pumped aminophenol. (a) The change in the number of electrons around the oxygen atom over time following the pump excitation. The oxygen K-edge transient spectra without (b) and with (c) a dipole filter in the region corresponding to O $1s \rightarrow \pi^*$ transition. Both methods yield an oxygen K-edge TAS with modulations correlated to the localized density change around oxygen, but the unfiltered spectrum exhibits extra unphysical peaks and absorption strength.

from the $\mu(t)$ for each value of time delay[92, 180], then transformed using Pade approximants following exponential damping via $e^{-(t-\tau)/t_d}$, $t_d = 100$ au (FWHM 0.544 eV). Fig. 3.3 shows the resulting transient spectra of oxygen K-edge with and without the dipole filter applied. The energy range shown covers the region around the O$1s \rightarrow \pi^*$

transition, which occurs at 523 eV for this basis and DFT functional. Both filtered and unfiltered O K-edge TAS have similar modulations with respect to τ. The modulations in the O1$s \rightarrow \pi^*$ transition peak are correlated with $N_O(t)$: when extra electron density is on the oxygen, the absorption strength decreases and vice versa. Although qualitatively similar, the unfiltered oxygen K-edge absorption (Fig. 3.3(b)) not only has higher absorption strength at 523 eV, but also has an intruder around 521 eV, which can be easily mistaken as a physical transient absorption modulation. The filtered spectrum (c) is free of these artifacts.

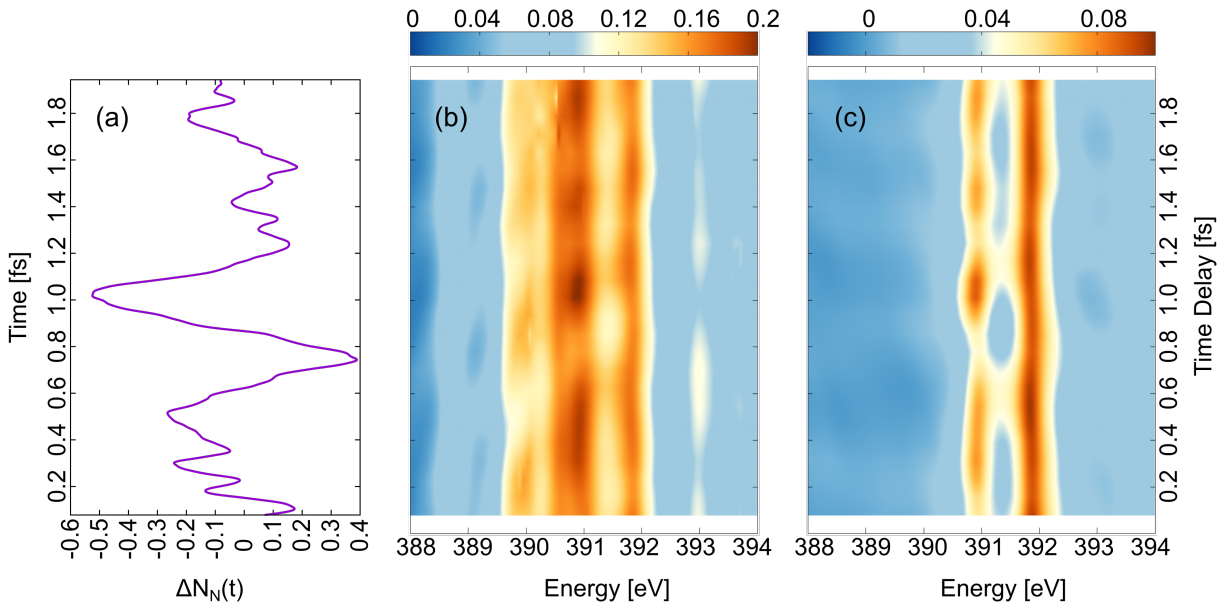

Figure 3.4. Simulated attosecond transient nitrogen K-edge X-ray absorption in pumped aminophenol. (a) The change in the number of electrons around the nitrogen over time resulting from the pump. In the unfiltered case (b), the N1$s \rightarrow \pi^*$ transition is obfuscated by the intruders, leading to a congested spectrum with unphysical modulations unrelated to the electron dynamics. For the filtered case (c), the spectrum exhibits modulations that are correctly correlated with the local density around the nitrogen atom.

Next, Fig. 3.4 presents the transient nitrogen K-edge near-edge spectrum, along with (a) the instantaneous change in the number of electrons on the nitrogen atom,

$\Delta N_{\mathrm{N}}(t)$ which is integrated around the position of the nitrogen atom between -0.35 Å and +0.38 Å in eq. 3.10. The unfiltered spectrum (b) has multiple intruder peaks in both the pre-edge range (388-389 eV), as well as in the vicinity of the target N $1s \rightarrow \pi^*$ at 391 eV. These peaks exhibit unphysical modulations with respect to time-delay, such as the intruder at 390 eV that is incorrectly enhanced at times when there are more electrons on the N atom. The combination of spectral congestion and unphysical modulations make this transient spectrum essentially incomprehensible. On the other hand, the filtered N K-edge TAS shows only physical absorption peaks that have clear modulations related to the dynamics. The N $1s \rightarrow \pi^*$ transition at 391 eV has the expected anti-correlation with the number of electrons, such that times with reduced density on N give stronger absorption strengths. Moreover, the filtered XTAS shows clear modulations in the N $1s \rightarrow \sigma^*$ transition at 392 eV. Since this transition involves virtual orbitals that are not significantly populated by the "pump", these modulations are weaker. The nitrogen K-edge TAS is more sensitive to intruders than the oxygen K-edge, since the intruders in the nitrogen spectrum arise primarily from the carbon K-edge as demonstrated in the unpumped case (see Appendix B). These peaks involve multiple nearly degenerate carbon sites along the length of the molecule. The oxygen K-edge, in contrast, has intruders mostly from the nitrogen K-edge, which is spatially localized on the opposite end of the molecule.

3.3.3. Si L-edge Absorption of α-Quartz Cluster

Next we demonstrate how intruder peaks can be a severe problem in transient inner-shell spectra of solids, and how a filtered dipole addresses this issue without affecting the interaction of pump on the material. For this, we use the case of infrared (IR) pump

/ extreme UV (XUV) probe transient absorption of α-quartz (SiO_2). As a ubiquitous component in optical [198] and electronic devices [199, 200], SiO_2 has drawn many research interests both experimentally and theoretically [90, 201, 202]. The simulations in this study utilize a finite cluster that is carved out of a bulk geometry in order to avoid computational costs and is described in detail in Ref.[90]. This bulk mimicking cluster has a molecular formula of $Si_5O_{16}H_{12}$ with added hydrogen atoms bonded to the boundary oxygen atoms in order to create charge consistency in the finite structure. For all our simulations, we used def2-TZVPPD atom centered basis set for describing the central absorbing silicon atom, def2-SVPD for the bridging oxygen that are connected to the central Si, Stuttgart RLC ECP for the bridging silicon and boundary oxygen; and finally, STO-3G for capping hydrogen atoms. The structure and basis set details are given in the Appendix B. LC-PBE0*, a tuned range-separated hybrid DFT functional, was employed for describing the Coulomb potential. Three parameters were used for tuning this functional: α specifies the fraction of HF exchange contribution for describing the long-range Coulomb interaction, β denotes DFT functional portion and is well-suited for short-range description near the nucleus, and μ signifies how fast the tuned functional switches from HF-exchange to DFT. These parameters are varied in accordance to Eq. 3.11. For each calculation the ground state total energy and ionization potential (IP) of the HOMO are computed. Using Koopmans theorem, the parameters that give the lowest difference between ΔSCF and IP_{HOMO} are picked for all absorption simulations [79, 90, 203]. The tuned parameters for SiO_2 are $\alpha = 0.515$, $\beta = 0.485$, and $\mu = 0.101$ au^{-1}.

$$\frac{1}{r_{12}} = \frac{\alpha + \beta\,\mathrm{erf}(\mu r_{12})}{r_{12}} + \frac{1 - [\alpha + \beta\,\mathrm{erf}(\mu r_{12})]}{r_{\ 12}} \tag{3.11}$$

A narrow Hann pulse with a $\sin^2$ envelope shape and polarized in the z-direction of the cluster was applied to simulate absorption, and is specified in Eq. 3.12.

$$E(t) = \begin{cases} 0, & t < 0 \\ A_0 \sin^2[\pi/W[t - (t_0 - W/2)]] \sin(\omega_0 t), & t > 0 \end{cases} \tag{3.12}$$

where the width of the envelope $W = 5$ au (0.12 fs), center $t_0 = 10$ au (0.24 fs), frequency $\omega_0 = 4.1$ au, and field amplitude $A_0 = 0.0001$ au. The time step used was $\Delta t = 0.2$ au (0.005 fs) and the total simulation time was $t_{\max} = 1323$ au (32 fs). The time-dependent dipole data was damped with τ =75 au (FWHW 0.726 eV) and padded with 5×10^4 zeros. The electric field and computed dipole signals were then Fourier transformed, and Eqs. 3.6 and 3.7 were used compute the XUV absorption spectrum.

Before discussing the pump/probe case, we present the linear absorption spectrum. Fig. 3.5 shows the Si L-edge spectrum simulated using RT-TDDFT and compared to the experimentally measured spectrum [204]. It can be seen that the filtered result gives good agreement with experiment by correctly predicting Si 2p $\rightarrow$ Si 3s transition (peak A) in the rising-edge region and Si 2p $\rightarrow$ Si 3p* transition (peak B), which is allowed, despite the Laporte rule, as a result of the deformed p-orbitals that exist in the tetrahedral geometry of α-quartz [90, 198, 204, 205]. The main difference between the experiment and simulation around 106 eV is due to lack of spin-orbit effects in the simulation ($2p_{3/2}$, $2p_{1/2}$). The unfiltered spectrum, on the other hand, has a severe intruder problem, and is qualitatively incorrect.

Next, we show a proof-of-principle simulations for transient absorption spectroscopy in this system for three time delays during a strong IR pump/XUV probe

transient metallization experiment. [3] The pump field has the same shape as the probe pulse (Eq. 3.12) but with center frequency, center time, width and field strength of 0.057 au (800 nm), 350 au (8.47 fs), 550 au (13.3 fs) and 0.01 au (0.51 V/Å), respectively. The corresponding time delay is defined as $\tau = t_0^{\text{probe}} - t_0^{\text{pump}}$.

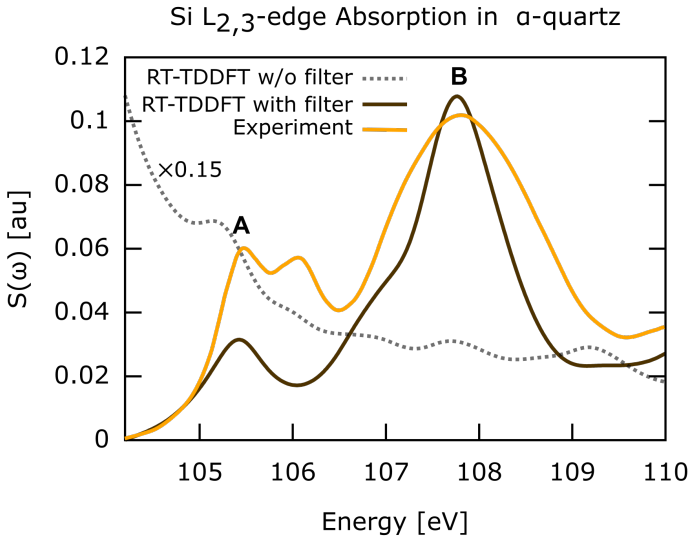

Figure 3.5. The Si $L_{2,3}$-edge XUV absorption spectrum for α-quartz is shown with orange line that is digitized from experiment [204], the dashed gray line shows the unfiltered RT-TDDFT spectrum, and the solid black line is the filtered RT-TDDFT result. Without a filter, the intruder peaks render the spectrum qualtitatively incorrect, whereas the filtered RT-TDDFT calculation and experiment spectrum show reasonable agreement.

Fig. 3.6 shows the transient spectroscopy of α-quartz with an IR pump pulse at three different time delays without (a) and with (b) a dipole filter. In these spectra, the absorption when the pump field is zero (equivalent to $\tau = -\infty$) is shown as a black dashed line and the transient spectra when the pump is ramping up ($\tau = -3.5\ fs$) and at the maximum ($\tau = 0\ fs$) are shown using orange solid and red solid lines, respectively. Absent a filter, as shown in Fig. 3.6 (a) the physical peaks are impossible to distinguish and the XANES modulations cannot be used to interpret the dynamics. However, in Fig. 3.6

(b) it can be seen clear modulations for both Si 2p → Si 3s transition and Si 2p → Si 3p* transition that as the dressing pump-pulse increases, the absorption decreases. This is related to the conduction band (virtual populations), being transiently populated by the strong IR field, which results in a drop absorption. A manuscript more fully detailing this effect is in preparation [206]. These results clearly demonstrate how a filter is especially important when computing transient inner-shell spectra for bulk-mimicking clusters, and is likely generalizable to any system with a high density of states.

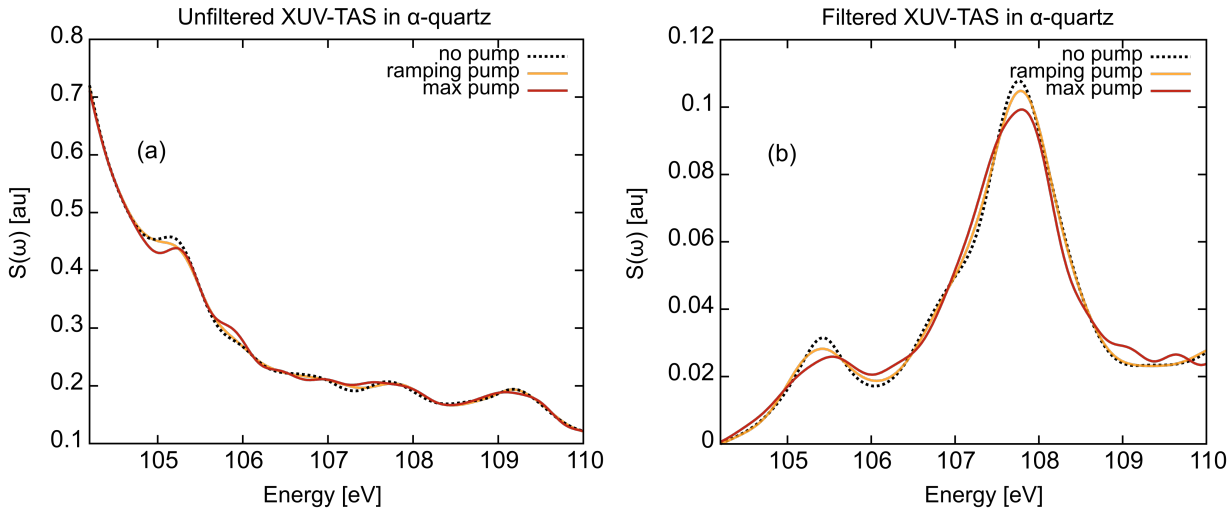

Figure 3.6. Simulated XUV transient spectroscopy of α quartz computed without (a) and with (b) a filter for three different time delays: when the pump is off ($\tau = -\infty$, black dashed line), ramping ($\tau = -3.5\ fs$, solid orange line) and maximum ($\tau = 0\ fs$ solid red lines).

3.4. Conclusions

In summary, real-time methods with atom-centered basis sets are well-suited for simulating transient inner-shell spectra, but can suffer from deleterious intruder peaks, especially in systems with a high density of states. This problem is more acute than in simple absorption, since intruders exhibit nonphysical modulations as a function of time-delay, which makes interpretation essentially impossible. We have presented a filtered

dipole operator technique for removing these intruders, where the expectation value of the dipole moment only includes specific core orbital contributions. This results in transient spectra that exclusively contain a particular inner-shell edge of interest, and do not have intruder peaks. As representative examples of molecular and solid state cases, we simulated the transient spectra in UV-pumped aminophenol and IR-pumped α-SiO_2. For aminophenol, standard RT-TDDFT was found to give somewhat reasonable results for the transient oxygen K-edge case, but the nitrogen K-edge has a catastrophic intruder problem. For the bulk-mimicking cluster case, the intruder peak problem likewise makes the spectrum incomprehensible. In both cases, dipole filtered RT-TDDFT gives transient spectra that correctly reflect the attosecond electron dynamics in the system. Going forward, addressing the intruder problem in transient spectra allows for simulation of transient inner-shell spectra in a wide range of systems subjected to a variety of different pumps. Simulations of this kind are valuable for interpreting transient absorption X-ray experiments, as they can help bridge from time-delay to real-time/actual dynamics in a molecule.

Chapter 4. Mapping Static Core-Holes and Ring-Currents with X-ray Scattering

4.1. Introduction

The recent emergence of ultra-short pulsed X-ray free-electron lasers (XFELs) has introduced new tools to study chemical processes, in particular photochemical or photophysical events. X-ray scattering experiments, limited in the past to crystalline samples, have become possible for all states of matter, and even low density, gaseous samples can be now studied as a consequence of the high peak brightness of these new X-ray sources. The spatial resolution and the short duration of these X-ray pulses has enabled gas-phase time-resolved X-ray scattering experiments where the time evolution of the electronic [46] and nuclear [47, 49] degrees of freedom in the system can be measured after ionization or excitation. These advances have made time-resolved X-ray scattering a useful tool in the study of complex photochemical reaction dynamics [207], where the preparation [208], evolution[209] and relaxation of vibrational wavepackets far from equilibrium [210] can be tracked by using a direct analysis of the X-ray signals in time. The experiments have a sensitivity that is similar to MeV ultrafast electron diffraction[211, 212]. Extensive theoretical studies have been also made in order to formulate a unified X-ray scattering theory [213–215] with a special attention to the time-resolved picture in atomic [110, 216–218] and molecular systems [113, 114, 219].

Even though the theoretical formulation of time-resolved X-ray scattering has provided most of the tools to analyse nuclear [214, 220, 221] and electron dynamics [109, 222,

Chapter 4.1-4.3.1 and 4.4 are reproduced with modifications from Carrascosa, A. M., Yang, M., Yong, H., Ma, L., Kirrander, A., Weber, P. M., & Lopata, K., 2021. Mapping static core-holes and ring-currents with X-ray scattering. Faraday Discussions, 228, 60-81. with permission from the Royal Society of Chemistry.

223] in X-ray experiments, the manifestation of these effects, in particular with regards to electron dynamics in excited polyatomic systems [224–226] remains a very active research area. The slow evolution of the nuclear degrees of freedom and the fast electron rearrangement in these systems require a compromise between resolution and sensitivity in the X-ray scattering signal measurement, as well as accurate theoretical simulations to interpret the experimental results. It has been recently demonstrated theoretically that X-ray scattering for electron dynamics is primarily sensitive to the time-derivative of the density, rather than the instantaneous density [113, 114, 219] and electronic currents can be reconstructed from instantaneous resonant X-ray scattering signals [227]. That is, considering only the electron dynamics on an attosecond time scale, the dynamical information is primarily contained in the inelastic parts of the scattering while the elastic part remains unchanged. This arises from the coupling of the X-ray probe with the time-evolving system where only the coherent-mixed terms between different electronic states contribute [109]. In a more intuitive physical picture, since this derivative is proportional to the divergence of the electron currents, time-resolved X-ray scattering can be viewed as a probe of the curvature and magnitude of the electron flow in the system. The instantaneous electron density, on the other hand, appears only as a background. As a result, X-ray scattering studies can conveniently reveal dynamics in molecules that support divergent curved electron currents and manifest the evolution of current intensity.

Conjugated, ring-shaped molecules are intriguing candidates for scattering studies of electron dynamics, as recently demonstrated by [113] and [228], since their driven electron density travels in semi-circular currents that have appreciable divergence [229, 230]. Additionally, they have been used extensively as targets for electron and X-ray scat-

tering[47, 209, 231–233], and are readily functionalized with heteroatoms that allow for site-selective X-ray ionization [234–236]. The presence of heteroatomic centers, for example, can also lead to long-lived vibrational coherence preservation [48]. Additionally, ring molecules are ubiquitous in chemistry and form the basis for a wide range of applications including drug design[237, 238], agrochemistry[239, 240], material science[241, 242],and electronics [243, 244]. They also undergo ring-opening and similar processes, which are the subjects of intense interest due to their importance in general organic synthesis [245], synthesis of photobiological compounds [246, 247] or production of new materials [248]. The role of electron dynamics in these processes, however, remains relatively unstudied. Elucidating them is critical as they may, for example, affect the ring-opening and fragmentation pathways by dictating which bonds break during the reaction. Due to the complexity of the scattering signals, simulations are necessary for the interpretation of the resulting scattering patterns. Linear molecules, on the other hand, exhibit straightforward dynamics along the molecular scaffold and thus can serve as a prototypical system for investigating the electron motion and its corresponding scattering signals.

In this chapter, we present a detailed study of how gas-phase X-ray scattering can map the electron flows in both heteo-atom ring-shape and linear molecules. Hetero-atom ring molecules that contain oxygen, nitrogen and carbon atoms in different chemical environments play an important role in the synthesis of potential medicines including antitumor, antimicrobial, anti-infective, cardiovascular, and nervous system agents [249]. They can also undergo photoinduced ring-opening reactions, and is well-studied by theoretical simulations [250–252] and time-resolved photoelectron spectroscopy [250]. To demonstrate the ring and linear currents can be probed by X-ray scattering, we study the core-hole in-

duced and UV-pumped dynamics both in ring shape and linear molecules. Here we simulated the oxygen K-edge core-hole triggered dynamics in oxazole and carbon monoxide and UV-pumped electron motions in 4-aminohphenol as well as carbon monoxide. These proof-of-principle results aim to lay the foundation for future experiments probing both the electronic and nuclear degrees of freedom using X-ray ionization followed by X-ray scattering.

4.2. Theory

To simulate the core-hole processes and resulting scattering patterns, we use density functional theory (DFT) to construct a stationary core-hole, real-time time-dependent DFT to simulate the electron density evolution following ionization, and stationary and time-resolved X-ray scattering theories to generate the scattering signals. These methods are briefly described below.

4.2.1. X-ray scattering from a time-evolving electron density

In the context of a fixed-nuclei approximation and a detection window $\Delta\omega$ larger than the electronic transition energies of the molecule, the time-dependent differential scattering cross-section reads [109, 253],

$$\frac{d\sigma}{d\Omega} = \left(\frac{d\sigma}{d\Omega}\right)_{\mathrm{Th}} W(\Delta\omega) \int I(t) \left\langle \Psi(\mathbf{r}^N, t)\right| \hat{L}(\mathbf{q}, \mathbf{r}^N)^\dagger \, \hat{L}(\mathbf{q}, \mathbf{r}^N) \left|\Psi(\mathbf{r}^N, t)\right\rangle dt, \tag{4.1}$$

where $\left(\frac{d\sigma}{d\Omega}\right)_{\mathrm{Th}}$ is the Thomson differential cross-section, $W(\Delta\omega)$ is the window function independent of the rovibrational energies that can be approximated as $W(\Delta\omega) \approx 1$, $I(t)$ is the probe-pulse intensity, $\Psi(\mathbf{r}^N, t)$ is the field-free wavepacket, $\hat{L}(\mathbf{q}, \mathbf{r}^N)$ the scattering operator defined as $L(\mathbf{q}, \mathbf{r}^N) = \sum_i^N e^{\mathrm{i}\mathbf{q}\mathbf{r}_i}$ where $\mathbf{q}$ is the momentum transfer vector or scattering vector that represents the momentum difference between the incident ($\mathbf{k}_0$) and scattered ($\mathbf{k}_1$) beams $\mathbf{q} = \mathbf{k}_1 - \mathbf{k}_0$, N is the number of electrons in the molecule, $\mathbf{r}$ the electron

coordinates and t is the time between the pump and probe pulses.

The field-free time evolution of the molecular electronic wavepacket $\Psi(\mathbf{r}^N, t)$ in atomic units can be expressed as,

$$\Psi(\mathbf{r}^N, t) = \sum_j C_j e^{\mathrm{i}E_j t} \psi_j(\mathbf{r}^N), \tag{4.2}$$

where $\psi_j(\mathbf{r}^N)$ are the N-dimensional populated electronic states with E_j eigenenergies and C_j expansion coefficients. Inserting this definition on the expression for the time-resolved differential scattering cross-section in Eq. (4.1) yields,

$$\begin{aligned} \frac{d\sigma}{d\Omega} = & \left(\frac{d\sigma}{d\Omega}\right)_{\mathrm{Th}} \int I(t) \sum_{i,j} C_i C_j \left\langle \psi_i(\mathbf{r}^N) \right| \hat{L}^\dagger(\mathbf{q}, \mathbf{r}^N) \hat{L}(\mathbf{q}, \mathbf{r}^N) \\ & \times \left| \psi_j^*(\mathbf{r}^N) \right\rangle e^{\mathrm{i}E_{ij}t} dt, \end{aligned} \tag{4.3}$$

with $E_{ij} = E_i - E_j$, which can be solved by either inserting the two-electron scattering operator $\hat{L}^{(2)}(\mathbf{q}, \mathbf{r}_1^N, \mathbf{r}_2^N) = e^{\mathrm{i}q(\mathbf{r}_1^N - \mathbf{r}_2^N)}$, only valid considering the large energy window, or the resolution of the identity in the electronic basis,

$$\hat{\mathbf{1}} = \sum_k^\infty \left| \psi_k(\mathbf{r}^N) \right\rangle \left\langle \psi_k(\mathbf{r}^N) \right|, \tag{4.4}$$

where k runs over all possible electronic states in the molecule. Combining Eq. (4.3) and Eq. (4.4) yields the general form for the expanded differential scattering cross-section [113],

$$\begin{aligned} \frac{d\sigma}{d\Omega} = & \left(\frac{d\sigma}{d\Omega}\right)_{\mathrm{Th}} \int I(t) \left(\sum_{i,k} C_i^2 \left| \int \rho_{ik}(\mathbf{r}) e^{\mathrm{i}\mathbf{q}\mathbf{r}} d\mathbf{r} \right|^2 + \right. \\ & \left. + \sum_{i<j,k} 2 C_i C_j \int \rho_{ik}(\mathbf{r}) e^{-\mathrm{i}\mathbf{q}\mathbf{r}} d\mathbf{r} \int \rho_{kj}(\mathbf{r}) e^{-\mathrm{i}\mathbf{q}\mathbf{r}} d\mathbf{r} \; e^{\mathrm{i}E_{ij}t} \right) dt, \end{aligned} \tag{4.5}$$

where we have introduced the density operator $\hat{\rho}(\mathbf{r}) = \sum_{n=1}^N \delta(\mathbf{r} - \mathbf{r}_n)$ between the electronic states $\psi_i(\mathbf{r}^N)$ to construct the one-electron densities $\rho_{ik}(\mathbf{r}) = \left\langle \psi_i(\mathbf{r}^N) \right| \hat{\rho}(\mathbf{r}) \left| \psi_k(\mathbf{r}^N) \right\rangle$.

The two terms in this expression carry different information about the time dependent X-ray scattering process: the first term corresponds to the time-independent contribution to the signal and acts as a constant background and the second term contains the so-called coherent-mixed terms [109, 114] which carry the time-dependent information in the X-ray scattering signal.

One can look at the difference between time t and $t = 0$ in Eq. (4.5) *i.e.* $\Delta\frac{d\sigma(t)}{d\Omega} = \frac{d\sigma(t)}{d\Omega} - \frac{d\sigma(0)}{d\Omega}$ to trace the time-evolution of the X-ray scattering signal in time, [113]

$$\begin{aligned}\Delta\frac{d\sigma(t)}{d\Omega} = \left(\frac{d\sigma}{d\Omega}\right)_{\mathrm{Th}} \int I(t) \Bigg(\sum_{i<j,k} -4C_iC_j\mathcal{F}[\rho_{ik}(\mathbf{r})]\mathcal{F}[\rho_{kj}(\mathbf{r})] \sin^2\left(\frac{E_{ij}t}{2}\right) \\ +2C_iC_j\mathcal{F}[\rho_{ik}(\mathbf{r})]\mathcal{F}[\rho_{kj}(\mathbf{r})]\mathrm{i}\sin\left(E_{ij}t\right)\Bigg)\, dt,\end{aligned} \tag{4.6}$$

where $\mathcal{F}[\rho(\mathbf{r})]$ is the Fourier transformation of the electron density. The coupled Fourier transformations can be further simplified by including the double Fourier transformation of the two-electron reduced density matrix $\Gamma(\mathbf{r}_1, \mathbf{r}_2)$,

$$\begin{aligned}\Delta\frac{d\sigma(t)}{d\Omega} = \left(\frac{d\sigma}{d\Omega}\right)_{\mathrm{Th}} \int I(t) \Bigg(\sum_{i<j} -4C_iC_j(\mathcal{F}^{(2)}[\Gamma_{ij}(\mathbf{r}_1, \mathbf{r}_2)]) \sin^2\left(\frac{E_{ij}t}{2}\right) \\ + 2C_iC_j(\mathcal{F}^{(2)}[\Gamma_{ij}(\mathbf{r}_1, \mathbf{r}_2)])\mathrm{i}\sin\left(E_{ij}t\right)\Bigg)\, dt,\end{aligned} \tag{4.7}$$

with,

$$\mathcal{F}^{(2)}[\Gamma_{ij}(\mathbf{r}_1, \mathbf{r}_2)]] = N + \int\int \Gamma_{ij}(\mathbf{r}_1, \mathbf{r}_2) e^{\mathrm{i}(\mathbf{r}_1 - \mathbf{r}_2)} d\mathbf{r}_1 d\mathbf{r}_2, \tag{4.8}$$

where N is the number of electrons in the molecule, as before.

Each term in Eq. (4.7) represents a different component of the scattering signal. The first term, expected to be small [113], is related to the time evolution of the one-electron density $\Delta\rho(\mathbf{r}, t)$,

$$\Delta\rho(\mathbf{r}, t) = -4 \sum_{i<j} C_iC_j\rho_{ij}(\mathbf{r}) \sin^2(\frac{E_{ij}t}{2}). \tag{4.9}$$

As an ansatz, we relate the second term to the the time derivative of the electron-density in Eq. (4.26),

$$\frac{d\rho(\mathbf{Q},t)}{dt} = 2\sum_{i<j} C_i C_j \mathcal{F}[\rho_{ij}^N(\mathbf{r})]\sin(E_{ij}t). \tag{4.10}$$

This relationship has been qualitatively demonstrated for a two-level superposition.[113] The density time-derivative is related to the electron-flux in the molecule (Eq. (4.29)) through the continuity relation in real-space,

$$\frac{d\rho(\mathbf{r},t)}{dt} = -\nabla\cdot\mathbf{j}(\mathbf{r},t). \tag{4.11}$$

4.2.2. X-ray scattering from a stationary state

The time-independent double differential cross section for X-ray scattering using Eq. (4.3) is [254],

$$\frac{d\sigma}{d\Omega d\omega'} = \left(\frac{d\sigma}{d\Omega}\right)_{\mathrm{Th}} S(\mathbf{q},\omega'), \tag{4.12}$$

where $\omega' = \omega_0 - \omega_1$, expressing the difference of energy between the incoming and scattered x-rays. The dynamic structure factor $S(\mathbf{q},\omega')$ is the key value in this equation as it describes the material response. It is given by,

$$S(\mathbf{q},\omega') = \sum_k \left|\langle\psi_k(\mathbf{r}^N)|\ \hat{\rho}(\mathbf{r})\,|\psi_0(\mathbf{r}^N)\rangle\, e^{-\mathbf{iqr}}\right|^2 \delta(E_k - E_0 - \hbar\omega') \tag{4.13}$$

where $|\psi_k(\mathbf{r}^N)\rangle$ and $|\psi_0(\mathbf{r}^N)\rangle$ are the final and initial electronic states with energies E_k and E_0 respectively. The transition energy $\hbar\omega' = E_k - E_0$, is often negligible compared to the energy of hard x-rays [255]. Therefore, $S(\mathbf{q},\omega')$ in Eq. (4.13) can be rewritten as $S(\mathbf{q})$ after the integration over w'. $S(\mathbf{q})$ can be expressed as the Fourier transform of the reduced two-electron density matrix $\Gamma(\mathbf{r}_1,\mathbf{r}_2)$, which yields,

$$S(\mathbf{q}) = \iint \Gamma(\mathbf{r}_1,\mathbf{r}_2)\ e^{\mathbf{iq}(\mathbf{r}_1-\mathbf{r}_2)}\ d\mathbf{r}_1 d\mathbf{r}_2 \ \ + \ \ N, \tag{4.14}$$

with N as the number of electrons in the molecule. From this equation, it can be noticed that total scattering is a combination of one and two-electron terms and electron correlation has a key importance in its calculation[256, 257]. The total scattering signal can be further decomposed by considering only the diagonal terms in Eq. (4.13) *i.e.* $\langle\psi_0|\ \hat{\rho}(\mathbf{r})\ |\psi_0\rangle\, e^{-\mathbf{iqr}}$, giving rise to the elastic component of X-ray scattering. This corresponds to the Fourier transform of the electron density,

$$S_{\mathrm{el}}(\mathbf{q}) = \left|\langle\psi_0|\ \hat{\rho}(\mathbf{r})\,|\psi_0\rangle\, e^{\mathbf{iqr}}\right|^2 = \left|\int \rho_{00}^{(N)}(\mathbf{r})\ e^{\mathbf{iqr}} d\mathbf{r}\right|^2 . \tag{4.15}$$

Here, $S_{\mathrm{el}}(\mathbf{q})$ is known as the elastic structure factor and $\rho_{00}^{(N)}(\mathbf{r})$ is the one-electron density of the stationary electronic state. The total *inelastic* scattering, $S_{\mathrm{inel}}(\mathbf{q})$, is usually defined as the difference between the total scattering and the *elastic* scattering, *i.e.*

$$S_{\mathrm{inel}}(\mathbf{q}) = S(\mathbf{q}) - S_{\mathrm{el}}(\mathbf{q}). \tag{4.16}$$

The limits for the elastic and inelastic components with respect to the amplitude of the momentum transfer vector, $q = |\mathbf{q}|$, are $S_{\mathrm{el}}(0) = N^2$, $S_{\mathrm{inel}}(\infty) = N$ and $S_{\mathrm{el}}(\infty) = S_{\mathrm{inel}}(0) = 0$, which is calculated from Eq. (4.20) and Eq. (4.30) where N is the number of electrons in the system. Several methods exist to calculate the total $S(\mathbf{q})$, elastic $S_{\mathrm{el}}(\mathbf{q})$ and inelastic cross-sections $S_{\mathrm{inel}}(\mathbf{q})$. Some of them use the analytical properties of the Gaussian type orbitals (GTOs) based wavefunctions [111, 258–260] and others draw upon the numerical Fourier transformation of the reduced one- and two-electron density matrices [261].

4.2.3. Real-time time dependent functional theory

Real-time first principles approaches [115, 116], including TDCI [262, 263], TD-CASSCF[66] and TDCC [69] etc., are natural for capturing non-perturbative electron motion by solving the Schrödinger equation in time. As an extension of DFT, RT-TDDFT

[264–267], which has been shown previously to give good agreement with methods such as ADC(2) [73], offers a good balance between efficiency and accuracy by propagating the non-interacting one-electron density (or N one-body functions), instead of the N-body wavefunction. In a Kohn-Sham (KS) framework this is given by,

$$\mathrm{i}\frac{\partial}{\partial t}\varphi_i(\mathbf{r},t) = \left\{-\frac{1}{2}\nabla^2 + v_{\mathrm{ext}}[\rho](\mathbf{r},t) + v_H(\mathbf{r},t) + v_{\mathrm{xc}}[\rho](\mathbf{r},t)\right\}\varphi_i(\mathbf{r},t), \tag{4.17}$$

where the electron-nuclear and electron-perturbation interactions are described by $v_{\mathrm{ext}}(\mathbf{r},t)$, $v_H(\mathbf{r},t)$ gives the mean-field electron-electron interaction and $v_{\mathrm{xc}}[\rho](\mathbf{r})$ is the exchange correlation potential potential, for which we use the adiabatic (local in time) approximation. Here the i^{th} KS orbital φ_i is described by a Slater determinant, and the one-particle density $\rho(\mathbf{r},t)$ is given by,

$$\rho(\mathbf{r},t) = \sum_{i}^{occ} |\varphi_i(\mathbf{r},t)|^2. \tag{4.18}$$

In principle, RT-TDDFT can account for the dynamics exactly but in practice the exchange correlation functions have to be approximated. Due to the adiabatic approximation typically made to the functionals, RT-TDDFT can be problematic for resonant excitation processes[101, 129], and the results may depend on the preparation of the initial state. Another error that arises from approximate functionals is the unphysical self-energy and the incorrect asymptotic potential. Besides turning to self-interaction correction (SIC) [268, 269], hybrid functionals (such as B3LYP, PBE0 etc.) can also reduce this error to some extent. Since delocalized valence density motion dominates the dynamics after the core-electron is ionized [73, 270, 271], hybrids are well-suited to study these processes.

RT-TDDFT with Gaussian basis sets is especially popular in theoretical chemistry and been applied to the study of strong field ionization [272, 273], whole energy range ex-

citations [274–277] and transient spectroscopy [278, 279] among others. Using a basis of n Gaussian functions as atomic orbitals (AOs) $\{\chi_\mu\}$, the molecular orbitals (MOs) can be written as the linear combination of AOs,

$$\varphi_i(\mathbf{r}, t) = \sum_{\mu}^{n} A_{\mu i}(t)\chi_\mu(\mathbf{r}), \tag{4.19}$$

and thus, $\rho(\mathbf{r}, t)$ can be computed as

$$\rho(\mathbf{r}, t) = \sum_{\mu\nu}^{n} \mathbf{P}_{\mu\nu}(t)\chi_\mu(\mathbf{r})\chi^*_\nu(\mathbf{r}), \tag{4.20}$$

with the density matrix $\mathbf{P}$ is calculated as the projection of density to the AOs,

$$\mathbf{P}_{\mu\nu}(t) = \sum_{i}^{n} \mathbf{A}_{\mu i}(t)\mathbf{A}^*_{\nu i}(t), \tag{4.21}$$

and the density matrix in the basis of molecular orbitals (Kohn-Sham eigenstates) $\mathbf{P}^{\mathrm{MO}}$ can be calculated by projecting density matrix in AOs with the coefficient matrix $\mathbf{A}$ (for simplicity here assumes no linear dependency occurs),

$$\mathbf{P}^{\mathrm{MO}} = \mathbf{A}^\dagger \mathbf{P} \mathbf{A}, \tag{4.22}$$

where $\mathbf{P}^{\mathrm{MO}}$ is a diagonal matrix in ground state.

With the prepared initial states, the density matrix can be propagated via von Neumann equation, which is typically done in the canonical basis (denoted with prime notation). In the basis of canonical orbitals, the density matrix propagated is given by,

$$\frac{\partial \mathbf{P}'(t)}{\partial t} = -\mathrm{i}[\mathbf{F}'(t), \mathbf{P}'(t)], \tag{4.23}$$

where the $\mathbf{P}'$ and $\mathbf{F}'$ are the density and Fock matrix in the CO basis. These are obtained by a projecting the density matrix in to the orthogonal basis set COs. The details of the

procedure of transforming between basis sets representations can be found in Ref. [280]. The time-dependent matrix can be calculated by integrating Eq. 4.23 over time with a second order Magnus propagator:

$$\mathbf{P}'(t+\Delta t) = e^{\Omega}\mathbf{P}'(t)e^{-\Omega}, \tag{4.24}$$

$$\Omega = -i\mathbf{F}'(t+\frac{\Delta t}{2})\Delta t. \tag{4.25}$$

The time-derivative of the density is most conveniently computed in the AO basis,

$$\frac{d\rho(\mathbf{r},t)}{dt} = \sum_{i}^{n}\sum_{\mu\nu}^{n}\frac{d\mathbf{P}_{\mu\nu}(t)}{dt}\chi_{\mu i}(\mathbf{r})\chi^{*}_{\nu i}(\mathbf{r}), \tag{4.26}$$

The reciprocal space representation, $\frac{d\rho(\mathbf{Q},t)}{dt}$, which is an important quantity for computing the X-ray scattering signals, can be calculated by a three-dimensional Fourier transformation of the time-derivative of the density matrix in the previous equation,

$$\frac{d\rho(\mathbf{Q},t)}{dt} = \int_{-\infty}^{\infty}\frac{d\rho(\mathbf{r},t)}{dt}e^{-2\pi \mathrm{i}\mathbf{Q}\cdot\mathbf{r}}d\mathbf{r}. \tag{4.27}$$

Besides directly looking into the density change in space, the electronic current density $\mathbf{j}(\mathbf{r},t)$ is a key quantity for interpreting the dynamics, since the scattering is related to its divergence Eqs. (4.10 and 4.11). It is defined as,

$$\mathbf{j}(\mathbf{r},t) = \sum_{i}^{n} -\frac{\mathrm{i}}{2}(\varphi_i^{*}\nabla\varphi_i - \varphi_i\nabla\varphi_i^{*}), \tag{4.28}$$

and can be calculated in the AO basis using the density matrix $\mathbf{P}(t)$:

$$\mathbf{j}(\mathbf{r},t) = -\frac{\mathrm{i}}{2}\sum_{\mu\nu}^{n}[\mathbf{P}(t)_{\nu\mu}\chi_{\mu}^{*}\nabla\chi_{\nu} - \mathbf{P}(t)_{\mu\nu}\chi_{\mu}\nabla\chi_{\nu}^{*}]. \tag{4.29}$$

The AO gradients Eq. (4.29) are typically available in any electronic structure code.

4.2.4. Calculation of scattering matrix elements from a core-hole

As the core-hole initial state considered here is non-stationary, $\mathbf{P}^{\mathrm{MO}}$ becomes non-diagonal and the transition amplitude between different states come into the off-diagonal elements. However, a diagonalized core-hole matrix $\mathbf{P}_{+}^{\mathrm{MO,\ diag}}$ can be obtained by projecting the non-stationary density $\mathbf{P}_{+}$ to the neutral ground state:

$$\mathbf{P}_{+}^{\mathrm{MO,\ diag}} = \mathbf{A}_0^{\dagger}\mathbf{P}_{+}\mathbf{A}_0. \tag{4.30}$$

In the context of a DFT/RT-DDFT derivation as the one presented in Sec. 4.2.3, molecular electronic wavefunctions can be constructed as a linear combination of Slater orbitals,

$$|\psi\rangle = \sum_{i=1}^{N_{\mathrm{conf}}} c_i \ |\phi_{\mathrm{SD}}^{i}\rangle \,, \tag{4.31}$$

where the c_i are the configuration interaction coefficients, N_{conf} is the number of configurations included in the expansion, and $|\phi_{\mathrm{SD}}^{i}\rangle$ are the Slater determinants. In the case of a single determinant method such as DFT, the wavefunction is built using a single Slater determinant and $c_1 = 1$. Each Slater determinant in Eq. (4.31) is constructed as a sum of spin-orbitals,$\varphi_j(\mathbf{r})$, where $\mathbf{r}$ are the electron coordinates. The expansion of the one-electron density matrix in Eq. (4.18) using these spin-orbitals can be then inserted in Eq. (4.15) to obtain the elastic structure factor S_{el},

$$S_{\mathrm{el}}(\mathbf{q}) = \left| \int \sum_{l,m}^{occ} \varphi_l(\mathbf{r})\varphi_m(\mathbf{r}) e^{\mathrm{i}\mathbf{q}\mathbf{r}} d\mathbf{r} \right|^2 . \tag{4.32}$$

For single-reference methods, the two-particle density matrix elements Γ_{klmn} can be constructed from the diagonal (stationary) one-particle density matrix elements P_{kl} (Eq. (4.30)) that are equal to the occupation number of the molecular orbitals,

$$\Gamma_{klmn}^{ij} = P_{mk}^{i} P_{ln}^{j} - P_{ml}^{i} P_{nk}^{j} \tag{4.33}$$

where i and j correspond to the two electronic states considered. The reduced two-electron density matrix then reads,

$$\Gamma^{(2)}_{ij}(\mathbf{r}_1, \mathbf{r}_2) = \sum_{klmn}^{N_{\text{orb}}} \Gamma^{ij}_{klmn} \varphi^i_k(\mathbf{r}_1) \varphi^i_l(\mathbf{r}_1) \varphi^j_m(\mathbf{r}_2) \varphi^j_n(\mathbf{r}_2), \tag{4.34}$$

where γ^{ij}_{klmn} are the two-electron reduced density matrix elements if $i = j$, and the two-electron reduced transition matrix elements when $i \neq j$ obtained through Eq. (4.33). N_{orb} is the number of occupied spin-orbitals $\varphi^i_l(\mathbf{r})$ forming every Slater determinant, $|\Phi^i_{\text{SD}}\rangle$. Combining Eq. (4.14) with the definition of the two-electron density matrix, the expression for the total X-ray scattering dynamic factor reads

$$\begin{aligned} S(\mathbf{q}) = \iint \sum_{klmn}^{N_{\text{orb}}} & \gamma^{ij}_{klmn} \\ & \phi^i_k(\mathbf{r}_1) \varphi^i_l(\mathbf{r}_1) \varphi^j_m(\mathbf{r}_2) \varphi^j_n(\mathbf{r}_2)\ e^{\mathrm{i}\mathbf{q}(\mathbf{r}_1 - \mathbf{r}_2)}\ d\mathbf{r}_1 d\mathbf{r}_2 \ \ + \ \ N, \end{aligned} \tag{4.35}$$

which leads to the resolution of two coupled integrals in $\mathbf{r}_1$ and $\mathbf{r}_2$. Eqs. (4.32 and 4.35) can be solved analytically, as demonstrated in [281] and [260].

4.3. Results

In this section attosecond electron dynamics following rapid core-hole ionization (Section 4.3.1) and UV-pumped excitation are demonstrated. As model systems we use oxazole and 4-aminophenol for hetero-aromatic ring molecules, as well as carbon monoxide for linear molecules. In the study of core-hole ionized oxazole and carbon monoxide, since the dynamics we study are faster than the life time of an oxygen K-edge core-hole (∼9 fs) [282], we do not take the Auger decay into account. All electronic structure calculations used the density functional theory (DFT) and RT-TDDFT module[264] in NWChem[283].

4.3.1. Oxygen K-edge core-hole induced attosecond ring currents in oxazole

In this section we show how X-ray scattering may be used to probe coherent attosecond electron dynamics triggered by the inner-shell ionization, which is shown in Fig. 4.1. This may be useful, for example for resolving the attosecond electronic density reorganization immediately before nuclear rearrangement in a photochemical reaction. Eluci-

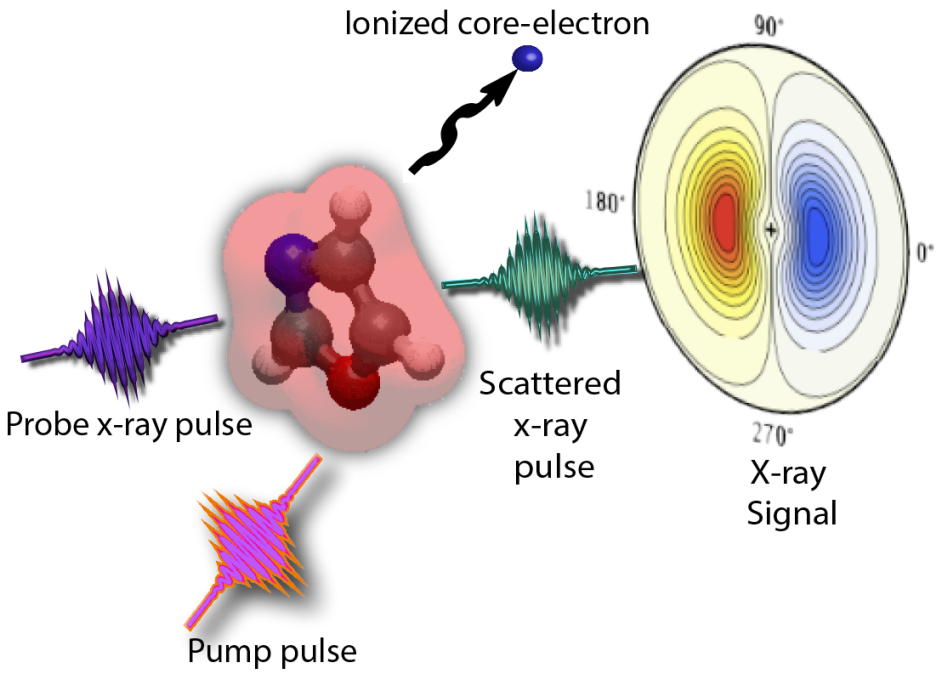

Figure 4.1. Schematic representation of the inner-shell ionization in oxazole and subsequent probing by an X-ray pulse.

dating this process is critical, as it is predicted to affect the ring-opening and fragmentation pathways, for example, by dictating which bonds break during the reaction. Due to the complexity of the scattering signals, simulations are necessary for interpretation of the resulting scattering patterns. Hermann *et al.*[113] recently demonstrated that the X-ray scattering in this case is primarily sensitive to the rate of change of the density, $\partial_t \rho(\mathbf{r}, t)$, rather than the instantaneous density itself. Drawing on a probability continuity argument

($\partial_t \rho(\mathbf{r}, t) = -\nabla \cdot \mathbf{j}(\mathbf{r}, t)$), attosecond X-ray scattering experiments can thus be viewed as probes of diverging electron currents rather than densities or holes. As an illustrative example, we study the dynamics induced by rapid core-hole ionization from the O K-edge in the oxazole molecule. We emulate this process by removing an electron from the O 1s orbital, followed by field-free propagation without energy minimization[73]. Removal of an K-edge electron from an atom-like orbital constitutes a reasonable representation of rapid ionization, unlike mixed-state valence cases which are typically multiconfigurational in character[73, 284]. The fast ionization creates a coherent superposition of states which results in density dynamics in the ring. Rapid ionization of this type has been observed to result in charge migration (CM), where a localized hole moves across the molecule [73, 284–288]. For the results presented here, the dynamics are perhaps best thought of as ring currents (continuous density flow) rather than CM. We focus primarily on the relationship between the time-evolving density/flux and the X-ray scattering, however, and do not characterize the dynamics as CM or non-CM. This excitation primarily results in in-plane dynamics along the x-direction (O/N axis), with a negligible evolution in the y and z directions. Following a sudden reorganization near $t \sim 0$, the time-dependent dipole moment along x-axis (O-N direction) oscillates with multiple frequencies due to the effectively broadband nature of the rapid core-hole ionization. The dominant mode has a period of roughly 0.5 fs. In order to determine how these dynamics can be measured using X-ray scattering, we selected five representative snapshots (red dots in Fig. 4.2) along a half-period. These points correspond to: maximum of the oscillation (a, $t = 0.08$ fs), three intermediate times (b, 0.15 fs; c, 0.21 fs; d, 0.29 fs), and the minimum (e, 0.33 fs). For each of these, the current density $\mathbf{j}(\mathbf{r}, t)$ and the time-derivative of the electron den-

sity (in real-space) were computed from the density matrix. Note that the dipole moment and average currents are related to each other but oscillate out-of-phase, *i.e.* the maximum/minimum dipole (points a, e) correspond to times with low average currents, whereas the intermediate times (b,c,d) have significant net currents across the molecule. The absolute value of the momentum-space density derivatives $\left|\frac{d\rho(\mathbf{Q},t)}{dt}\right|$ was then computed via the absolute value of the 3D FFTs of the real-space $\frac{d\rho(\mathbf{r},t)}{dt}$. These two quantities, re-

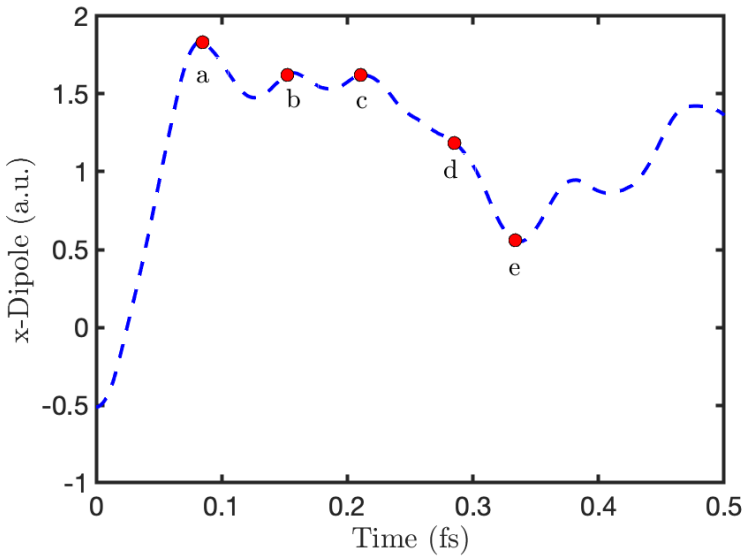

Figure 4.2. Computed time-dependent dipole moment of oxazole along X-axis (O-N bond) following an O K-edge core-hole ionization. The five time points chosen for scattering calculations are marked with red circles.

lated through the continuity equation in real-space (Eq. (4.11)), give complimentary information: $\mathbf{j}(\mathbf{r},t)$ shows the mechanism of electron flow during the process, and $\left|\frac{d\rho(\mathbf{Q},t)}{dt}\right|$ is related to the time-dependent X-ray scattering. Finally, to match the conventional experimental conditions we have also included a rotational-averaged representation of the absolute density derivative $\left\langle\left|\frac{d\rho(Q,t)}{dt}\right|\right\rangle_{\Omega}$, that accounts for all possible molecular orientations in a random gas-phase ensemble of molecules.

Fig. 4.3 shows four quantities for the five time snapshots. The top row shows the magnitude of the current densities $\sqrt{\mathbf{j}(\mathbf{r},t)\cdot\mathbf{j}(\mathbf{r},t))}$ 1 Å above the molecular plane. This was chosen to better visualize the currents in the π-conjugated system and avoid showing the strong localized currents flowing to/from each atom, which would appear at Q values beyond the detection limit of current X-ray sources[289]. In this case, the electron density flows across the molecular backbone, resulting in semi-ring currents (discussed below). The second row shows the corresponding current vector lines in this plane. The third row in this figure shows $|\frac{d\rho(Q,t)}{dt}|$ for the $Qz = 0$ Å^{-1} slice of the reciprocal space. This emulates a scattering experiment in which the incident X-ray beam travels in a perpendicular direction with respect to the molecular plane. The momentum-space Qx and Qy values range between -15 Å^{-1} and 15 Å^{-1} using a 100×100 Q-grid. The localized currents give rise to high Q signals. Due to the direct relationship between $\frac{d\rho(Q,t)}{dt}$ and scattering, these plots are qualitative predictions of the expected X-ray signals at every time point for fixed molecular orientation and rotationally averaged measurements, respectively. As expected, the lack of symmetry in the oxazole molecule results in static patterns that only maintain the centrosymmetry [290]. Finally, the fourth row shows the rotationally averaged signal using a 200^2 Q-grid, obtained by integration over the azimuthal and polar angles [291]. The inclusion of rotational averaged values corresponds to a measurement of an ensemble of randomly oriented molecules.

We now discuss the ring-current mechanism in detail and how these currents qualitatively manifest in the scattering patterns. At time 0.08 fs (point a), when the dipole moment reaches its first maximum, there are three distinct current flows: a divergence from the oxygen, and two weak semi-ring counter-currents traveling from the right of the

ring towards the oxygen. The diverging currents from the oxygen are localized in space and result in a broad, high Q (starting at $Q = 14$ Å^{-1}) signal that is not fully contained in our reciprocal space representation. These currents are likely related to the rapid response of valence electrons to the core hole created at $t = 0$. The semi-ring currents appear at $Q = 3.1$ Å^{-1} in momentum space, which is a reflection of the curved electron flow spanning the entire ring. At the second snapshot time (point b, 0.15 fs), the dynamics becomes dominated by two strong right→left semi-ring currents with significant curvature ($C_3 \rightarrow C_2 \rightarrow H$; $N \rightarrow C_1 \rightarrow H$). As the two currents have different curvature and magnitude, this results in two main signals in the scattering at $Q = 2.0$ Å^{-1} and $Q = 4.5$ Å^{-1}. The broad signal centered at 15 Å^{-1} remains, but has a lower magnitude. This arises from weak but non-zero converging currents near the oxygen.

At point c (0.21 fs), the currents flow mostly perpendicularly to the direction of the density oscillation (towards C_2=C_3 and C_1) with relatively localized linear flows. Since the main two currents have similar magnitudes and curvature, this results in a single broad scattering peak at Q =4.2 Å^{-1}. At the next snapshot (point d; 0.29 fs), the dipole moment in the O-N direction is roughly near the average value and thus expected to have a large current. The current density in Fig. 4.3 shows a strong left-to-right ring current split into two channels, one from $C_1 \rightarrow C_3$ and another from $C_2 \rightarrow N$. These intersecting currents manifest in the scattering as two distinct peaks at $Q = 3.6$ Å^{-1} and 6.3 Å^{-1}. Since the current flows with different curvature (more linear/along the bonds) than in the the right-to-left (point b) case, the scattering signals occur at different Q values. As before, the absence of core-hole currents results in no clear peak within the Q range considered. Finally, at 0.33 fs (point e), when the dipole becomes minimum, there are four distinct

currents: two converging on O, one diverging from C_1 and one diverging from C_2. The two ring currents result in a set of low Q peaks at 2.1 Å^{-1} and 4.2 Å^{-1}, which is roughly consistent with the positions of the previous ones. Since two of these currents converge sharply on the oxygen core-hole, this results in a strong, broad high Q signal (17.0 Å^{-1}).

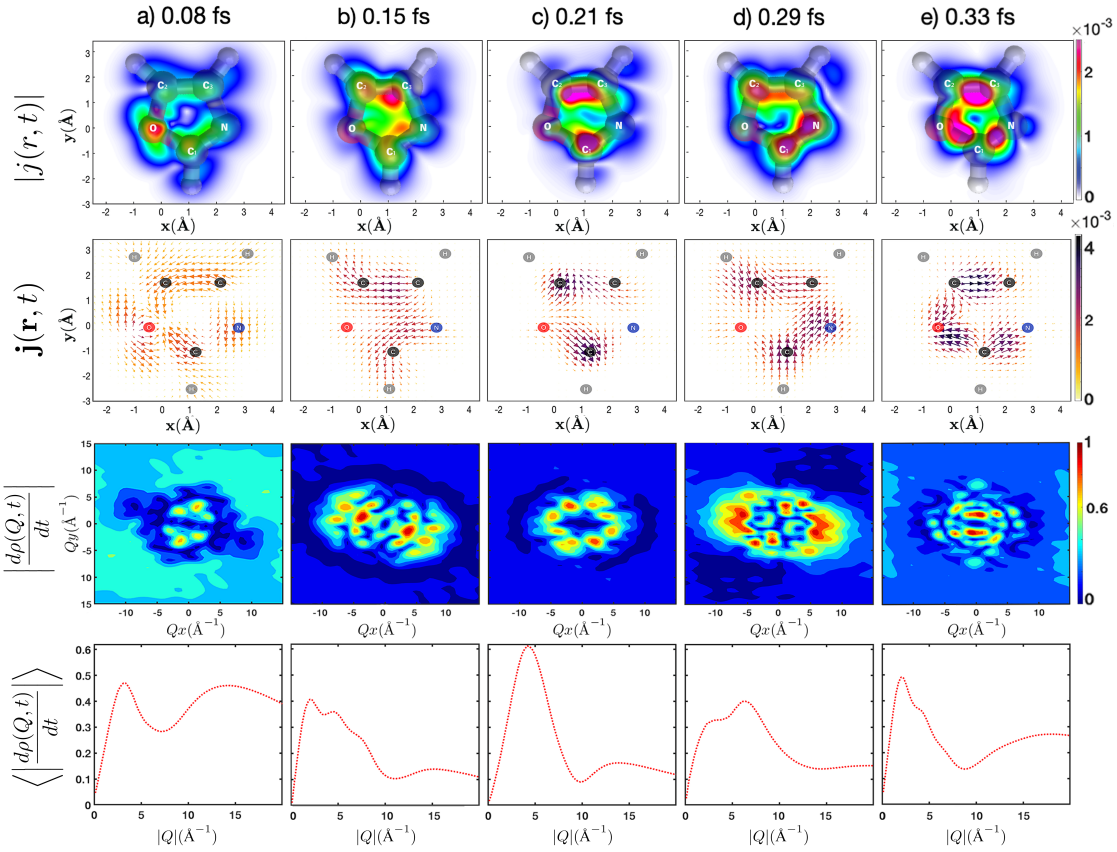

Figure 4.3. Simulated electron current magnitude $|j(\mathbf{r},t)|$ (top row), electron current vector fields $|\mathbf{j}(\mathbf{r},t)|$ (second row), absolute value of the Fourier transformed electron density time-derivative $\left|\frac{d\rho(Q,t)}{dt}\right|$ (third row) and rotational-averaged $\left\langle\left|\frac{d\rho(Q,t)}{dt}\right|\right\rangle_\Omega$ (bottom row) for five different time delays (columns): 0.08, 0.15, 0.21, 0.29 and 0.33 fs extracted from the dynamics simulation of the O K-edge ionization in oxazole. All the values represented are in a.u. except the distances and momentum vectors which are presented in Å and Å^{-1} respectively

Looking at the results as a whole, there is a clear correlation between the scattering patterns and the currents within the molecule. Broadly speaking, ring currents are mir-

rored as complex, low Q features, whereas electron flows into/out of a single atom result in a broad, high Q peak. These results also demonstrate that, although the instantaneous density is an important quantity for probing nuclear dynamics, for electron dynamics it is the divergence of the currents (or alternatively the derivative of the density) that dominates the signals.

4.3.2. UV-pump initiated attosecond ring currents in aminophenol

We simulated the electron motions induced by a UV-pump in 4-aminophenol to further analyze the X-ray scattering of ring currents. These dynamics have been previously examined by XTAS simulations, which reveal the electron density motion around the N and O atoms through modulations of their corresponding K-edge absorption [92]. However, the proximity in energy of the ring-carbons prevents XTAS from resolving dynamics across the ring. X-ray scattering, on the other hand, can probe electron flows in real-space, serving as a suitable tool for providing an all-element description of the dynamics. As in the previous chapter, the initial state is prepared using cdft to distribute 0.3 charges on the $-$OH site and 0.3 electrons on the $-NH_2$ group to emulate the UV-pump excitation. The def2-tzvp basis set and PBE0 functional are employed for this simulation. To remove high-frequency noise caused by non-equilibrium initial states, a Butterworth low-pass filter with a 6 eV cutoff energy is applied to the density matrix, which ensures all physical quantities are appropriately filtered.

Fig. 4.4 depicts the modulations between the temporal evolution of the simulated scattering signal ($\left\langle \left| \frac{d\rho(Q,t)}{dt} \right| \right\rangle_\Omega$) and the corresponding time-dependent dipole moment of the "UV-pumped" aminophenol along the x-axis (where O and N are located). After

the excitation of the "UV pump", the electrons move from the $-NH_2$ group to the $-OH$ side with a main frequency of 5.7 eV and a low frequency of 2.1 eV. It can be seen that the scattering intensity is related to the amplitude of the dipole moment. At the max-

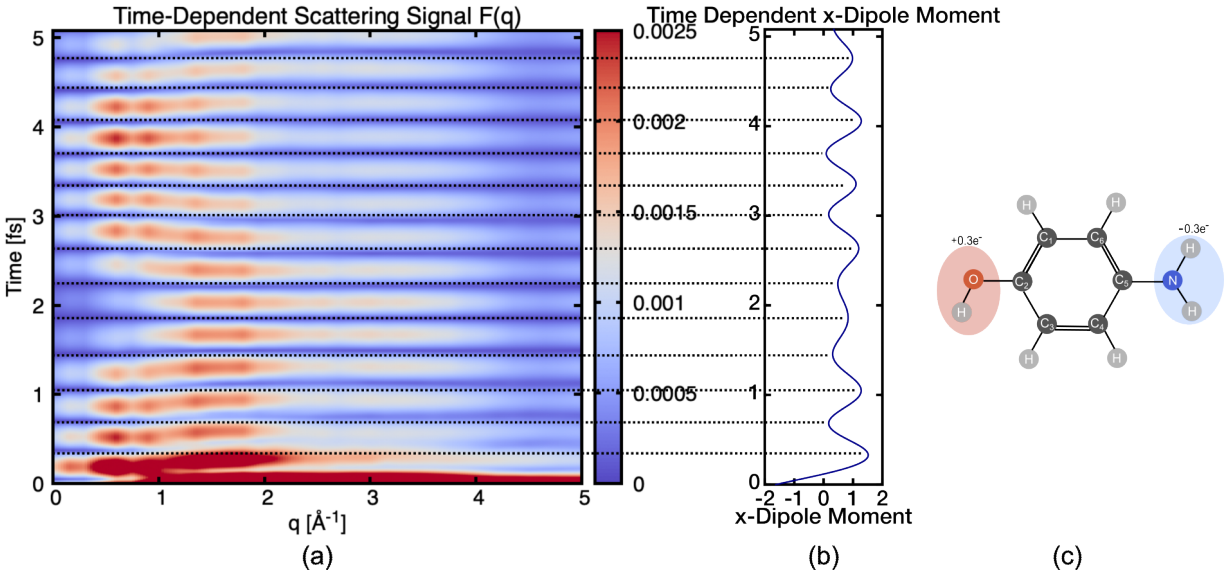

Figure 4.4. This figure shows: (a) the simulated real-time scattering signals of 4-aminophenol; (b) the calculated time-dependent dipole moment along the x-axis (N-O direction); and (c) an illustration of the preparation of the "UV-pumped" initial states.

ima/minima of the dipole moment, when the electron density oscillates to the end of the molecule with minimal momentum, the scattering signals reduce to their minimum values. Additionally, noticeable shifts from the lower-Q range (0.5 to 1 $Å^{-1}$) to the higher-Q range (1.2 to 2 $Å^{-1}$) emerge at each half period of the density oscillation. This effect is more prominent between 1.5 and 2.2 fs and can be attributed to the low-frequency dynamics.

To examine the relationship between the characteristic dynamical features and the scattering peak positions, we selected five time-steps from a modulation as the electrons travel from the nitrogen side to the oxygen region. Fig. 4.5 shows a zoomed-in view

of the time-resolved scattering and the corresponding dipole moment between 0.65 and 1.05 fs, highlighting the selected points of interest with red circles: A (0.73 fs), B (0.8 fs), C (0.87 fs), D (0.94 fs) and E (1.03 fs). Fig. 4.6 illustrates their corresponding electron

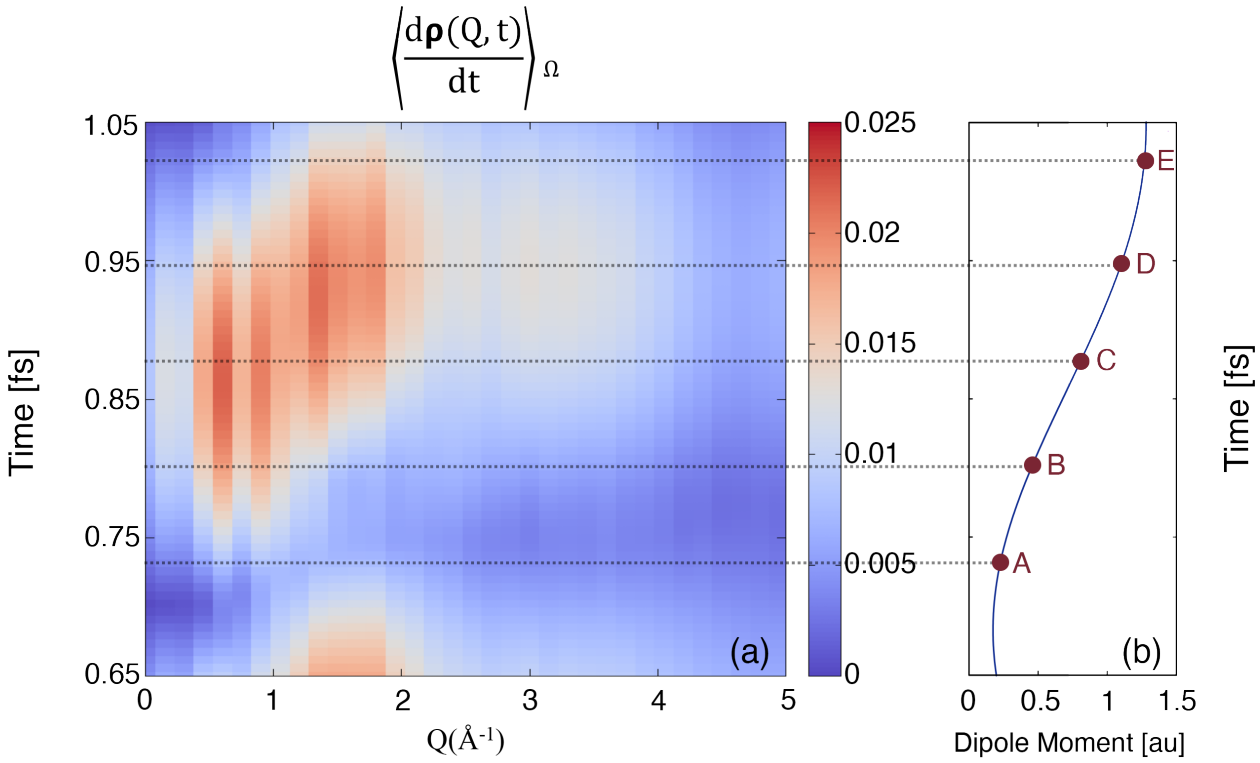

Figure 4.5. The zoomed-in of Fig. 4.4 between 0.65 to 1.1 fs. Five time-points are chosen for the scrutiny of the electron currents and the time-dependent signals. The main peak gradually blue-shifts from 0.8 Å^{-1} to 1.6 Å^{-1}

currents. To exclude the core-currents from the sudden charge separation at t=0, the vectorfields of the currents are projected along the z-direction, which is perpendicular to the molecular plane, with the exclusion of the range of z=0∼0.2 Å^{-1}. At time A, which is around the maximum dipole amplitude, the net electron currents are negligible, resulting in a low-intensity scattering signal. At time B, the electron density migrates from the $-NH_2$ side to the $-OH$ functional group via homogeneous flows across the backbone of the ring, which diverge from C_5 and converge to C_2, resulting in a low-Q scattering peak

between 0.5 and 1 $Å^{-1}$. At time C, while the long-range ring currents are intensified as the dipole displacement approaches its minimal magnitude, the currents from the $-NH_2$ functional group start to diverge to its two adjacent C−H bonds, resulting in the emergence of the scattering in the higher-Q range of 1.3∼1.8 $Å^{-1}$. With the dipole amplitude increasing from time C to time D, part of the electron density begins to flow towards the O→N direction, opposite to the right-left electron motion in previous steps, as shown in the current plot of time D. These counter-currents bridging the left (C_1−C_6) and right (C_3−C_5) sides of the ring further attenuate the long-range global ring currents and form three localized flows: C_1, C_3→ O, C_1, NH_2→ C_6 and C_3, NH_2 → C_4. These collective effects result in a significant reduction of the lower-Q signal concomitant with an enhancement of the higher-Q signal. At time E, the currents that reside in the left and right of the ring become weaker while these O→N semi-ring currents increase, breaking the N→O nonlocal ring currents. Consequently, the scattering peak in the low-Q region significantly reduces and leaves only the higher-Q peak. Since these short-range dynamics are evenly distributed, they will produce minimal net currents and are consistent with the maximum of the dipole amplitude. The results in the study of the UV-pumped 4-aminophenol further validate the qualitative mapping between the scattering signal and the divergence of the electron currents as revealed in 4.3.1. The low-Q peaks can be attributed to the long-range ring currents, while the higher-Q peaks are characteristic signals of the short-range dynamics with divergent flows. We can also infer that in the UV-pumped aminophenol, the high-frequency dynamics are associated with the electron oscillation between two ends of this molecule with diverging currents when the density changes directions, while the low-frequency dynamics, which occur from 1.4 to 2.2 fs, are dominated by diverging cur-

rents that balance the electron distribution across the molecule, causing the scattering signals to significantly shift to the higher-Q region.

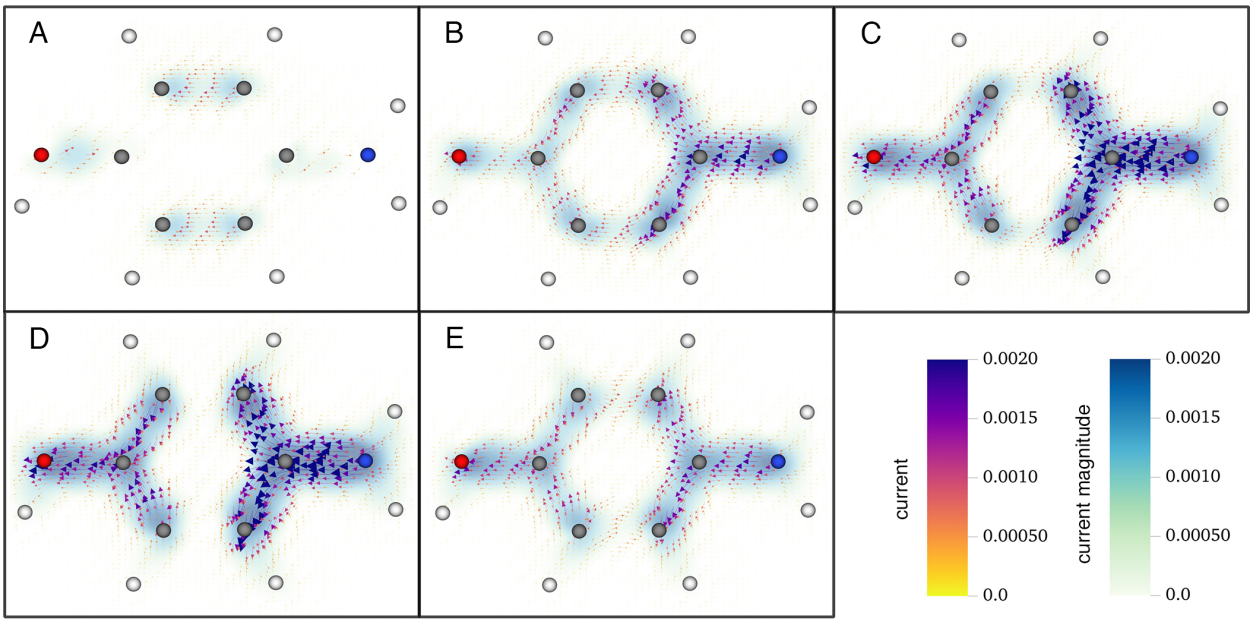

Figure 4.6. Electron currents at the chosen time steps in Fig. 4.5. The vector fields of the currents are scaled $\times 250$ for the visualization of the current fields. The magnitudes of the electron currents are plotted with pseudocolor.

4.3.3. Oxygen K-edge core-hole triggered attosecond currents in carbon monoxide

Linear molecules may seem less interesting at first glance due to the lack of complex geometries that support curved currents. However, in molecules with heteroatoms, the molecular orbitals are not symmetric in space and can raise electron flows with unequal curvatures around each atom. These asymmetries make it possible to reveal the electron dynamics of linear molecules in the scattering signal. To investigate the relation-

ship between electron currents and scattering signals in linear molecules, we chose carbon monoxide as the model system for its π-conjugated electronic structure and geometrical simplicity. In this section, we scrutinize the dynamics induced by the oxygen K-edge core-

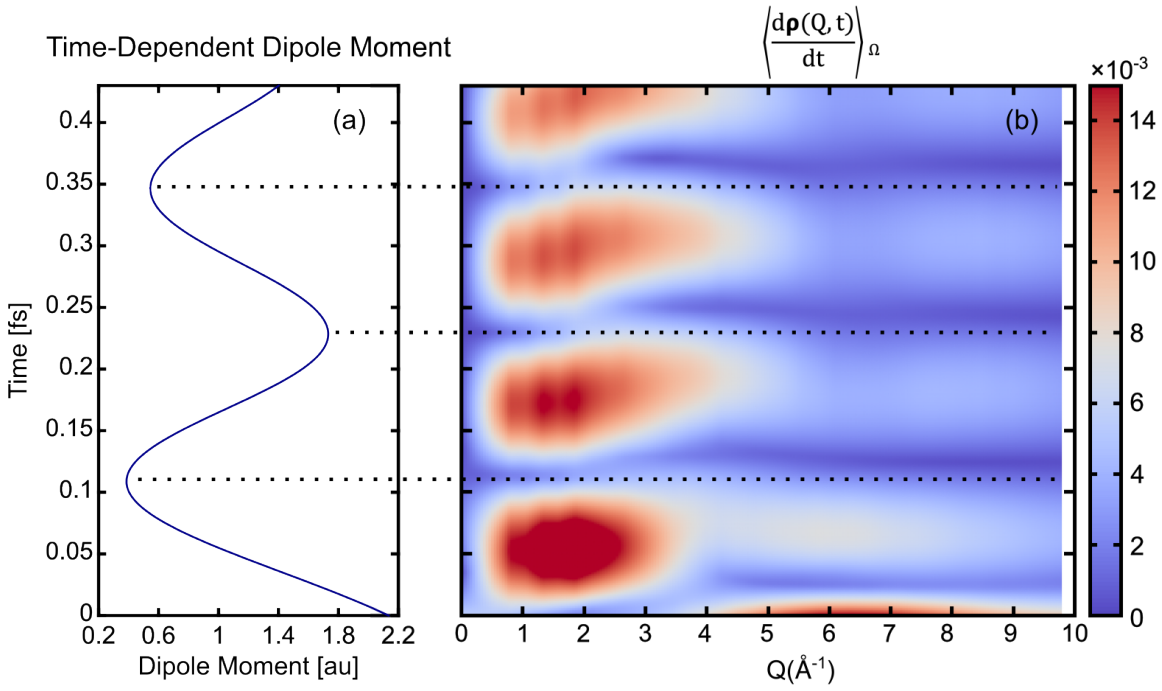

Figure 4.7. Simulated time-dependent dipole moment along the C-O bond (a) and scattering signals (b) for the dynamics of carbon monoxide after the removal of the oxygen K-edge electron. The dipole magnitude and the scattering pattern are correlated with out-of-phase modulations.

hole in CO, which are prepared by the removal of the oxygen 1s electron from the ground state CO without the SCF convergence procedure. PBE0 exchange correlation functional and def2-tzvp basis sets are used in the simulation. A 20 eV Butterworth low-pass-filter is applied to eliminate the unwanted high-frequency modes generated by the sudden creation of the core-hole at t=0 fs. After the ionization of the oxygen 1s electron, the electrons oscillate between C and O with a frequency of 17 eV.

Fig. 4.7 shows the simulated dipole moment and scattering signal of the electron

motion after the removal of the oxygen K-edge electron. As in previous studies in ring-shape molecules, the magnitude of the dipole displacement is correlated with the scattering amplitude with out-of-phase modulations. However, noticeable peak shift from the lower-Q region (1∼2 $Å^{-1}$) to the higher-Q region (2∼6 $Å^{-1}$) with broadened width is observed at each half-period, with a delay of roughly 0.025 fs in the depletion of the scattering signal at the higher-Q region compared with that at the lower-Q range. Here we analyze the electron dynamics as they move from the carbon to the oxygen atom along the half dipole oscillation period in detail. Specifically, we selected five time points at 0.23 fs, 0.26 fs, 0.29 fs, 0.32 fs and 0.35 fs. The first row of Fig. 4.8 displays the dipole

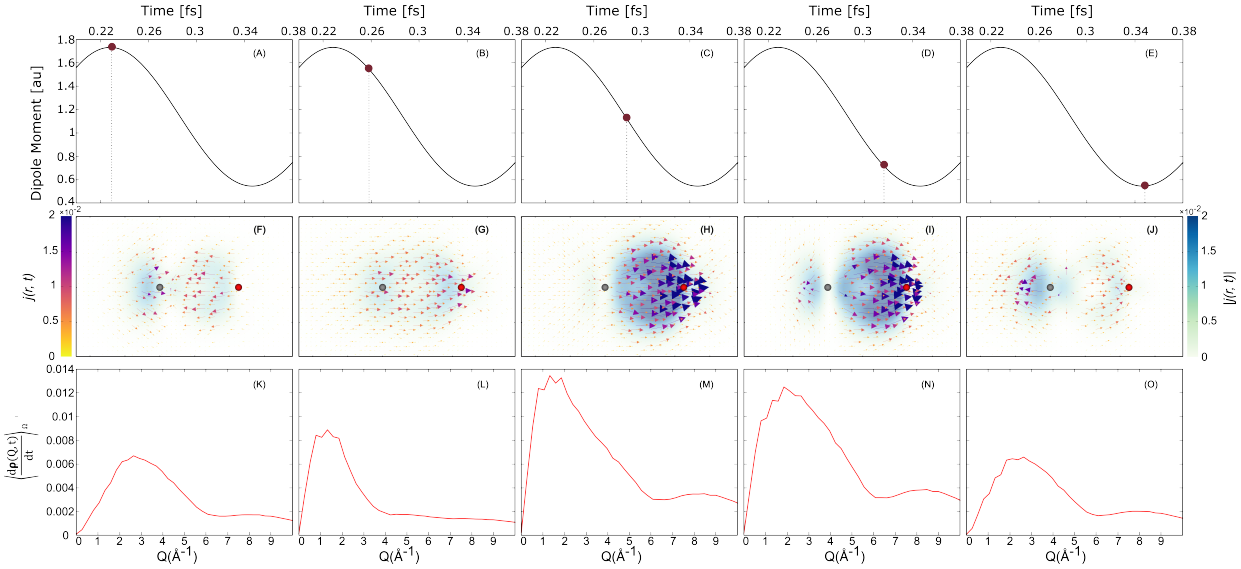

Figure 4.8. In the first row, panels (A)-(E) display the position of the selected time steps in the time-dependent dipole moment. The second row (F)-(J) demonstrates the vector field of the electron current and its amplitude in pseudocolor for each corresponding time step. The third row (K)-(O) exhibits the resulting scattering pattern for each chosen time step.

moment position for the selected time steps. In the second row, we present time-resolved current data using vector field plots for direction and pseudocolor plots for amplitude. The electron currents are selected from 0.3 Å to 3 Å above the molecular plane (xy-plane)

and projected along the z-direction. The pseudocolor plots are sliced at 0.3 Å above the molecule at the z-axis to avoid the strong core-electron currents for better visualization. Finally, the third row of Fig. 4.8 presents the resulting scattering signals for each selected time point. One thing that needs to be mentioned is that the sawtooth shapes in the first scattering peak do not represent physical peaks, but rather result from the limited resolution of the radius grid. At t=0.23 fs, two weak, opposite flows on the left and right sides of the molecule render a minimum net current, which matches the maximum dipole displacement. Due to their similar curvature and length, these two counter-currents manifest as a broad peak around 3 $Å^{-1}$. At t=0.26 fs, when the dipole displacement reaches its midpoint, the electrons flowing from left to right of the molecule create a set of global, homogeneous currents, leading to a low-Q peak around 1.5 $Å^{-1}$. These long-range currents are approximately twice the range of the counter-flows observed at 0.23 fs, accounting for the shift of the scattering peak to half of the peak position in the previous time-step. At t=0.29 fs, the strong net electron flow is consistent with the minimal dipole magnitude. The intensified global flow leads to an increase in the scattering signal of the low-Q signal. Due to the more pronounced curvature of the long-range flow, the scattering peak broadened to a width of 6 $Å^{-1}$. The flat peak observed around 8 $Å^{-1}$ may be attributed to the localized flows around the carbon and oxygen atoms. At t=0.32 fs, as the dipole reaches another middle point in the oscillation with opposite direction to that at t=0.26 fs, the one-direction flows that are parallel to C−O bond decrease, accompanied by part of the electron currents moving towards the carbon side. These can account for the reduced signal intensity and shifted peak at 2 $Å^{-1}$ in the scattering plot. At the last time step (0.35 fs), the dipole returns to its maximum amplitude in the opposite direc-

tion, which is reflected by an approximately zero net current from the two counter-flows. These two counter-flows yield an almost identical scattering pattern as in the first step, which will disappear when the global molecular currents in the next oscillation build up again. These results show that the coherent unidirectional flow along the molecule backbone can be attributed to the low-Q peak, whereas the counter-flows, which divide the homogeneous dynamics in half, lead to the peak shifting to the higher-Q range. During the transition between these two types of dynamics, the scattering pattern exhibits a broad signal between these two peaks. These findings are in agreement with previous studies on ring-shaped molecules, indicating that even simple linear molecules that consist of heteroatoms such as CO can sustain currents with considerable divergence, allowing them to be detected using time-resolved X-ray scattering techniques.

4.3.4. UV-pump excited attosecond currents carbon monoxide

In this section, we further investigate how the time-evolving electron transitions are encoded in the scattering signal in linear molecules by examining the electron dynamics in carbon monoxide induced by a "UV-pump". This system was also previously studied with simulated XTAS [92]. The preparation of the initial state follows the same procedure as in the aforementioned XTAS study. To imitate the UV-pump excitation, 0.8 electrons are assigned to C and 0.8 charges to O, which approximately picturizes the electron distribution after a π to π^* excitation, with cdft and PBE0 functional. The generated dynamics are also processed with a 20 eV Butterworth low-pass-filter to remove the high-frequency response from the rapid charge separation in the initial state.

As illustrated in Fig. 4.9, the simulated dipole moment and time-resolved X-ray

scattering signal exhibit a clear modulation with out-of-phase correlation, as the electron density travels between the carbon and oxygen atoms at a frequency of 14.2 eV. Com-

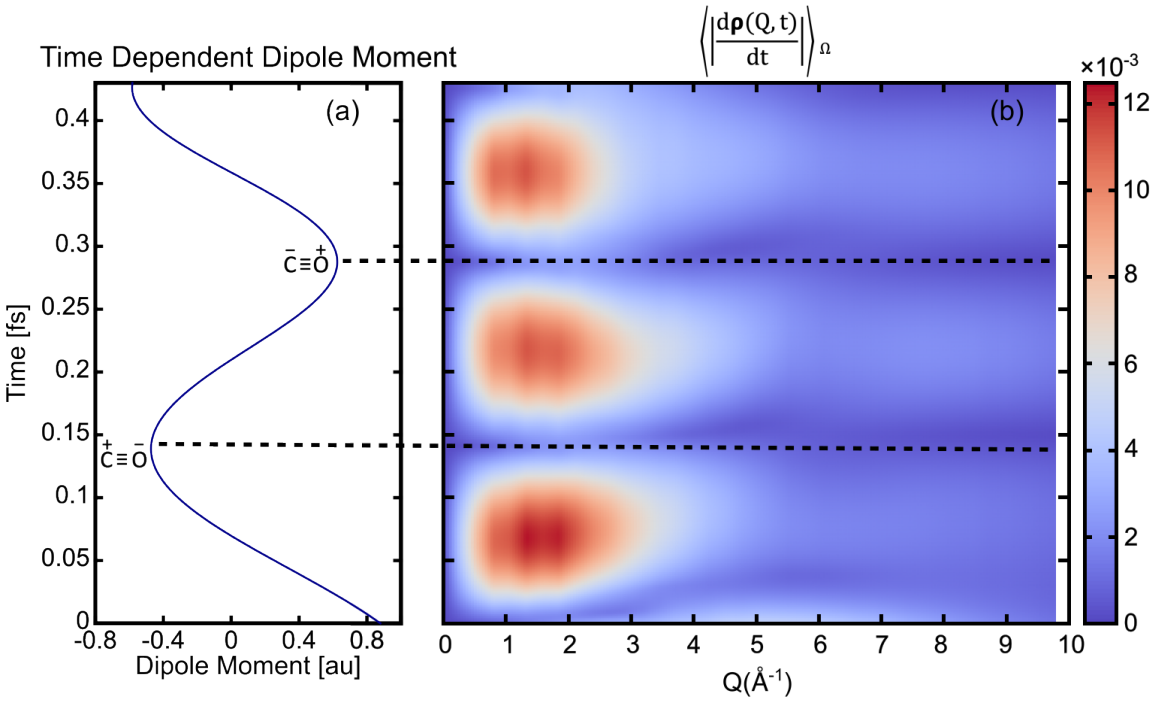

Figure 4.9. The simulated dipole moment is shown in panel (a), and panel (b) displays the time-resolved X-ray scattering signal for CO. It is evident that there is a significant modulation between these two quantities.

pared to previous studies on both ring-shaped molecules and carbon monoxide with an oxygen K-edge core-hole, this "UV-pumped" valence excitation in carbon monoxide exhibits no significant peak shift during each modulated period. Five time steps within half of a dipole oscillation period, during which the electrons flow from C to O, are chosen to be examined in depth. The selected time steps and their corresponding dipole moments are shown in the first row of Fig. 4.10, with each column representing time points of 0.29 fs, 0.33 fs, 0.36 fs, 0.4 fs, and 0.42 fs, respectively. The second row of Fig. 4.10 shows the simulated electron currents for the selected snapshots. The electron currents are chosen from a range of 0.15 to 3 Å above the molecular plane, which the currents are sub-

sequently projected onto. The pseudocolor plots for the magnitude of the electron currents are sliced at 0.25 Å above the molecular plane for clarity.

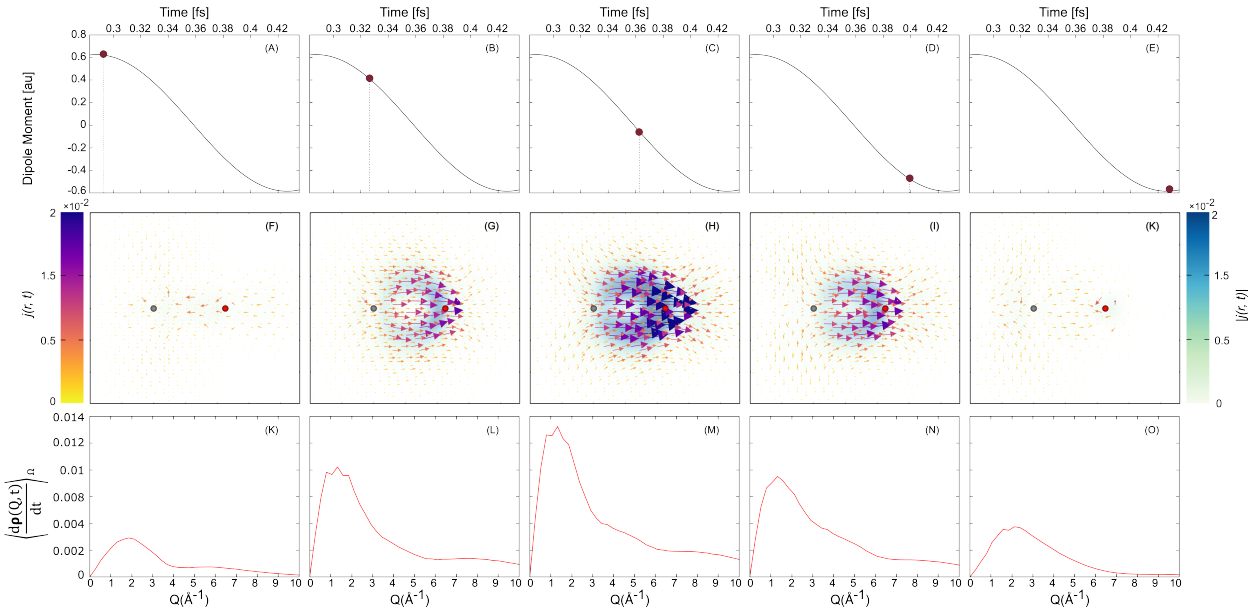

Figure 4.10. The first row (panels A-E) displays the dipole moments of the selected time-steps, denoted with red circles. (F)-(J) in the second row illustrate the vector field of the electron currents for each selected time-step, along with their corresponding intensity represented by a pseudocolor scheme. The third row (panels K-O) presents the corresponding scattering signals in momentum space.

At time point A, when the dipole undergoes maximum oscillation, a set of weak currents of varying shapes arise around each atom and in the inter-molecular space between the C-O bond, producing an approximate net current of zero and a scattering signal around 2 Å^{-1} with a low and broad profile. At time point B, the advent of the strong long-range currents from C to O leads to a strong peak at approximately 1.5 Å^{-1}. Since the electron flows exhibit notable curvature around the carbon and oxygen atoms, the peak width broadens up to 5 Å^{-1}. From time B to time C, with the decrease in dipole amplitude, the electron flows intensify along the molecule scaffold, leading to an increase in the magnitude of the broad scattering signal at 1.5 Å^{-1}. At time point D, the dipole

magnitude increases again as the homogeneous electron currents weaken, resulting in a reduction of the scattering signal that is similar to that observed at time B. At time E, as the electron density arrives at the O end, the net current becomes trivial again, thereby the scattering signal is reduced to its minima. Due to the larger curvature of the currents at time E compared to those observed at time A, the peak width at time E become broader. To sum up, our studies on the dynamics of oxygen K-edge ionization and "UV-pumped" excitation of carbon monoxide demonstrate that time-resolved X-ray scattering signals can capture the characteristics of electron flows in linear molecules. When the electrons traverse the linear molecule, the main scattering peak appears at low-Q region. However, as the homogeneous flows become more curved around the end atoms, this low-Q peak expands to a higher-Q region, as observed in both core-hole ionization and UV-excitation cases. Moreover, the scattering patterns of the carbon monoxide with oxygen K-edge core-hole show that when removing the core electron from molecules, the dominant electron currents can transfer from one-directional to opposite-directional flows as the electron-hole rearranges, resulting in peak shift from low-Q to high-Q.

4.4. Conclusions

In conclusion, we have presented simulations of time-resolved scattering from systems with evolving electron density. We have shown that, at least qualitatively, X-ray scattering can be used to map out the time-dependent electron currents in excited molecules. In this chapter we did not use the analytical scattering expression, and instead related the scattering to the dynamics via the absolute value of the electron density derivative. It is important to note that this gives only a qualitative picture of the map-

ping between scattering and instantaneous currents. To properly compute this mapping would require either time-dependent two-particle reduced density matrices or explicit calculation of a large number of states in the molecule. Nevertheless, our results capture the essential relationship between electron current and scattering. Here, the instantaneous density is not the quantity that determines the scattering, but instead it is sensitive to the divergence of the electronic currents, as demonstrated by the authors in Ref. [113]. As a result, scattering is well-matched to cases where these currents have appreciable curvature, such as in ring-shaped molecules and linear-molecules with localized core-hole. Rings with heteroatoms are especially promising candidates since the currents can be influenced by the differing electronegativites at the different sites on the ring. For the specific case of oxygen core-hole ionization in oxazole, we show that the resulting currents that span the ring appear at Q values between 2 and 6 Å^{-1}, whereas localized currents around into/away from the oxygen atom appear at Q $\sim$12 Å^{-1}. In the study of UV-pumped 4-aminophenol, the homogeneous global ring-shape currents occur between Q $\sim$ 0.5 to 1 Å^{-1}. When the localized diverging flows along the ring become dominant, the scattering signal shifts to the range of 1.3 to 1.8Å^{-1}. In our investigation of the linear molecule, carbon monoxide, we found that the dynamics triggered by the oxygen K-edge core-hole exhibit more complexity than those induced by the UV-pump. In both cases, the peak near 1.5Å^{-1} can be attributed to the current along the molecular backbone. For the UV-pumped dynamics in carbon monoxide, since there are no strong perturbations involved, the currents are dominated by linear motions, whose intensity change can be monitored by the scattering amplitude. However, for the carbon monoxide with an oxygen K-edge core-hole, the rearrangement of the core-hole can produce localized counter-flows, leading

to the peak shift to the higher-Q region. These studies suggest that both ring and linear currents will be able to be measured by time-resolved X-ray scattering experiments once sufficient time resolution is achieved, opening the door to measuring the dynamics immediately before the arrangement of atoms, where electron currents may play an important role in softening the bonds.

Appendix A. Intruder Peak-Free Transient Inner-Shell Spectra using Real-Time Simulations Supplementary Details

A.1. Origins of the Intruder Peaks in 4-Aminophenol

In this section we discuss the origins of the unphysical intruder peaks in O K-edge and N K-edge absorption in aminophenol. Fig. A.1(a) shows the O K-edge XANES both with and without a filter, and Fig. A.1(b) shows the spectrum resulting from only contributions from the N K-edge . This demonstrates that the intruder peaks arise from unphysical transitions from N 1s→high virtual states. Fig. A.1(c,d) show a similar analysis for the N K-edge XANES spectrum. To generate the figures above, all real-time dipoles are damped with $\tau = 25$ a.u.

A.2. Basis Set Effects in 4-Aminophenol

Fig. A.2 presents unpumped N K-edge absorption of aminophenol for three different basis sets: (a) def2-SVP, (b) def2-TZVP, (c) def2-TZVPD for unfiltered RT (solid line), filtered RT (dashed line), and LR (filled green). For the small (def2-SVP) basis set there are no intruder peaks, which is a consequence of lack of high angular momentum basis functions. In addition to the expected dependence of the spectrum on basis, especially for high energies, both of the larger basis sets (def2-TZVP and def2-TZVPD) have a large number of intruder peaks, which vary significantly between the two basis sets. These results are representative of our general observations: intruders in inner-shell spectra are highly basis set dependent, but using a filtered dipole consistently removes them.

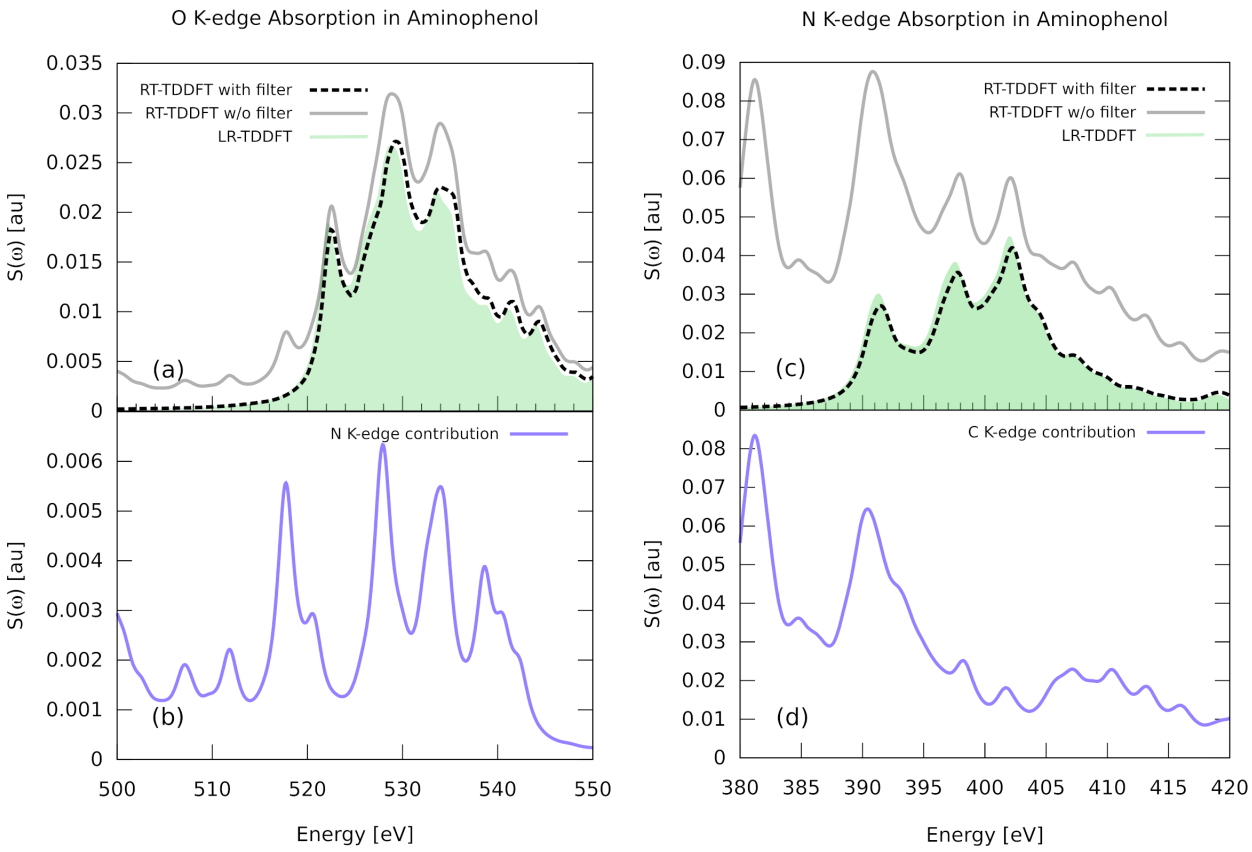

Figure A.1. (a) Filtered, unfiltered, and linear response O K-edge spectra for 4-aminophenol. (b) The N 1s contributions to the O K-edge give rise to the intruder peaks. (c,d) Similar analysis for the N K-edge shows that the intruder peaks come from transitions from the C 1s orbitals.

A.3. Transient Spectra of 4-Aminophenol over A Wider Energy Range

Fig. A.3 and Fig. A.4 show the XTAS of 4-aminophenol in the O K-edge and N K-edge absorption regions, respectively, spanning an energy range larger than that presented in the main manuscript. In Fig. A.3, the unfiltered simulations not only result in intruder peaks in the pre-edge and high energy region, they also add extra weights on the physical absorption. As shown in Fig. A.4, besides the unphysical weights in the high energy region, the unfiltered TAS have significant intruders in the pre-edge and rising edge region.

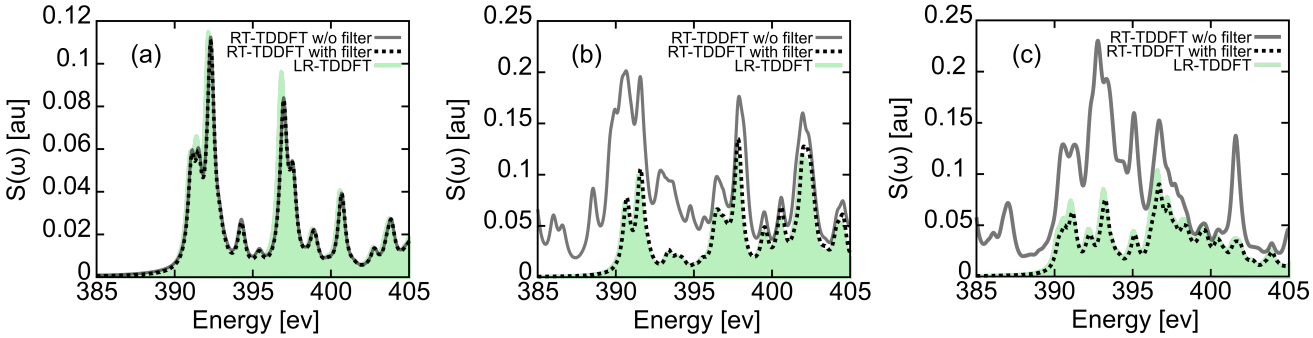

Figure A.2. Filtered, unfiltered, and linear response N K-edge spectra for 4-aminophenol using different basis sets: (a) def2-SVP; (b) def2-TZVP; (c) def2-TZVPD

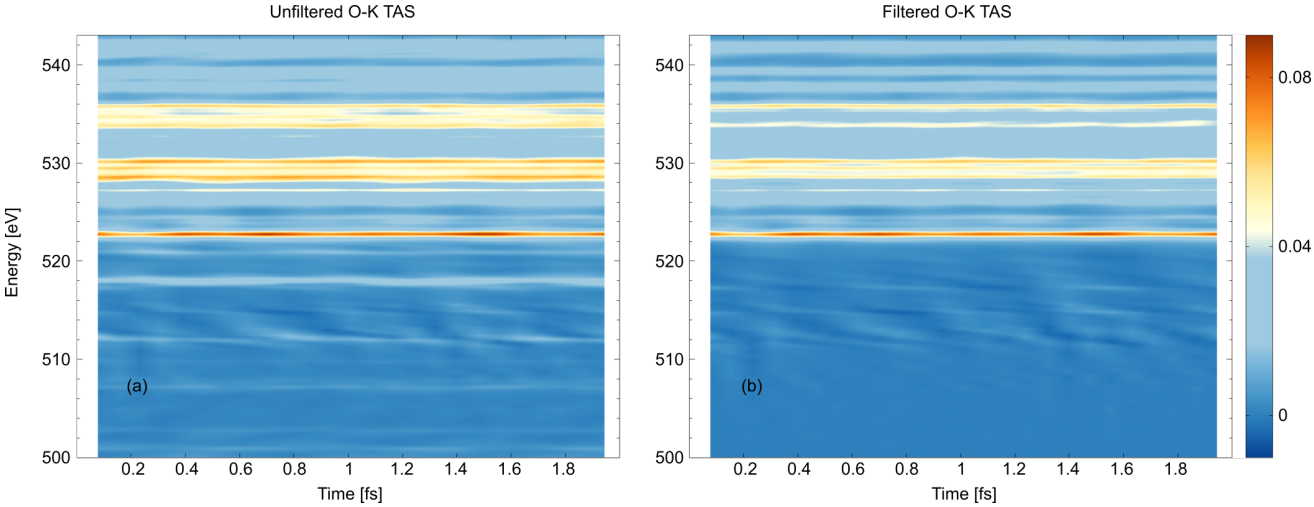

Figure A.3. The unfiltered (a) and filtered (b) oxygen K-edge transient absorption spectra for aminophenol computed using RT-TDDFT.

A.4. Optimized Geometries

A.4.1. Geometry of Aminophenol

Table A.1 shows the optimized geometry for 4-aminophenol (C_6H_7NO), optimized with the def2-TZVP basis set and PBE0 functional.

A.4.2. Geometry of SiO_2

For the simulation of α-quartz cluster, we used a bulk-mimicking approach and cut the cluster into a small cluster of $Si_5O_{16}H_{12}$. Table A.2 shows the basis sets used in the calculation for elements in different chemical environment, and the corresponding geome-

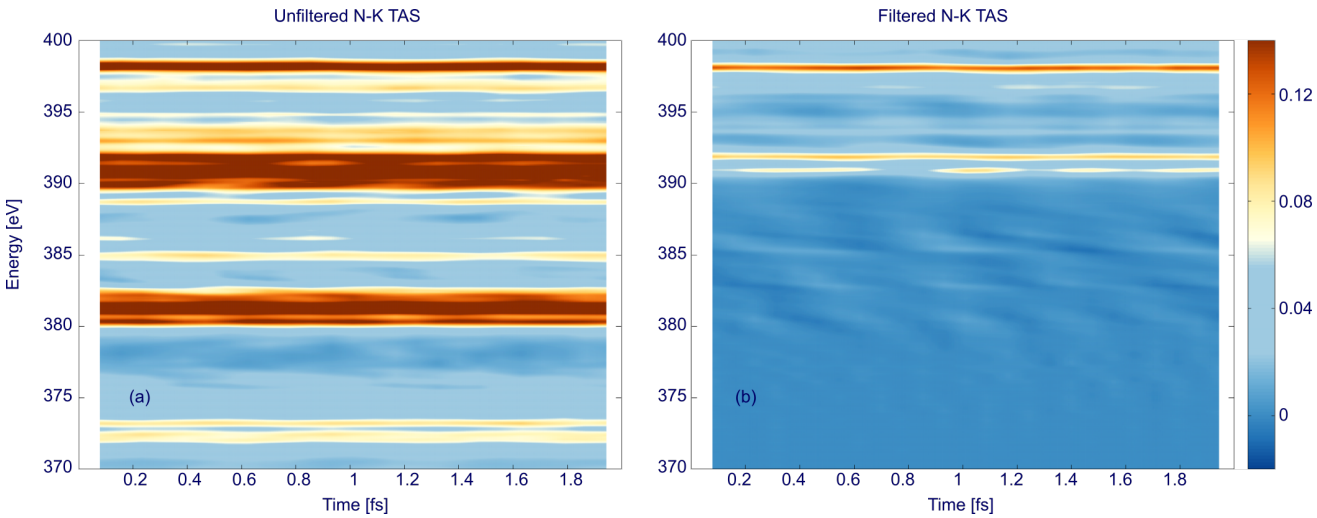

Figure A.4. The unfiltered (a) and filtered (b) nitrogen K-edge transient absorption spectra for aminophenol computed using RT-TDDFT.

try is in Table A.3.

Element	x[Å]	y[Å]	z[Å]
H	6.0653068925	-0.8634956830	0.0000000000
H	6.0481831800	0.8740807753	0.0000000000
N	5.5414526820	-0.0000000150	0.0000000000
C	4.1598046373	-0.0107741587	0.0000000000
O	0.0000000000	0.0000000000	0.0000000000
H	-0.3306292207	-0.9129732241	0.0000000000
C	1.3626150697	-0.0336215183	0.0000000000
H	3.9967231013	-2.1626123380	0.0000000000
H	1.5407431623	-2.1893718973	0.0000000000
C	3.4573836308	-1.2193772615	0.0000000000
C	2.0590797360	-1.2363743604	0.0000000000
C	3.4389159956	1.1860787402	0.0000000000
C	2.0418068713	1.1771570584	0.0000000000
H	3.9590876682	2.1397023442	0.0000000000
H	1.4892309327	2.1118826516	0.0000000000

Table A.1. Optimized geometry for 4-aminophenol

Element with numbering	Role	Basis set
Si1	absorbing center	def2-TZVPPD
Si2	bridging element	Stuttgart RLC ECP
O1	bridging element	def2-SVPD
O2	boundary element	Stuttgart RLC ECP
H	capping element	STO-3G

Table A.2. Basis sets for the bulk-mimicking cluster $Si_5O_{16}H_{12}$ for α-quartz

Element with numbering	x[Å]	y[Å]	z[Å]
Si1	0.3922109500	-0.0354317600	0.0525048900
O1	1.8064191800	-0.7752149700	0.0308350600
O1	0.1144270400	0.5837297400	-1.4083506500
O1	0.4332984900	1.1485666200	1.1343665400
O2	-0.7861223600	-1.0524208400	0.4601055700
Si2	2.2958868400	-2.3366187600	0.2440999700
Si2	-0.5998206400	1.8026650700	-2.2330827700
Si2	0.3431285000	2.4294386000	2.1119695400
Si2	-2.0408565400	-1.8702062000	-0.2109781100
O2	2.3000976100	-2.5111419800	1.9249722200
O2	1.3336644000	-3.4029314400	-0.5988118400
O2	3.8790006500	-2.5396359300	-0.3096555900
H	2.7040421300	-3.2846536000	2.4133456400
H	0.3409481700	-3.4003920400	-0.7192611300
H	4.0756737100	-2.9400459800	-1.2046368700
O2	-0.5573564200	3.2440327100	-1.4182693900
O2	-2.1707683900	1.1739237800	-2.5152185300
O2	0.0325948300	2.0325652300	-3.7738956000
H	-0.5173221100	3.4434101800	-0.4391647600
H	-2.7697429300	1.5439034100	-3.2253907400
H	0.6998403600	2.7426444300	-3.9987754200
O2	-0.6871791300	2.2877814200	3.4233443200
O2	1.8502602000	2.8546892500	2.7171974900
O2	-0.3624921300	3.6360352300	1.1280183200
H	-0.4245527500	1.9512163300	4.3276403600
H	2.7308698800	2.7577866500	2.2533694100
H	-0.7838653200	4.4575892400	1.5120673300
O2	-3.0877983800	-2.5106124600	0.9411173100
O2	-2.9167090200	-0.9552305400	-1.2765694900
O2	-1.2479783000	-3.2273302100	-0.8911987700
H	-3.9525879000	-2.0756446500	1.1919999300
H	-2.6607545800	-0.1475428800	-1.8077266900
H	-1.7418397000	-4.0172683500	-1.2546525300

Table A.3. Optimized geometry for bulk-mimicking cluster $Si_5O_{16}H_{12}$ in xyz format

A.5. Unitary Transformations for Switching Basis

In this section we briefly describe how to switch between the different bases in an RT-TDDFT simulations that uses Gaussian atomic orbitals (AOs). Here we AOs as $\{\phi_\mu\}$ and canonical orbitals (COs) as $\{\phi'_\mu\}$.

$$\phi'_i = X_{\mu i}\phi_\mu \tag{A.1}$$

Using a canonical scheme, $\mathbf{X}$ is the transformation matrix given by,

$$\mathbf{X} = \mathbf{U}\mathbf{s}^{-\frac{1}{2}} \tag{A.2}$$

with $\mathbf{U}$ and $\mathbf{s}$ being the eigenvector and eigenvalue matrices of the one-electron overlap matrix $\mathbf{S}$ evaluated in AOs basis, respectively. Without linear dependencies in the basis, $\mathbf{X}$ is a $n \times n$ matrix, where n is the number of atomic orbitals. With linear dependencies, it is $n \times m$, where $m < n$ is the number of canonical orbitals.

The molecular orbitals (MOs) can be constructed from either COs or AOs following an SCF calculation, with the coefficients C ($n \times m$) or $\mathbf{C}'$ ($m \times m$), respectively,

$$\Phi_i = \sum_\mu C_{\mu i}\phi_\mu \tag{A.3}$$

$$= \sum_\mu C'_{\mu i}\phi'_\mu \tag{A.4}$$

When using Gaussians as a basis, the matrix elements of an operator $\hat{A}$ are typically computed in the AO basis for efficiency reasons:

$$A_{\mu\nu} = \langle\phi_\mu|\hat{A}|\phi_\nu\rangle \tag{A.5}$$

Switching between bases during the time propagation involves a set of unitary transformations. For the Fock matrix $\mathbf{F}$ and dipole matrix $\mathbf{D}$ these are straightforward,

$$\mathbf{F}' = \mathbf{X}^\dagger\mathbf{F}\mathbf{X} \tag{A.6}$$

$$\mathbf{D}' = \mathbf{X}^{\dagger}\mathbf{D}\mathbf{X} \tag{A.7}$$

According to Roothaan equation,

$$\mathbf{F}'\mathbf{C}' = \mathbf{C}'\epsilon \tag{A.8}$$

by diagonalizing the $\mathbf{F}'$ the coefficient matrix $\mathbf{C}'$ and eigenenergies matrix ϵ can be obtained. The relationship between the coefficient matrices of canonical and atomic orbital is,

$$\mathbf{C} = \mathbf{X}\mathbf{C}' \tag{A.9}$$

With the coefficient matrix in hand, we can project the dipole matrix into the MOs,

$$\mathbf{D}^{\mathrm{MO}} = \mathbf{C}^{\dagger}\mathbf{D}\mathbf{C} \tag{A.10}$$

with the inverse to Eq. A.10 being in the case where the basis functions are not linear-dependent,

$$\mathbf{D} = \mathbf{C}\mathbf{D}^{\mathrm{MO}}\mathbf{C}^{\dagger} \tag{A.11}$$

When the linear dependency occurs, the matrix $\mathbf{C}$ is not square either, and the transformation between MO and AO will be,

$$\mathbf{D} = \mathbf{C}_{\mathbf{L}}^{-\mathbf{1}}\mathbf{D}^{\mathrm{MO}}(\mathbf{C}_{\mathbf{R}}^{-\mathbf{1}})^{\dagger} \tag{A.12}$$

with $\mathbf{C_L}$ and $\mathbf{C_R}$ being the left and right pseudoinverse vectors of $\mathbf{C}$, where

$$\mathbf{C_L}^{-1} = (\mathbf{C}^{\dagger}\mathbf{C})^{-1}\mathbf{C}^{\dagger} \tag{A.13}$$

$$(\mathbf{C_R}^{-1})^{\dagger} = \mathbf{C}(\mathbf{C}^{\dagger}\mathbf{C})^{-1} \tag{A.14}$$

The density matrix in AOs can be calculated directly from $\mathbf{P}'$

$$\mathbf{P} = \mathbf{X}\mathbf{P}'\mathbf{X}^{\dagger} \tag{A.15}$$

Because the transformation matrix $\mathbf{X}$ is not necessarily square and the inverse transformation is more complicated,

$$\mathbf{F} = \mathbf{Y}^{\dagger}\mathbf{F}'\mathbf{Y} \tag{A.16}$$

$$\mathbf{D} = \mathbf{Y}^{\dagger}\mathbf{D}'\mathbf{Y} \tag{A.17}$$

$$\mathbf{P}' = \mathbf{Y}^{\dagger}\mathbf{P}\mathbf{Y} \tag{A.18}$$

where the inverse transformation matrix is given by $\mathbf{Y} = \mathbf{U}\mathbf{s}^{\frac{1}{2}}$.

Appendix B. Publication Agreements and Permissions

Intruder Peak-Free Transient Inner-Shell Spectra Using Real-Time Simulations.

Yang, M., Sissay, A., Chen, M. and Lopata, K., 2022. *Journal of Chemical Theory and Computation*, 18(2), pp.992-1002.

Link for this article: `https://pubs.acs.org/doi/abs/10.1021/acs.jctc.1c00079`

The following is a proof of copyright permission.

From: Copyright <Copyright@ACS.org>
Sent: Monday, March 27, 2023 10:07 AM
To: Mengqi Yang <myang14@lsu.edu>; Copyright <Copyright@ACS.org>
Subject: RE: Permission for using published paper in dissertation

Dear Mengqi Yang,

In reference to your message below, the following is from the **American Chemical Society's Policy on Theses and Dissertations:**
This policy addresses permission to include **your article**(s) or portions of text from **your article**(s) in your thesis.

Reuse/Republication of the Entire Work in Theses or Collections: Authors may reuse all or part of the Submitted, Accepted or Published Work in a thesis or dissertation that the author writes and is required to submit to satisfy the criteria of degree-granting institutions. Such reuse is permitted subject to the ACS' "Ethical Guidelines to Publication of Chemical Research". Appropriate citation of the Published Work must be made as follows:
"Reprinted with permission from [COMPLETE REFERENCE CITATION]. Copyright [YEAR] American Chemical Society." Insert the appropriate wording in place of the capitalized words. Citation information may be found after the "Cite this:" heading below the title of the online version and at the bottom of **the first page of the pdf or print version of your ACS journal article**.
If the thesis or dissertation to be published is in electronic format, a direct link to the Published Work must also be included using the ACS Articles on Request author-directed link.
Submission to a Dissertation Distributor: If you plan to submit your thesis to UMI or to another dissertation distributor, you should not include the unpublished ACS paper in your thesis if the thesis will be disseminated electronically, until ACS has published your paper. After publication of the paper by ACS, you may release the entire thesis (**not the individual ACS article by itself**) for electronic dissemination through the distributor; ACS's copyright credit line should be printed on the first page of the ACS paper.

As such, please consider this email confirmation that your request to use the material as described is granted.
I hope this information is helpful.
Sincerely,

Keri Travis *(she/her)*
Copyright Specialist
Office of the Secretary & General Counsel
American Chemical Society
1155 Sixteenth Street, NW
Washington, DC 20036
202-872-4368
202-604-2874
k_travis@acs.org

Mapping Static Core-Holes and Ring-Currents with X-ray Scattering.

Carrascosa, A. M.; Yang, M.; Yong, H.; Ma, L.; Kirrander, A.; Weber, P. M.;Lopata, K., 2021.*Faraday Discussions*, 228, 60–81.

Link for this article: `https://doi.org/10.1039/D0FD00124D`

The following is a proof of copyright permission.

References

(1) Rajski, S. R.; Jackson, B. A.; Barton, J. K. *Mutation Research/Fundamental and Molecular Mechanisms of Mutagenesis* **2000**, *447*, 49–72.

(2) Ikeura-Sekiguchi, H.; Sekiguchi, T. *Physical Review Letters* **2007**, *99*, 228102.

(3) Krausz, F.; Stockman, M. I. *Nature Photonics* **2014**, *8*, 205–213.

(4) Ponseca Jr, C. S.; Chabera, P.; Uhlig, J.; Persson, P.; Sundstrom, V. *Chemical Reviews* **2017**, *117*, 10940–11024.

(5) Popmintchev, T.; Chen, M.-C.; Popmintchev, D.; Arpin, P.; Brown, S.; Ališauskas, S.; Andriukaitis, G.; Balčiunas, T.; Mücke, O. D.; Pugzlys, A., et al. *Science* **2012**, *336*, 1287–1291.

(6) Serkez, S.; Geloni, G.; Tomin, S.; Feng, G.; Gryzlova, E.; Grum-Grzhimailo, A.; Meyer, M. *Journal of Optics* **2018**, *20*, 024005.

(7) Coffee, R. N.; Cryan, J. P.; Duris, J.; Helml, W.; Li, S.; Marinelli, A. *Philosophical Transactions of the Royal Society A* **2019**, *377*, 20180386.

(8) Duris, J.; Li, S.; Driver, T.; Champenois, E. G.; MacArthur, J. P.; Lutman, A. A.; Zhang, Z.; Rosenberger, P.; Aldrich, J. W.; Coffee, R., et al. *Nature Photonics* **2020**, *14*, 30–36.

(9) Driver, T.; Li, S.; Champenois, E. G.; Duris, J.; Ratner, D.; Lane, T. J.; Rosenberger, P.; Al-Haddad, A.; Averbukh, V.; Barnard, T., et al. *Physical Chemistry Chemical Physics* **2020**, *22*, 2704–2712.

(10) Schoenlein, R.; Elsaesser, T.; Holldack, K.; Huang, Z.; Kapteyn, H.; Murnane, M.; Woerner, M. *Philosophical Transactions of the Royal Society A* **2019**, *377*, 20180384.

(11) Shiner, A.; Schmidt, B.; Trallero-Herrero, C.; Wörner, H. J.; Patchkovskii, S.; Corkum, P. B.; Kieffer, J.; Légaré, F.; Villeneuve, D. *Nature Physics* **2011**, *7*, 464–467.

(12) Baker, S.; Robinson, J. S.; Haworth, C.; Teng, H.; Smith, R.; Chirilă, C. C.; Lein, M.; Tisch, J.; Marangos, J. P. *Science* **2006**, *312*, 424–427.

(13) Telle, H. R.; Steinmeyer, G.; Dunlop, A. E.; Stenger, J.; Sutter, D. H.; Keller, U. *Applied Physics B* **1999**, *69*, 327–332.

(14) Dietrich, P.; Krausz, F.; Corkum, P. *Optics Letters* **2000**, *25*, 16–18.

(15) Babushkin, I.; Galán, Á. J.; de Andrade, J. R. C.; Husakou, A.; Morales, F.; Kretschmar, M.; Nagy, T.; Vaičaitis, V.; Shi, L.; Zuber, D., et al. *Nature Physics* **2022**, *18*, 417–422.

(16) Schultze, M.; Fieß, M.; Karpowicz, N.; Gagnon, J.; Korbman, M.; Hofstetter, M.; Neppl, S.; Cavalieri, A. L.; Komninos, Y.; Mercouris, T., et al. *Science* **2010**, *328*, 1658–1662.

(17) Drescher, M.; Hentschel, M.; Kienberger, R.; Uiberacker, M.; Yakovlev, V.; Scrinzi, A.; Westerwalbesloh, T.; Kleineberg, U.; Heinzmann, U.; Krausz, F. *Nature* **2002**, *419*, 803–807.

(18) Cavalieri, A. L.; Müller, N.; Uphues, T.; Yakovlev, V. S.; Baltuška, A.; Horvath, B.; Schmidt, B.; Blümel, L.; Holzwarth, R.; Hendel, S., et al. *Nature* **2007**, *449*, 1029–1032.

(19) Tao, Z.; Chen, C.; Szilvási, T.; Keller, M.; Mavrikakis, M.; Kapteyn, H.; Murnane, M. *Science* **2016**, *353*, 62–67.

(20) Shi, X.; Liao, C.-T.; Tao, Z.; Cating-Subramanian, E.; Murnane, M. M.; Hernández-García, C.; Kapteyn, H. C. *Journal of Physics B: Atomic, Molecular and Optical Physics* **2020**, *53*, 184008.

(21) Santra, R.; Yakovlev, V. S.; Pfeifer, T.; Loh, Z.-H. *Physical Review A* **2011**, *83*, 033405.

(22) Li, J.; Ren, X.; Yin, Y.; Zhao, K.; Chew, A.; Cheng, Y.; Cunningham, E.; Wang, Y.; Hu, S.; Wu, Y., et al. *Nature Communications* **2017**, *8*, 186.

(23) Beck, A. R.; Neumark, D. M.; Leone, S. R. *Chemical Physics Letters* **2015**, *624*, 119–130.

(24) Gaarde, M. B.; Buth, C.; Tate, J. L.; Schafer, K. J. *Physical Review A* **2011**, *83*, 013419.

(25) Chu, W.-C.; Lin, C. *Physical Review A* **2012**, *85*, 013409.

(26) Han, S.; Zhao, K.; Chang, Z. *Sensors* **2022**, *22*, 7513.

(27) Wang, H.; Chini, M.; Chen, S.; Zhang, C.-H.; He, F.; Cheng, Y.; Wu, Y.; Thumm, U.; Chang, Z. *Physical Review Letters* **2010**, *105*, 143002.

(28) Ramasesha, K.; Leone, S. R.; Neumark, D. M. *Annual Review of Physical Chemistry* **2016**, *67*, 41–63.

(29) Misra, S.; Peak, D.; Niyogi, S. *Metallomics* **2010**, *2*, 710–717.

(30) Koningsberger, D.; Prins, R. *Chemical Analysis* **1988**, *92*.

(31) Stöhr, J., *NEXAFS spectroscopy*; Springer Science & Business Media: 2013; Vol. 25.

(32) De Groot, F.; Kotani, A., *Core level spectroscopy of solids*; CRC press: 2008.

(33) Pabst, S.; Sytcheva, A.; Moulet, A.; Wirth, A.; Goulielmakis, E.; Santra, R. *Physical Review A* **2012**, *86*, 063411.

(34) Wirth, A.; Santra, R.; Goulielmakis, E. *Chemical Physics* **2013**, *414*, 149–159.

(35) Goulielmakis, E.; Loh, Z.-H.; Wirth, A.; Santra, R.; Rohringer, N.; Yakovlev, V. S.; Zherebtsov, S.; Pfeifer, T.; Azzeer, A. M.; Kling, M. F., et al. *Nature* **2010**, *466*, 739–743.

(36) Wirth, A.; Hassan, M. T.; Grguraš, I.; Gagnon, J.; Moulet, A.; Luu, T. T.; Pabst, S.; Santra, R.; Alahmed, Z.; Azzeer, A., et al. *Science* **2011**, *334*, 195–200.

(37) Schultze, M.; Ramasesha, K.; Pemmaraju, C.; Sato, S.; Whitmore, D.; Gandman, A.; Prell, J. S.; Borja, L.; Prendergast, D.; Yabana, K., et al. *Science* **2014**, *346*, 1348–1352.

(38) Mashiko, H.; Oguri, K.; Yamaguchi, T.; Suda, A.; Gotoh, H. *Nature Physics* **2016**, *12*, 741–745.

(39) Wolf, T.; Myhre, R. H.; Cryan, J.; Coriani, S.; Squibb, R.; Battistoni, A.; Berrah, N.; Bostedt, C.; Bucksbaum, P.; Coslovich, G., et al. *Nature Communications* **2017**, *8*, 29.

(40) Scutelnic, V.; Tsuru, S.; Pápai, M.; Yang, Z.; Epshtein, M.; Xue, T.; Haugen, E.; Kobayashi, Y.; Krylov, A. I.; Møller, K. B., et al. *Nature Communications* **2021**, *12*, 5003.

(41) Matselyukh, D. T.; Despré, V.; Golubev, N. V.; Kuleff, A. I.; Wörner, H. J. *Nature Physics* **2022**, *18*, 1206–1213.

(42) Fu, Y.; Nishimura, K.; Shao, R.; Suda, A.; Midorikawa, K.; Lan, P.; Takahashi, E. J. *Communications Physics* **2020**, *3*, 92.

(43) Zinchenko, K. S.; Ardana-Lamas, F.; Lanfaloni, V. U.; Luu, T. T.; Pertot, Y.; Huppert, M.; Wörner, H. J. *Scientific Reports* **2023**, *13*, 3059.

(44) McMillan, W. *Physical Review A* **1972**, *6*, 936.

(45) Morikawa, Y.; Nishimura, S.-i.; Hashimoto, R.-i.; Ohnuma, M.; Yamada, A. *Advanced Energy Materials* **2020**, *10*, 1903176.

(46) Yong, H. et al. *Nature Communications* **2020**, *11*, 2157.

(47) Minitti, M. P. et al. *Physical Review Letters* **2015**, *114*, 255501.

(48) Stankus, B. et al. *Nature Chemistry* **2019**, *11*, 716–721.

(49) Ruddock, J. M. et al. *Science Advances* **2019**, *5*, 1.

(50) Ware, M. R.; Glownia, J. M.; Al-Sayyad, N.; O'Neal, J. T.; Bucksbaum, P. H. *Physical Review A* **2019**, *100*, 033413.

(51) Yong, H.; Xu, X.; Ruddock, J. M.; Stankus, B.; Carrascosa, A. M.; Zotev, N.; Bellshaw, D.; Du, W.; Goff, N.; Chang, Y., et al. *Proceedings of the National Academy of Sciences* **2021**, *118*, e2021714118.

(52) Emma, P.; Akre, R.; Arthur, J.; Bionta, R.; Bostedt, C.; Bozek, J.; Brachmann, A.; Bucksbaum, P.; Coffee, R.; Decker, F.-J., et al. *Nature Photonics* **2010**, *4*, 641–647.

(53) Malyzhenkov, A.; Arbelo, Y. P.; Craievich, P.; Dijkstal, P.; Ferrari, E.; Reiche, S.; Schietinger, T.; Juranić, P.; Prat, E. *Physical Review Research* **2020**, *2*, 042018.

(54) Langhoff, S. R.; Davidson, E. R. *International Journal of Quantum Chemistry* **1974**, *8*, 61–72.

(55) Shepard, R. et al. *Ab Initio Methods in Quantum Chemistry–II* **1987**, 63.

(56) Bartlett, R. J.; Musiał, M. *Reviews of Modern Physics* **2007**, *79*, 291.

(57) Slater, J. C. *Physical Review* **1951**, *81*, 385.

(58) Baerends, E.; Ellis, D.; Ros, P. *Chemical Physics* **1973**, *2*, 41–51.

(59) Fischer, C. F. **1977**.

(60) Hohenberg, P.; Kohn, W. *Physical Review* **1964**, *136*, B864.

(61) Sham, L. J.; Kohn, W. *Physical Review* **1966**, *145*, 561.

(62) Lopata, K.; Van Kuiken, B. E.; Khalil, M.; Govind, N. *Journal of Chemical Theory and Computation* **2012**, *8*, 3284–3292.

(63) Sonk, J. A.; Caricato, M.; Schlegel, H. B. *Journal of Physical Chemistry A* **2011**, *115*, 4678–4690.

(64) Hu, C.; Sugino, O.; Miyamoto, Y. *Physical Review A* **2006**, *74*, 032508.

(65) Liang, W.; Fischer, S. A.; Frisch, M. J.; Li, X. *Journal of Chemical Theory and Computation* **2011**, *7*, 3540–3547.

(66) Sato, T.; Ishikawa, K. L. *Physical Review A* **2013**, *88*, 023402.

(67) Ulusoy, I. S.; Stewart, Z.; Wilson, A. K. *The Journal of Chemical Physics* **2018**, *148*, 014107.

(68) Cederbaum, L. S.; Zobeley, J. *Chemical Physics Letters* **1999**, *307*, 205–210.

(69) Nascimento, D. R.; DePrince III, A. E. *Journal of Chemical Theory and Computation* **2016**, *12*, 5834–5840.

(70) Takimoto, Y.; Vila, F.; Rehr, J. *Journal of Chemical Physics* **2007**, *127*, 154114.

(71) Lopata, K.; Govind, N. *Journal of Chemical Theory and Computation* **2011**, *7*, 1344–1355.

(72) Isborn, C. M.; Li, X.; Tully, J. C. *The Journal of Chemical Physics* **2007**, *126*, 134307.

(73) Bruner, A.; Hernandez, S.; Mauger, F.; Abanador, P. M.; LaMaster, D. J.; Gaarde, M. B.; Schafer, K. J.; Lopata, K. *Journal of Physical Chemistry Letters* **2017**, *8*, 3991–3996.

(74) Folorunso, A. S.; Bruner, A.; Mauger, F.; Hamer, K. A.; Hernandez, S.; Jones, R. R.; DiMauro, L. F.; Gaarde, M. B.; Schafer, K. J.; Lopata, K. *Physical Review Letters* **2021**, *126*, 133002.

(75) Folorunso, A. S.; Mauger, F.; Hamer, K. A.; Jayasinghe, D. D.; Wahyutama, I. S.; Ragains, J. R.; Jones, R. R.; DiMauro, L. F.; Gaarde, M. B.; Schafer, K. J., et al. *The Journal of Physical Chemistry A* **2023**, *127*, 1894–1900.

(76) Mauger, F.; Folorunso, A. S.; Hamer, K. A.; Chandre, C.; Gaarde, M. B.; Lopata, K.; Schafer, K. J. *Physical Review Research* **2022**, *4*, 013073.

(77) Mauger, F.; Folorunso, A. S.; Hamer, K. A.; Chandre, C.; Gaarde, M. B.; Lopata, K.; Schafer, K. J. *hal02866922* **2021**.

(78) Telnov, D. A.; Sosnova, K. E.; Rozenbaum, E.; Chu, S.-I. *Physical Review A* **2013**, *87*, 053406.

(79) Sissay, A.; Abanador, P.; Mauger, F.; Gaarde, M.; Schafer, K. J.; Lopata, K. *Journal of Chemical Physics* **2016**, *145*, 094105.

(80) Wahyutama, I. S.; Jayasinghe, D. D.; Mauger, F.; Lopata, K.; Gaarde, M. B.; Schafer, K. J. *Physical Review A* **2022**, *106*, 052211.

(81) Nobusada, K.; Yabana, K. *Physical Review A* **2007**, *75*, 032518.

(82) Wachter, G.; Lemell, C.; Burgdörfer, J.; Sato, S. A.; Tong, X.-M.; Yabana, K. *Physical Review Letters* **2014**, *113*, 087401.

(83) Yabana, K.; Bertsch, G. F. *Zeitschrift für Physik D Atoms, Molecules and Clusters* **1997**, *42*, 219–225.

(84) Lopata, K.; Govind, N. *Journal of Chemical Theory and Computation* **2013**, *9*, 4939–4946.

(85) Bruner, A.; LaMaster, D.; Lopata, K. *Journal of Chemical Theory and Computation* **2016**, *12*, 3741–3750.

(86) Goings, J. J.; Kasper, J. M.; Egidi, F.; Sun, S.; Li, X. *The Journal of Chemical Physics* **2016**, *145*, 104107.

(87) Kawashita, Y.; Yabana, K.; Noda, M.; Nobusada, K.; Nakatsukasa, T. *Journal of Molecular Structure: THEOCHEM* **2009**, *914*, 130–135.

(88) Kadek, M.; Konecny, L.; Gao, B.; Repisky, M.; Ruud, K. *Physical Chemistry Chemical Physics* **2015**, *17*, 22566–22570.

(89) Repisky, M.; Konecny, L.; Kadek, M.; Komorovsky, S.; Malkin, O. L.; Malkin, V. G.; Ruud, K. *Journal of Chemical Theory and Computation* **2015**, *11*, 980–991.

(90) Fernando, R. G.; Balhoff, M. C.; Lopata, K. *Journal of Chemical Theory and Computation* **2015**, *11*, 646–654.

(91) Darapaneni, P.; Meyer, A. M.; Sereda, M.; Bruner, A.; Dorman, J. A.; Lopata, K. *Journal of Chemical Physics* **2020**, *153*, 054110.

(92) Chen, M.; Lopata, K. *Journal of Chemical Theory and Computation* **2020**.

(93) De Giovannini, U.; Brunetto, G.; Castro, A.; Walkenhorst, J.; Rubio, A. *ChemPhysChem* **2013**, *14*, 1363–1376.

(94) Pemmaraju, C. *arXiv preprint arXiv:2006.02034* **2020**.

(95) Dutoi, A. D.; Cederbaum, L. S. *Physical Review A* **2014**, *90*, 023414.

(96) Dutoi, A. D.; Gokhberg, K.; Cederbaum, L. S. *Physical Review A* **2013**, *88*, 013419.

(97) Golubev, N. V.; Vaníček, J.; Kuleff, A. I. *Physical Review Letters* **2021**, *127*, 123001.

(98) Chew, A.; Douguet, N.; Cariker, C.; Li, J.; Lindroth, E.; Ren, X.; Yin, Y.; Argenti, L.; Hill III, W. T.; Chang, Z. *Physical Review A* **2018**, *97*, 031407.

(99) Lucchini, M.; Sato, S. A.; Ludwig, A.; Herrmann, J.; Volkov, M.; Kasmi, L.; Shinohara, Y.; Yabana, K.; Gallmann, L.; Keller, U. *Science* **2016**, *353*, 916–919.

(100) Kobayashi, Y.; Neumark, D. M.; Leone, S. R. *Optics Express* **2022**, *30*, 5673–5682.

(101) Provorse, M. R.; Habenicht, B. F.; Isborn, C. M. *Journal of Chemical Theory and Computation* **2015**, *11*, 4791–4802.

(102) Kaduk, B.; Kowalczyk, T.; Van Voorhis, T. *Chemical Reviews* **2012**, *112*, 321–370.

(103) Ben-Nun, M.; Martinez, T. J.; Weber, P. M.; Wilson, K. R. *Chemical Physics Letters* **1996**, *262*, 405.

(104) Ben-Nun, M.; Cao, J.; Wilson, K. R. *The Journal of Physical Chemistry A* **1997**, *101*, 8743–8761.

(105) Cao, J.; Wilson, K. R. *The Journal of Physical Chemistry A* **1998**, *102*, 9523–9530.

(106) Kirrander, A.; Saita, K.; Shalashilin, D. V. *Journal of Chemical Theory and Computation* **2016**, *12*, 957–967.

(107) Yong, H.; Zotev, N.; Stankus, B.; Ruddock, J. M.; Bellshaw, D.; Boutet, S.; Lane, T. J.; Liang, M.; Carbajo, S.; Robinson, J. S., et al. *The Journal of Physical Chemistry Letters* **2018**, *9*, 6556–6562.

(108) Stankus, B.; Yong, H.; Ruddock, J.; Ma, L.; Carrascosa, A. M.; Goff, N.; Boutet, S.; Xu, X.; Zotev, N.; Kirrander, A., et al. *Journal of Physics B: Atomic, Molecular and Optical Physics* **2020**, *53*, 234004.

(109) Simmermacher, M.; Moreno Carrascosa, A.; Henriksen, N. E.; Møller, K. B.; Kirrander, A. *The Journal of Chemical Physics* **2019**, *151*, 174302.

(110) Dixit, G.; Vendrell, O.; Santra, R. *Proceedings of the National Academy of Sciences* **2012**, *109*, 11636.

(111) Carrascosa, A. M.; Kirrander, A. *Physical Chemistry Chemical Physics* **2017**, *19*, 19545–19553.

(112) Moreno Carrascosa, A.; Yong, H.; Crittenden, D. L.; Weber, P. M.; Kirrander, A. *Journal of Chemical Theory and Computation* **2019**, *15*, 2836–2846.

(113) Hermann, G.; Pohl, V.; Dixit, G.; Tremblay, J. C. *Physical Review Letters* **2020**, *124*, 013002.

(114) Simmermacher, M.; Henriksen, N. E.; Møller, K. B.; Moreno Carrascosa, A.; Kirrander, A. *Physical Review Letters* **2019**, *122*, 073003.

(115) Goings, J. J.; Lestrange, P. J.; Li, X. *Wiley Interdiscip. Rev. Comput. Mol. Sci.* **2018**, *8*, e1341.

(116) Li, X.; Govind, N.; Isborn, C.; DePrince III, A. E.; Lopata, K. *Chemical Reviews* **2020**.

(117) Szabo, A.; Ostlund, N. S., *Modern quantum chemistry: introduction to advanced electronic structure theory*; Courier Corporation: 2012.

(118) Krause, P.; Klamroth, T.; Saalfrank, P. *Journal of Chemical Physics* **2005**, *123*, 074105.

(119) Kohn, W.; Sham, L. J. *Physical Review* **1965**, *140*, A1133.

(120) Orio, M.; Pantazis, D. A.; Neese, F. *Photosynthesis Research* **2009**, *102*, 443–453.

(121) Sholl, D. S.; Steckel, J. A., *Density functional theory: a practical introduction*; John Wiley & Sons: 2022.

(122) Koch, W.; Holthausen, M. C., *A chemist's guide to density functional theory*; John Wiley & Sons: 2015.

(123) Becke, A. D. *Physical Review A* **1988**, *38*, 3098.

(124) Perdew, J. P.; Burke, K.; Ernzerhof, M. *Physical Review Letters* **1996**, *77*, 3865.

(125) Becke, A. D. *The Journal of Chemical Physics* **1993**, *98*, 1372–1377.

(126) Baer, R.; Livshits, E.; Salzner, U. *Annual Review of Physical Chemistry* **2010**, *61*, 85–109.

(127) Tussupbayev, S.; Govind, N.; Lopata, K.; Cramer, C. J. *Journal of Chemical Theory and Computation* **2015**, *11*, 1102–1109.

(128) Isborn, C. M.; Li, X. *The Journal of Chemical Physics* **2008**, *129*, 204107.

(129) Fuks, J. I.; Luo, K.; Sandoval, E. D.; Maitra, N. T. *Physical Review Letters* **2015**, *114*, 183002.

(130) Habenicht, B. F.; Tani, N. P.; Provorse, M. R.; Isborn, C. M. *The Journal of Chemical Physics* **2014**, *141*, 184112.

(131) Fischer, S. A.; Cramer, C. J.; Govind, N. *Journal of Chemical Theory and Computation* **2015**, *11*, 4294–4303.

(132) Chapman, C. T.; Liang, W.; Li, X. *The Journal of Physical Chemistry Letters* **2011**, *2*, 1189–1192.

(133) Wu, Q.; Van Voorhis, T. *Physical Review A* **2005**, *72*, 024502.

(134) Castro, A.; Marques, M. A.; Rubio, A. *Journal of Chemical Physics* **2004**, *121*, 3425–3433.

(135) Engel, G. S.; Calhoun, T. R.; Read, E. L.; Ahn, T.-K.; Mančal, T.; Cheng, Y.-C.; Blankenship, R. E.; Fleming, G. R. *Nature* **2007**, *446*, 782–786.

(136) Andrade, X.; Hamel, S.; Correa, A. A. *The European Physical Journal B* **2018**, *91*, 1–7.

(137) Schultze, M.; Bothschafter, E. M.; Sommer, A.; Holzner, S.; Schweinberger, W.; Fiess, M.; Hofstetter, M.; Kienberger, R.; Apalkov, V.; Yakovlev, V. S., et al. *Nature* **2013**, *493*, 75–78.

(138) Mauritsson, J.; Remetter, T.; Swoboda, M.; Klünder, K.; L'Huillier, A.; Schafer, K.; Ghafur, O.; Kelkensberg, F.; Siu, W.; Johnsson, P., et al. *Physical Review Letters* **2010**, *105*, 053001.

(139) Ruberti, M. *Faraday Discussions* **2021**, *228*, 286–311.

(140) Holler, M.; Schapper, F.; Gallmann, L.; Keller, U. *Physical Review Letters* **2011**, *106*, 123601.

(141) Zürch, M.; Chang, H.-T.; Borja, L. J.; Kraus, P. M.; Cushing, S. K.; Gandman, A.; Kaplan, C. J.; Oh, M. H.; Prell, J. S.; Prendergast, D., et al. *Nature Communications* **2017**, *8*, 1–11.

(142) Iannuzzi, M.; Hutter, J. *Physical Chemistry Chemical Physics* **2007**, *9*, 1599–1610.

(143) Björneholm, O.; Federmann, F.; Fössing, F.; Möller, T. *Physical Review Letters* **1995**, *74*, 3017.

(144) Wenzel, J.; Wormit, M.; Dreuw, A. *Journal of Chemical Theory and Computation* **2014**, *10*, 4583–4598.

(145) Wenzel, J.; Holzer, A.; Wormit, M.; Dreuw, A. *Journal of Chemical Physics* **2015**, *142*, 214104.

(146) Dreuw, A.; Wormit, M. *Wiley Interdisciplinary Reviews: Computational Molecular Science* **2015**, *5*, 82–95.

(147) Southworth, S. H.; Wehlitz, R.; Picón, A.; Lehmann, C. S.; Cheng, L.; Stanton, J. F. *Journal of Chemical Physics* **2015**, *142*, 224302.

(148) Peng, B.; Lestrange, P. J.; Goings, J. J.; Caricato, M.; Li, X. *Journal of Chemical Theory and Computation* **2015**, *11*, 4146–4153.

(149) Liu, J.; Matthews, D.; Coriani, S.; Cheng, L. *Journal of Chemical Theory and Computation* **2019**, *15*, 1642–1651.

(150) Nascimento, D. R.; DePrince III, A. E. *Journal of Physical Chemistry Letters* **2017**, *8*, 2951–2957.

(151) Gilmore, K.; Vinson, J.; Shirley, E. L.; Prendergast, D.; Pemmaraju, C. D.; Kas, J. J.; Vila, F. D.; Rehr, J. J. *Computer Physics Communications* **2015**, *197*, 109–117.

(152) Vinson, J.; Rehr, J.; Kas, J.; Shirley, E. *Physical Review B* **2011**, *83*, 115106.

(153) Triguero, L.; Pettersson, L.; Ågren, H. *Physical Review B* **1998**, *58*, 8097.

(154) Hait, D.; Head-Gordon, M. *The Journal of Physical Chemistry Letters* **2021**, *12*, 4517–4529.

(155) Derricotte, W. D.; Evangelista, F. A. *Physical Chemistry Chemical Physics* **2015**, *17*, 14360–14374.

(156) Taillefumier, M.; Cabaret, D.; Flank, A.-M.; Mauri, F. *Physical Review B* **2002**, *66*, 195107.

(157) Altman, A. B.; Pemmaraju, C.; Camp, C.; Arnold, J.; Minasian, S. G.; Prendergast, D.; Shuh, D. K.; Tyliszczak, T. *Journal of the American Chemical Society* **2015**, *137*, 10304–10316.

(158) Stratmann, R. E.; Scuseria, G. E.; Frisch, M. J. *Journal of Chemical Physics* **1998**, *109*, 8218–8224.

(159) Christiansen, O.; Halkier, A.; Koch, H.; Jo/rgensen, P.; Helgaker, T. *Journal of Chemical Physics* **1998**, *108*, 2801–2816.

(160) Parker, S. M.; Rappoport, D.; Furche, F. *Journal of Chemical Theory and Computation* **2018**, *14*, 807–819.

(161) Cronstrand, P.; Luo, Y.; Ågren, H. *Chemical Physics Letters* **2002**, *352*, 262–269.

(162) Friese, D. H.; Hättig, C.; Ruud, K. *Physical Chemistry Chemical Physics* **2012**, *14*, 1175–1184.

(163) Luo, Y.; Jonsson, D.; Norman, P.; Ruud, K.; Vahtras, O.; Minaev, B.; Ågren, H.; Rizzo, A.; Mikkelsen, K. *International Journal of Quantum Chemistry* **1998**, *70*, 219–239.

(164) Norman, P.; Luo, Y.; Ågren, H. *Chemical Physics Letters* **1998**, *296*, 8–18.

(165) Vaara, J.; Ruud, K.; Vahtras, O.; Ågren, H.; Jokisaari, J. *Journal of Chemical Physics* **1998**, *109*, 1212–1222.

(166) Stener, M.; Fronzoni, G.; de Simone, M. d. *Chemical Physics Letters* **2003**, *373*, 115–123.

(167) Jaszewski, A. R.; Stranger, R.; Pace, R. J. *Physical Chemistry Chemical Physics* **2009**, *11*, 5634–5642.

(168) Zhang, Y.; Biggs, J. D.; Healion, D.; Govind, N.; Mukamel, S. *Journal of Chemical Physics* **2012**, *137*, 194306.

(169) Ray, K.; DeBeer George, S.; Solomon, E. I.; Wieghardt, K.; Neese, F. *Chemistry - A European Journal* **2007**, *13*, 2783–2797.

(170) Tsuchimochi, T.; Kobayashi, M.; Nakata, A.; Imamura, Y.; Nakai, H. *Journal of Computational Chemistry* **2008**, *29*, 2311–2316.

(171) Atkins, A. J.; Jacob, C. R.; Bauer, M. *Chemistry - A European Journal* **2012**, *18*, 7021–7025.

(172) Lestrange, P. J.; Nguyen, P. D.; Li, X. *Journal of Chemical Theory and Computation* **2015**, *11*, 2994–2999.

(173) Verma, P.; Bartlett, R. J. *Journal of Chemical Physics* **2014**, *140*, 18A534.

(174) Nakata, A.; Imamura, Y.; Otsuka, T.; Nakai, H. *Journal of Chemical Physics* **2006**, *124*, 094105.

(175) Akama, T.; Nakai, H. *Journal of Chemical Physics* **2010**, *132*, 054104.

(176) Akama, T.; Imamura, Y.; Nakai, H. *Chemistry Letters* **2010**, *39*, 407–409.

(177) Cho, D.; Rouxel, J. R.; Kowalewski, M.; Lee, J.; Mukamel, S. *Philos. Trans. Royal Soc. A* **2019**, *377*, 20170470.

(178) Kasper, J. M.; Lestrange, P. J.; Stetina, T. F.; Li, X. *Journal of Chemical Theory and Computation* **2018**, *14*, 1998–2006.

(179) Pemmaraju, C. *Computational Condensed Matter* **2019**, *18*, e00348.

(180) De Giovannini, U.; Brunetto, G.; Castro, A.; Walkenhorst, J.; Rubio, A. *Computer Physics Communications* **2013**, *14*, 1363–1376.

(181) Trcera, N.; Cabaret, D.; Farges, F.; Flank, A.-M.; Lagarde, P.; Rossano, S. In *AIP Conference Proceedings*, 2007; Vol. 882, pp 226–228.

(182) Cabaret, D.; Mauri, F.; Henderson, G. S. *Physical Review B* **2007**, *75*, 184205.

(183) Prendergast, D.; Galli, G. *Physical Review Letters* **2006**, *96*, 215502.

(184) Uejio, J. S.; Schwartz, C. P.; Saykally, R. J.; Prendergast, D. *Chemical Physics Letters* **2008**, *467*, 195–199.

(185) Dong, S. S.; Gagliardi, L.; Truhlar, D. G. *Journal of Chemical Theory and Computation* **2019**, *15*, 4591–4601.

(186) Ciofini, I.; Adamo, C. *Journal of Physical Chemistry A* **2007**, *111*, 5549–5556.

(187) Karamatskou, A.; Pabst, S.; Chen, Y.-J.; Santra, R. *Physical Review A* **2014**, *89*, 033415.

(188) Santra, R.; Cederbaum, L. S. *Physics Reports* **2002**, *368*, 1–117.

(189) Santra, R.; Cederbaum, L. S. *Journal of Chemical Physics* **2002**, *117*, 5511–5521.

(190) Feuerbacher, S.; Sommerfeld, T.; Santra, R.; Cederbaum, L. S. *Journal of Chemical Physics* **2003**, *118*, 6188–6199.

(191) Norman, P.; Bishop, D. M.; Jo/rgen Aa. Jensen, H.; Oddershede, J. *Journal of Chemical Physics* **2001**, *115*, 10323–10334.

(192) Jensen, L.; Autschbach, J.; Schatz, G. C. *Journal of Chemical Physics* **2005**, *122*, 224115.

(193) Krause, P.; Schlegel, H. B. *Journal of Physical Chemistry Letters* **2015**, *6*, 2140–2146.

(194) Schelter, I.; Kümmel, S. *Journal of Chemical Theory and Computation* **2018**, *14*, 1910–1927.

(195) Neville, S. P.; Schuurman, M. S. *Journal of Chemical Physics* **2018**, *149*, 154111.

(196) Valiev, M.; Bylaska, E. J.; Govind, N.; Kowalski, K.; Straatsma, T. P.; Van Dam, H. J.; Wang, D.; Nieplocha, J.; Apra, E.; Windus, T. L., et al. *Computer Physics Communications* **2010**, *181*, 1477–1489.

(197) Adamo, C.; Barone, V. *Journal of Chemical Physics* **1999**, *110*, 6158–6170.

(198) Nekrashevich, S.; Gritsenko, V. *Physics of the Solid State* **2014**, *56*, 207–222.

(199) Yin, K.; Lin, H.; Cai, Q.; Zhao, Y.; Lee, S.-T.; Hu, F.; Shao, M. *Nanoscale* **2013**, *5*, 12330–12334.

(200) Que, R.; Shao, M.; Wang, S.; Ma, D. D. D.; Lee, S.-T. *Nano Letters* **2011**, *11*, 4870–4873.

(201) Binggeli, N.; Troullier, N.; Martins, J. L.; Chelikowsky, J. R. *Physical Review B* **1991**, *44*, 4771.

(202) Taillefumier, M.; Cabaret, D.; Flank, A.-M.; Mauri, F. *Physical Review B* **2002**, *66*, 195107.

(203) Baer, R.; Livshits, E.; Salzner, U. *Annual Review of Physical Chemistry* **2010**, *61*, 85–109.

(204) Li, D.; Bancroft, G.; Kasrai, M.; Fleet, M.; Secco, R.; Feng, X.; Tan, K.; Yang, B. *American Mineralogist* **1994**, *79*, 622–632.

(205) Hansen, P. L.; Brydson, R.; McComb, D. W. *Microscopy Microanalysis Microstructures* **1992**, *3*, 213–219.

(206) Sissay, A.; Chen, M.; Yang, M.; Meyer, A.; Lopata, K., *manuscript in preparation.*

(207) Ruddock, J. M.; Zotev, N.; Stankus, B.; Yong, H.-W.; Bellshaw, D.; Boutet, S.; Lane, T. J.; Liang, M.; Carbajo, S.; Du, W.; Kirrander, A.; Minitti, M. P.; Weber, P. M. *Angewandte Chemie* **2019**, *131*, 6437–6441.

(208) Yong, H. et al. *The Journal of Physical Chemistry Letters* **2018**, *9*, 6556–6562.

(209) Minitti, M. P.; Budarz, J. M.; Kirrander, A.; Robinson, J.; Lane, T. J.; Ratner, D.; Saita, K.; Northey, T.; Stankus, B.; Cofer-Shabica, V.; Hastings, J.; Weber, P. M. *Faraday Discussions* **2014**, *171*, 81.

(210) Yong, H. et al. *The Journal of Chemical Physics* **2019**, *151*, 084301.

(211) Stefanou, M.; Saita, K.; Shalashilin, D. V.; Kirrander, A. *Chemical Physics Letters* **2017**, *683*, 300–305.

(212) Ma, L.; Yong, H.; Geiser, J. D.; Moreno Carrascosa, A.; Goff, N.; Weber, P. M. *Structural Dynamics* **2020**, *7*, 034102.

(213) Santra, R. *Journal of Physics B: Atomic, Molecular and Optical Physics* **2009**, *42*, 023001.

(214) Lorenz, U.; Møller, K. B.; Henriksen, N. E. *Physical Review A* **2010**, *81*, 023422.

(215) Møller, K. B.; Henriksen, N. E. *Molecular Electronic Structures of Transition Metal Complexes I* **2012**, *142*, 185.

(216) Cao, J.; Wilson, K. R. *The Journal of Physical Chemistry A* **1998**, *102*, 9523.

(217) Bratos, S.; Mirloup, F.; Vuilleumier, R.; Wulff, M. *The Journal of Chemical Physics* **2002**, *116*, 10615.

(218) Simmermacher, M.; Henriksen, N. E.; Møller, K. B. *Physical Chemistry Chemical Physics* **2017**, *19*, 19740–19749.

(219) Kowalewski, M.; Bennett, K.; Mukamel, S. *Structural Dynamics* **2017**, *4*, 054101.

(220) Bardeen, C. J.; Che, J.; Wilson, K. R.; Yakovlev, V. V.; Apkarian, V. A.; Martens, C. C.; Zadoyan, R.; Kohler, B.; Messina, M. *The Journal of Chemical Physics* **1997**, *106*, 8486.

(221) Lorenz, U.; Møller, K. B.; Henriksen, N. E. *New Journal of Physics* **2010**, *12*, 113022.

(222) Dixit, G.; Santra, R. *Physical Review A* **2017**, *96*, 053413.

(223) Arnold, C.; Vendrell, O.; Santra, R. *Physical Review A* **2017**, *95*, 033425.

(224) Föhlisch, A.; Feulner, P.; Hennies, F.; Fink, A.; Menzel, D.; Sanchez-Portal, D.; Echenique, P.; Wurth, W. *Nature* **2005**, *436*, 373–376.

(225) Friend, R.; Bradley, D.; Townsend, P. *Journal of Physics D: Applied Physics* **1987**, *20*, 1367.

(226) Bauch, S.; Sørensen, L. K.; Madsen, L. B. *Physical Review A* **2014**, *90*, 062508.

(227) Popova-Gorelova, D.; Santra, R. *Physical Review B* **2015**, *92*, 184304.

(228) Bredtmann, T.; Ivanov, M.; Dixit, G. *Nature Communications* **2014**, *5*, 5589.

(229) Juse, J.; Sundholm, D., et al. *Physical Chemistry Chemical Physics* **1999**, *1*, 3429–3435.

(230) Amos, A.; Roberts, H. F. *The Journal of Chemical Physics* **1969**, *50*, 2375–2381.

(231) Stankus, B.; Budarz, J. M.; Kirrander, A.; Rogers, D.; Robinson, J.; Lane, T. J.; Ratner, D.; Hastings, J.; Minitti, M. P.; Weber, P. M. *Faraday Discussions* **2016**, *194*, 525–536.

(232) Stankus, B.; Zotev, N.; Rogers, D. M.; Gao, Y.; Odate, A.; Kirrander, A.; Weber, P. M. *The Journal of Chemical Physics* **2018**, *148*, 194306.

(233) Wolf, T. J. A. et al. *Nature Chemistry* **2019**, *11*, 504–509.

(234) Itala, E.; Ha, D.; Kooser, K.; Huels, M.; Rachlew, E.; Naummiste, E.; Joost, U.; Kukk, E. *Journal of Electron Spectroscopy and Related Phenomena* **2011**, *184*, Advances in Vacuum Ultraviolet and X-ray Physics, 119–124.

(235) Sakai, S.; Takane, S. *The Journal of Physical Chemistry A* **1999**, *103*, 2878–2882.

(236) Stolte, W. C.; Öhrwall, G. *The Journal of Chemical Physics* **2010**, *133*, 014306.

(237) Broughton, H. B.; Watson, I. A. *Journal of Molecular Graphics and Modelling* **2004**, *23*, 51–58.

(238) Jampilek, J. *Molecules* **2019**, *24*, 3839.

(239) Lamberth, C. *Pest Management Science* **2013**, *69*, 1106–1114.

(240) Sanemitsu, Y.; Kawamura, S. *Journal of Pesticide Science* **2008**, *33*, 175–177.

(241) Ahmed, S. K.; Ali, W. B.; Khadom, A. A. *International Journal of Industrial Chemistry* **2019**, *10*, 159–173.

(242) Singh, A.; Ansari, K. R.; Quraishi, M. A.; Kaya, S.; Banerjee, P. *New Journal of Chemistry* **2019**, *43*, 6303–6313.

(243) Aradhya, S. V.; Venkataraman, L. *Nature Nanotechnology* **2013**, *8*, 399.

(244) Ismael, A. K.; Lambert, C. J. *Journal of Materials Chemistry C* **2019**, *7*, 6578–6581.

(245) Fan, R.-H.; Hou, X.-L. *The Journal of Organic Chemistry* **2003**, *68*, PMID: 12558391, 726–730.

(246) Arruda, B. C.; Sension, R. J. *Physical Chemistry Chemical Physics* **2014**, *16*, 4439–4455.

(247) Havinga, E.; Schlatmann, J. *Tetrahedron* **1961**, *16*, 146–152.

(248) Izak-Nau, E.; Campagna, D.; Baumann, C.; Göstl, R. *Polymer Chemistry* **2020**, *11*, 2274–2299.

(249) Robertson, E. G. *Journal of Molecular Spectroscopy* **2005**, *231*, 50–56.

(250) Geng, T.; Ehrmaier, J.; Schalk, O.; Richings, G. W.; Hansson, T.; Worth, G.; Thomas, R. D. *The Journal of Physical Chemistry A* **2020**, *124*, 3984.

(251) Cao, J.; Xie, Z.-Z.; Yu, X. *Chemical Physics* **2016**, *474*, 25–35.

(252) Tanaka, H.; Matsushita, T.; Nishimoto, K. *Journal of the American Chemical Society* **1983**, *105*, 1753–1760.

(253) Dixit, G.; Slowik, J. M.; Santra, R. *Physical Review A* **2014**, *89*, 043409.

(254) Schülke, W., *Electron Dynamics by Inelastic X-Ray Scattering*, First; Oxford Science Publications: 2007.

(255) Waller, I.; Hartree, D. R. *Proceedings of the Royal Society of London. Series A, Containing Papers of a Mathematical and Physical Character* **1929**, *124*, 119.

(256) Bartell, L.; Gavin, R. *The Journal of Chemical Physics* **1965**, *43*, 856–861.

(257) Bonham, R. A.; Fink, M., *High Energy Electron Scattering*, ACS Monograph 169; ISBN 0-442-30891-4; Van Nostrand Reinhold Company: 1974.

(258) Debnarova, A.; Techert, S. *The Journal of Chemical Physics* **2006**, *125*, 224101.

(259) Northey, T.; Zotev, N.; Kirrander, A. *Journal of Chemical Theory and Computation* **2014**, *10*, 4911.

(260) Zotev, N.; Moreno Carrascosa, A.; Simmermacher, M.; Kirrander, A. *Journal of Chemical Theory and Computation* **2020**, *16*, PMID: 32142278, 2594–2605.

(261) Parrish, R. M.; Martínez, T. J. *Journal of Chemical Theory and Computation* **2019**, *0*, PMID: 30702882, null.

(262) Krause, P.; Klamroth, T.; Saalfrank, P. *The Journal of Chemical Physics* **2005**, *123*, 074105.

(263) Sonk, J. A.; Caricato, M.; Schlegel, H. B. *The Journal of Physical Chemistry A* **2011**, *115*, 4678–4690.

(264) Lopata, K.; Govind, N. *Journal of Chemical Theory and Computation* **2011**, *7*, 1344–1355.

(265) Runge, E.; Gross, E. K. *Physical Review Letters* **1984**, *52*, 997.

(266) Theilhaber, J. *Physical Review B* **1992**, *46*, 12990.

(267) Sun, J.; Song, J.; Zhao, Y.; Liang, W.-Z. *The Journal of Chemical Physics* **2007**, *127*, 234107.

(268) Ruiz, E.; Alvarez, S.; Cano, J.; Polo, V. *The Journal of Chemical Physics* **2005**, *123*, 164110.

(269) Perdew, J. P.; Zunger, A. *Physical Review B* **1981**, *23*, 5048.

(270) Cederbaum, L. S.; Zobeley, J. *Chemical Physics Letters* **1999**, *307*, 205–210.

(271) Kuleff, A. I.; Kryzhevoi, N. V.; Pernpointner, M.; Cederbaum, L. S. *Physical Review Letters* **2016**, *117*, 093002.

(272) Sissay, A.; Abanador, P.; Mauger, F.; Gaarde, M.; Schafer, K. J.; Lopata, K. *The Journal of Chemical Physics* **2016**, *145*, 094105.

(273) Sándor, P.; Sissay, A.; Mauger, F.; Abanador, P. M.; Gorman, T. T.; Scarborough, T. D.; Gaarde, M. B.; Lopata, K.; Schafer, K. J.; Jones, R. R. *Physical Review A* **2018**, *98*, 043425.

(274) Lopata, K.; Govind, N. *Journal of Chemical Theory and Computation* **2013**, *9*, 4939–4946.

(275) Lopata, K.; Van Kuiken, B. E.; Khalil, M.; Govind, N. *Journal of Chemical Theory and Computation* **2012**, *8*, 3284–3292.

(276) Bruner, A.; LaMaster, D.; Lopata, K. *Journal of Chemical Theory and Computation* **2016**, *12*, 3741–3750.

(277) Kadek, M.; Konecny, L.; Gao, B.; Repisky, M.; Ruud, K. *Physical Chemistry Chemical Physics* **2015**, *17*, 22566–22570.

(278) Nguyen, T. S.; Koh, J. H.; Lefelhocz, S.; Parkhill, J. *The Journal of Physical Chemistry Letters* **2016**, *7*, 1590–1595.

(279) Chen, M.; Lopata, K. *Journal of Chemical Theory and Computation* **2020**, 1.

(280) Szabo, A.; Ostlund, N. S., *Modern Quantum Chemistry: Introduction to Advanced Electronic Structure Theory*, Second; ISBN 0486691861; Dover Publishing Inc.: 1996.

(281) Wang, J.; Smith, V. H. *International Journal of Quantum Chemistry* **1994**, *52*, 1145–1151.

(282) Stolte, W. C.; Lu, Y.; Samson, J. A.; Hemmers, O.; Hansen, D. L.; Whitfield, S. B.; Wang, H.; Glans, P.; Lindle, D. W. *Journal of Physics B: Atomic, Molecular and Optical Physics* **1997**, *30*, 4489.

(283) Apra, E.; Bylaska, E. J.; De Jong, W. A.; Govind, N.; Kowalski, K.; Straatsma, T. P.; Valiev, M.; van Dam, H. J.; Alexeev, Y.; Anchell, J., et al. *The Journal of Chemical Physics* **2020**, *152*, 184102.

(284) Kuleff, A. I.; Lünnemann, S.; Cederbaum, L. S. *Chemical Physics* **2013**, *414*, 100–105.

(285) Calegari, F.; Ayuso, D.; Trabattoni, A.; Belshaw, L.; De Camillis, S.; Anumula, S.; Frassetto, F.; Poletto, L.; Palacios, A.; Decleva, P., et al. *Science* **2014**, *346*, 336–339.

(286) Breidbach, J.; Cederbaum, L. *Physical Review Letters* **2005**, *94*, 033901.

(287) Perfetto, E.; Trabattoni, A.; Calegari, F.; Nisoli, M.; Marini, A.; Stefanucci, G. *The Journal of Physical Chemistry Letters* **2020**, *11*, 891–899.

(288) Belshaw, L.; Calegari, F.; Duffy, M. J.; Trabattoni, A.; Poletto, L.; Nisoli, M.; Greenwood, J. B. *The Journal of Physical Chemistry Letters* **2012**, *3*, 3751–3754.

(289) Stankus, B.; Yong, H.; Ruddock, J.; Ma, L.; Carrascosa, A. M.; Goff, N.; Boutet, S.; Xu, X.; Zotev, N.; Kirrander, A.; Minitti, M.; Weber, P. M. *Journal of Physics B: Atomic, Molecular and Optical Physics* **2020**, 1.

(290) Carrascosa, A. M.; Northey, T.; Kirrander, A. *Physical Chemistry Chemical Physics* **2017**, *19*, 7853–7863.

(291) Northey, T.; Carrascosa, A. M.; Schäfer, S.; Kirrander, A. *The Journal of Chemical Physics* **2016**, *145*, 154304.

Vita

Mengqi Yang received her Bachelor degree in chemistry from Shanxi University in China in 2017. Following her graduation, she went to the United States and pursued a Ph.D. in theoretical studies of electron dynamics under the guidance of Dr.Kenneth Lopata at Louisiana State University. Her research focuses on simulations of electron dynamics and ultrafast spectroscopies including X-ray transient absorption and time-resolved X-ray scattering. She is anticipated to receive her Doctorate in August 2023 and continue her career in the study of electron motions.